Università degli Studi di Torino

Facoltà di Scienze Matematiche, Fisiche e Naturali
Corso di Laurea Specialistica in Fisica delle Interazioni Fondamentali

Observables in VV-fusion at the CMS Experiment

Relatore

Prof.sa Alessandra Romero

Co-Relatore

Dott.sa Chiara Mariotti

Candidato

Riccardo Bellan

Anno Accademico 2003/2004

Contents

Introduction

The Standard Model (SM) of Particle Physics provides a description of the basic components of matter and their interactions. The present belief is that all known matter can be described through twelve fundamental particles, the *fermions*, that can be divided into two main groups according to their different behaviour: *leptons* and *quarks*. The fermions interact through three types of interactions: electromagnetic, weak and strong interactions, which are mediated by another type of particle: the *vector bosons*. A fourth force is needed to describe the Universe, the Gravitation. Even if this is the interaction closest to everyday experience, its effect is completely negligible at the typical scales of mass and distance relevant for particle physics.

The Standard Model (Chapter 1) describes the three fundamental interactions with two gauge theories: the theory of the electroweak interaction, or Electroweak Standard Model, that unifies the electromagnetic and the weak interactions, and the theory of strong interactions or Quantum Chromodynamics (QCD). The SM for weak and electromagnetic interactions is constructed on a gauge theory with four gauge fields corresponding to massless bosons. Since only the photon is massless, whereas W and Z are massive, something has to happen in order to have electroweak unification. The masses of the gauge fields (as well as the fermions, in SM) are generated by spontaneous symmetry breaking. A renormalizable theory which perfectly reproduces the low-energy phenomenology is then obtained. Electroweak symmetry breaking in the Standard Model is described by the Higgs mechanism. At present this is the weak spot of the theory.

It maybe possible that we are in a scenario similar to the ones before the electroweak unification: physicists used a phenomenological theory (Fermi the-

ory) able to explain low energy phenomena, but non renormalizable and with non physical behaviour at high energies. The upgrade of the Fermi theory into a gauge theory, with the consequent introduction of the gauge bosons, provides a renormalizable model for the electroweak interactions. Similarly, if the Higgs boson does not exist, some processes could violate unitarity and then renormalizability could be lost. However, even the discovery of the Higgs boson could imply the necessity of new physics, depending on its mass. In fact only a limited range of masses around 160 GeV are compatible with the stability of the Standard Model up to the Planck mass scale. A very different mass would imply a breakdown of the Standard Model and give an indication of the scale at which new physics would become evident. Therefore it is important to study the processes that are sensitive both to Higgs production and to the no-Higgs scenario.

The aim of this work is to study the possibility to experimentally observe the *fusion of longitudinally polarized vector bosons* produced in $p-p$ collisions. The VV-fusion can probe the electroweak symmetry breaking without assuming the Higgs mechanism. The following processes:

$$pp \to V_L V_L + X \to Z_L Z_L + X \to \mu^+\mu^- jj + X$$

$$pp \to Z_L W_L + X \to Z_L W_L + X \to \mu^+\mu^- jj + X$$

have been studied in the framework of the CMS experiment at LHC. The results are summarized in Chapter 4. The CMS apparatus is described in Chapter 2. In Chapter 4 another goal of this work will be discussed: understand if $V_L V_L \to Z_L Z_L$ and $Z_L W_L \to Z_L W_L$ can be experimentally discriminated.

Since no real data are yet available, a simulation with Monte Carlo generator has been performed. The simulation and the processing through both the fast and the full detector simulation are treated in Chapter 3.

Chapter 1

The Standard Model

Introduction

All known particle physics phenomena are extremely well described within the Standard Model (SM) of elementary particles and their fundamental interactions. The SM provides a very elegant theoretical framework and it has successfully passed very precise tests which at present are at the 0.1% level [1, 2, 3, 4, 5].

We understand by elementary particles the point-like constituents of matter with no known substructure up to the present limits of 10^{-19} m. These are of two types, the basic building blocks of matter themselves known as matter particles and the intermediate interaction particles. The first ones are fermions of spin $s = 1/2$ and are classified into leptons and quarks. The known leptons are: the electron, e^-, the muon, μ^-, and the tau τ^-, with electric charge $Q = -1$ (all charges are given in units of the elementary charge e); and the corresponding neutrinos ν_e, ν_μ and ν_τ with $Q = 0$. The known quarks are of six different flavours: u, d, s, c, b, and t and have fractional charge $Q = \frac{2}{3}, -\frac{1}{3}, -\frac{1}{3}, \frac{2}{3}, -\frac{1}{3}$ and $\frac{2}{3}$, respectively. Both leptons and quarks have their corresponding antiparticles (particles with identical mass and spin, but with opposite additive quantum numbers with respect to the vacuum).

The quarks have an additional quantum number, the colour, which can be of three types, generically denoted as q_i with $i = 1, 2, 3$. We know that colour is not seen in Nature and therefore the elementary quarks must be confined into the experimentally observed matter particles, the hadrons. These colourless

Table 1.1: *Fermion features.*

Fermions	**1^{st} fam.**	**2^{nd} fam.**	**3^{rd} fam.**	**Charge**	**Interactions**
Quarks	$\begin{pmatrix} u \\ d \end{pmatrix}$	$\begin{pmatrix} c \\ s \end{pmatrix}$	$\begin{pmatrix} t \\ b \end{pmatrix}$	$+\frac{2}{3}$ $-\frac{1}{3}$	All
Leptons	$\begin{pmatrix} \nu_e \\ e \end{pmatrix}$	$\begin{pmatrix} \nu_\mu \\ \mu \end{pmatrix}$	$\begin{pmatrix} \nu_\tau \\ \tau \end{pmatrix}$	0 -1	Weak, E.M.

Table 1.2: *Gauge bosons features.*

	Electromagnetic	**Weak**	**Strong**
Quantum	Photon (γ)	$W^{\pm}$ and Z	gluons
Number of quantum	1	3	8
Mass (GeV/c^2)	0	80-90	0
Coupling constant	$\alpha(\mu = m_e) \simeq \frac{1}{137}$	$G_F = 1.167 \times 10^{-5} GeV^{-2}$	$\alpha_s(m_Z) \simeq 0.1$
Range (cm)	∞	10^{-16}	10^{-13}

composite particles are classified into baryons and mesons. The baryons are fermions made of three quarks, qqq, as for instance the proton, $p \sim uud$, and the neutron, $n \sim udd$. The mesons are bosons made of one quark and one antiquark as for instance the pions, $\pi^+ \sim u\overline{d}$ and $\pi^- \sim d\ \overline{u}$. A classification of fermions is given in Table 1.1.

The second kind of elementary particles are the intermediate interaction particles. Leaving aside the gravitational interactions, all the relevant interactions in particle physics are known to be mediated by the exchange of an elementary particle that is a boson with spin $s = 1$. The photon, γ, is the exchanged particle in the electromagnetic interactions, the eight gluons g_α, $\alpha = 1, .., 8$, mediate the strong interactions among quarks and the three weak bosons, $W^{\pm}$ and Z^0, are the corresponding intermediate bosons of the weak interactions. The main features of electromagnetic, weak and strong forces are summarized in Table 1.2.

1.1 The Standard Model

The Standard Model is a quantum field theory that is based on the gauge symmetry $SU(3)_{colour} \otimes SU(2)_L \otimes U(1)_Y$. This gauge group includes the symmetry group of the strong interactions, $SU(3)_{colour}$, and the symmetry group of the electroweak interactions, $SU(2)_L \otimes U(1)_Y$. The symmetry group of the electromagnetic interactions, $U(1)_{em}$, appears in the SM as a subgroup of $SU(2)_L \otimes U(1)_Y$ and it is in this sense that the weak and electromagnetic interactions are said to be unified.

The forces in the standard model are mediated by gauge bosons associated with the symmetries of the group $SU(3)_{colour} \otimes SU(2)_L \otimes U(1)_Y$.

The $SU(3)_{colour}$ factor describes the gluonic force of the strong interactions. Because the $SU(3)_{colour}$ gauge invariance is not broken, the eight associated gluons remain massless. The strong interactions do not have an infinite range, in spite of the gluon being massless, because of confinement. The theory of quarks interacting by exchange of gluons is called Quantum Chromodynamics (or QCD), to stress the parallel with Quantum Electrodynamics (or QED), which also has an unbroken gauge invariance and an associated massless gauge boson: the photon.

The $SU(2)_L \otimes U(1)_Y$ [1] factors describe the unified electroweak interactions. The $SU(2)_L$ group describes the left-handed isospin, an isospin charge carried by left-chirality fermions (chirality is equivalent to helicity in the ultra-relativistic limit). The subscript Y refers to "weak hypercharge", related to the electric charge and left isospin, by the relation:

$$Q = t_L^3 + \frac{Y}{2}\,. \tag{1.1}$$

Unlike the $SU(3)_{colour}$ factor, the $SU(2)_L \otimes U(1)_Y$ invariance is broken down to the $U(1)_{em}$ subgroup, the unbroken gauge invariance of electromagnetism. As a result, three of the four gauge bosons, $W^{\pm}$ and Z, of $SU(2)_L \otimes U(1)_Y$ are massive while the fourth, the photon (γ), remains massless.

Experimentally this is not a subtle effect. The W and the Z masses [6]:

[1] As show in the following, $SU(2)_L \otimes U(1)_Y$ gauge bosons are W^A (A=1,2,3) and B, which are massless. Physical vector bosons (γ, $W^{\pm}$, Z), which are linear combinations of W^A and B, are generated by electroweak symmetry breaking.

$$m_W = 80.423 \pm 0.039 \text{ GeV} \qquad m_Z = 91.1876 \pm 0.0021 \text{ GeV}$$

are responsible for the subnuclear range of the weak force $r_{weak} \sim \hbar/m_W c^2 \simeq 2.5 \cdot 10^{-16}$ cm. In contrast, Maxwell's laws are verified by measurement to a scale greater than $L_\gamma > 10^{16}$ cm. Therefore the symmetry-breaking mechanism produces a mass hierarchy of at least 26 orders of magnitude $m_W/m_\gamma > 10^{26}$.

The fact that the weak gauge bosons are massive particles, m_W, $m_Z \neq 0$, indicates that $SU(2)_L \otimes U(1)_Y$ is *not* a vacuum symmetry. In contrast, the photon being massless reflects the fact that $U(1)_{em}$ is a good symmetry of the vacuum. Therefore, the *Spontaneous Symmetry Breaking* pattern in the SM must be:

$$SU(3)_{colour} \otimes SU(2)_L \otimes U(1)_Y \rightarrow SU(3)_{colour} \otimes U(1)_{em}\,.$$

The dynamics of the symmetry-breaking mechanism is unknown. There are good reasons to believe that the general framework is the spontaneous symmetry breaking. The term "spontaneous" here means that the symmetry is not broken explicitly by the interactions but rather by the asymmetry of the state of lowest energy, referred to as the vacuum in quantum field theory. In the absence of an associated gauge symmetry, each spontaneously broken direction in the global (*i.e.* space-time independent) symmetry space gives rise to a massless, spin-zero particle or Goldstone boson. If the broken direction in symmetry space also correspond to a gauge symmetry (*i.e.* a space-time dependent symmetry) then the associated Goldstone boson and the massless gauge bosons combine to form a massive gauge boson: this is the Higgs mechanism. The Higgs Mechanism provides the proper masses to the W and Z gauge bosons and to the fermions, and leaves as a consequence the prediction of a new particle: the Higgs boson. This must be scalar and electrically neutral. This particle has not been seen in the experiments so far [5].

The Higgs mechanism preserves the number of states. A massless gauge boson occurs in two, transverse[2] polarization states, given in four-component notation by

[2]The terms transverse and longitudinal refer to the polarization of three-vectors: ε_T is transverse to the momentum $\mathbf{p}$ while ε_L is parallel to it.

$$\varepsilon_T^\mu = \frac{1}{\sqrt{2}}(0, 1, \pm i, 0)\,, \tag{1.2}$$

where the z direction is chosen as the direction of motion. Because a massive gauge boson can be brought to rest by a Lorentz transformation, and since there is no preferred direction in the rest frame, spatial isotropy requires three spin states. In the frame in which the massive gauge boson moves in the z direction, the two transverse spins states are given by Eq. (1.2), while the third spin state is longitudinally polarized

$$\varepsilon_L^\mu = \frac{1}{M}(E, 0, 0, p)\,. \tag{1.3}$$

As specified by the equivalence theorem (see later), at energies large compared to the gauge boson mass the longitudinal mode can be identified with the underlying Goldstone boson from the symmetry-breaking sector. In this sense we can say that three particles from the otherwise unknown symmetry-breaking sector have already been discovered: the longitudinal gauge modes $W_L^\pm$ and Z_L (here L denotes longitudinal). Therefore by studying the interactions of longitudinally polarized *W's* and *Z's* in the laboratory we can probe the dynamics of the unknown symmetry-breaking mechanism.

1.1.1 Before the Standard Electroweak Theory

The modern electroweak theory provides a well defined and consistent theoretical framework including weak interactions and quantum electrodynamics in a unified picture.

Weak interactions take their name from their intensity at low energy. An approximate model that can explain the behaviour at low energy of weak force is the Fermi effective four-fermion approximation. Thus the intensity of weak interaction at low energy is characterized by the Fermi coupling constant

$$G_F = 1.6639 \cdot 10^{-5} GeV^{-2} \tag{1.4}$$

and depends with quadratic law on the energy scale of process:

$$G_F E^2 \simeq 10^{-5} \frac{E^2}{m_p^2}\,, \tag{1.5}$$

where m_p is the proton mass. Observing Eq. (1.5), it is clear that the model has a bad behaviour at high energy (the unitarity is lost). This behaviour is corrected in the EW theory by the vector boson propagator, thus in such theory the unitarity is guaranteed also at high energy.

1.1.2 Electroweak Unification

The EW phenomenology is described by a gauge theory, based on $SU(2)_L \otimes U(1)_Y$ symmetry. As in the SM the left- and the right- handed fermions have different transformation properties under this gauge group, the mass terms (which are of the type $\overline{\psi_L}\psi_R + h.c.$) violate gauge invariance. Also the vector boson masses break the $SU(2)_L \otimes U(1)_Y$ symmetry. So if we want to give masses to the particles, we have to invoke a mechanism that both explains the symmetry breaking and provides masses to fermion and weak bosons and *not* to the electromagnetic field. In the SM the mass sector is described by Higgs mechanism [7, 8].

We can write the Standard Model Lagrangian as a sum of two parts:

$$\mathcal{L} = \mathcal{L}_{symm} + \mathcal{L}_{Higgs}\,, \tag{1.6}$$

the symmetric one is[3]

$$\mathcal{L}_{symm} = -\frac{1}{4}\sum_{A=1}^{3} F^A_{\mu\nu} F^{A\mu\nu} - \frac{1}{4} B_{\mu\nu} B^{\mu\nu} + \overline{\psi_L} i\gamma^\mu D_\mu \psi_L + \overline{\psi_R} i\gamma^\mu D_\mu \psi_R\,, \tag{1.7}$$

where

- $B_{\mu\nu} = \partial_\mu B_\nu - \partial_\nu B_\mu$.

  B_μ is the gauge field associated with the $U(1)_Y$ generator.

- $F^A_{\mu\nu} = \partial_\mu W^A_\nu - \partial_\nu W^A_\mu - g\varepsilon_{ABC} W^B_\mu W^C_\nu$.

[3] For simplicity only one generic family is discussed here, it is understood that complete SM Lagrangian is a sum over all families.

Table 1.3: *Lepton quantum numbers.*

Lepton	t	t_L^3	Q	Y
ν_L	$\frac{1}{2}$	$\frac{1}{2}$	0	-1
e_L	$\frac{1}{2}$	$-\frac{1}{2}$	-1	-1
e_R	0	0	-1	-2

W_μ^A are the gauge fields associated with the $SU(2)_L$ generators.

- $D_\mu = \partial_\mu + ig\sum_{A=1}^{3} t_L^A W_\mu^A + ig'\frac{Y}{2}B_\mu$.

  Since ψ_R is an *isosinglet*, then no terms proportional to g are made from D_μ.

  t_L^A are the $SU(2)_L$ generators and g the corresponding coupling constant, g' is the $U(1)_Y$ one, which has Y as generator.

  t_L^A obey angular momentum commutation laws,

$$t_L^A = \varepsilon_{ABC}\left[t_L^B, t_L^C\right], \tag{1.8}$$

  while there is an important relation between Y, t_L^3 and Q (the $U(1)_{em}$ generator):

$$Q = t_L^3 + \frac{Y}{2}. \tag{1.9}$$

- ψ_L is an $SU(2)_L$ doublet: $\psi_L^{lepton} = \begin{pmatrix} \nu_l \\ l \end{pmatrix}$ or $\psi_L^{quark} = \begin{pmatrix} u-type \\ d'-type \end{pmatrix}$; while ψ_R is an $SU(2)_L$ singlet. Quantum numbers for all fermions are listed in Tables 1.3 and 1.4.

$\mathcal{L}_{symm}$ contains the physical vector boson fields $W_\mu^\pm$, Z_μ, and A_μ. We can identify them as:

$$W_\mu^\pm = \frac{W_\mu^1 \pm iW_\mu^2}{\sqrt{2}} \tag{1.10}$$

and

Table 1.4: *Quark quantum numbers.*

Quark	t	t_L^3	Q	Y
u_L	$\frac{1}{2}$	$\frac{1}{2}$	$\frac{2}{3}$	$\frac{1}{3}$
d_L	$\frac{1}{2}$	$-\frac{1}{2}$	$-\frac{1}{3}$	$\frac{1}{3}$
u_R	0	0	$\frac{2}{3}$	$\frac{4}{3}$
d_R	0	0	$-\frac{1}{3}$	$-\frac{2}{3}$

$$\begin{cases} A_\mu = B_\mu \cos\theta_w + W_\mu^3 \sin\theta_w \\ Z_\mu = -B_\mu \sin\theta_w + W_\mu^3 \cos\theta_w \end{cases} , \tag{1.11}$$

where θ_w is the *Weinberg angle*, that relates the electroweak coupling constants

$$g \sin\theta_w = g' \cos\theta_w = e\,. \tag{1.12}$$

The Eq. (1.7) can be written as:

$$\mathcal{L}_{symm} = \mathcal{L}_{fermion} + \mathcal{L}_{A\overline{\psi}\psi} + \mathcal{L}_{W\overline{\psi}\psi} + \mathcal{L}_{Z\overline{\psi}\psi} + \mathcal{L}_{gauge}, \tag{1.13}$$

where

- $\mathcal{L}_{fermion} = i\overline{\psi}\gamma^\mu\partial_\mu\psi \equiv i\overline{\psi_L}\gamma^\mu\partial_\mu\psi_L + i\overline{\psi_R}\gamma^\mu\partial_\mu\psi_R$;
- $\mathcal{L}_{A\overline{\psi}\psi} = -Qe\overline{\psi}\gamma^\mu\psi A_\mu \equiv -Qe\left\{\overline{\psi_L}\gamma^\mu\psi_L + \overline{\psi_R}\gamma^\mu\psi_R\right\}A_\mu$;
- $\mathcal{L}_{W\overline{\psi}\psi} = -g\overline{\psi}\gamma^\mu\frac{1-\gamma_5}{2}\left[\frac{t_L^+W_\mu^-}{\sqrt{2}} + \frac{t_L^-W_\mu^+}{\sqrt{2}}\right]\psi W_\mu$
  $\equiv -g\overline{\psi_L}\gamma^\mu\left[\frac{t_L^+W_\mu^-}{\sqrt{2}} + \frac{t_L^-W_\mu^+}{\sqrt{2}}\right]\psi_L W_\mu$;
- $\mathcal{L}_{Z\overline{\psi}\psi} = -\frac{g}{2\cos\theta_w}\overline{\psi}\gamma^\mu\left[(1-\gamma_5)\,t_L^3 - 2Q\sin^2\theta_w\right]\psi Z_\mu$
  $\equiv -\frac{g}{\cos\theta_w}\left[\overline{\psi_L}\gamma^\mu t_L^3\psi_L - \overline{\psi}\gamma^\mu\psi Q\sin^2\theta_w\right]Z_\mu$;
- $\mathcal{L}_{gauge} = -ig_{WWV}\left[\left(W_{\mu\nu}^\dagger W^\mu V^\nu - W_\mu^\dagger V_\nu W^{\mu\nu} + W_\mu^\dagger W_\nu V^{\mu\nu}\right)\right] +$
  $-i\frac{g^2}{4}\left[\varepsilon^{kij}\varepsilon^{klm}g^{\mu\alpha}g^{\nu\beta}\right]W_\mu^i W_\nu^j W_\alpha^l W_\beta^m$,
  where $W_{\mu\nu} = \partial_\mu W_\nu - \partial_\nu W_\mu$, $V_{\mu\nu} = \partial_\mu V_\nu - \partial_\nu V_\mu$,
  $g_{WW\gamma} = e$ and $g_{WWZ} = e\cot\theta_w$.

In which $\gamma_5 = i\gamma^0\gamma^1\gamma^2\gamma^3$ and $t^{\pm} = t^1 \pm it^2$.

Equation (1.13) tells us that vector bosons can interact with each other also without fermion fields and reflects charge-parity violation.

The Higgs term is:

$$\mathcal{L}_{Higgs} = (D_\mu\phi)^\dagger (D^\mu\phi) - V\left(\phi^\dagger\phi\right) - \frac{G_F}{\sqrt{2}}\left(\overline{\psi_L}\mathcal{M}\phi\psi_R^d + \overline{\psi_R}\mathcal{M}\phi^C\psi_R^u + h.c.\right), \tag{1.14}$$

where in the Minimal Standard Model (MSM), ϕ is a doublet of Higgs fields:

$$\phi = \begin{pmatrix} \phi^+ \\ \phi^0 \end{pmatrix} = \frac{1}{\sqrt{2}}\begin{pmatrix} \phi^1 + i\phi^2 \\ \phi^3 + i\phi^4 \end{pmatrix} = \frac{1}{\sqrt{2}}\begin{pmatrix} w^1 + iw^2 \\ h + iw^3 \end{pmatrix} \tag{1.15}$$

and $\phi^C = i\sigma^2\phi^*$ is the charge conjugate of ϕ; it is introduced to explain *up-type* fermion masses.

D_μ has the same expression as the corresponding term in Eq. (1.7) and $\mathcal{M}$ is the fermion mass matrix. In the MSM we have only one Higgs doublet so the change of basis that makes $\mathcal{M}$ diagonal will at the same time diagonalize the fermion-Higgs couplings. Thus, no flavour changing neutral Higgs exchanges are present. Moreover from recent evidence [6] also neutrinos have masses, therefore $\mathcal{M}$ has non-null eigenvalues also in leptonic families.

The potential $V\left(\phi^\dagger\phi\right)$ is invariant under $SU(2)_L \otimes U(1)_Y$ and contains, at most, quartic terms in ϕ so that the theory is renormalizable:

$$V\left(\phi^\dagger\phi\right) = \frac{1}{2}\mu^2\phi^\dagger\phi + \lambda\left(\phi^\dagger\phi\right)^2, \tag{1.16}$$

in which $\mu^2 < 0$ and $\lambda > 0$. This combination of signs is crucial for the model (see Figure 1.1). If $\mu^2 > 0$ then the potential does not produce spontaneous symmetry breaking; if $\lambda < 0$ the vacuum should be unstable (no lower bounds).

Spontaneous symmetry breaking is induced if the minimum of *V,* which is the classical analogue of the quantum mechanical vacuum state, is obtained for non-vanishing ϕ values. It is simple to verify that Eq. (1.16), with requested condition on μ^2 and λ, has a minimum for $\phi_{min}^{class} = \sqrt{\frac{-\mu^2}{4\lambda}}$.

For the quantum vacuum state conventionally we place

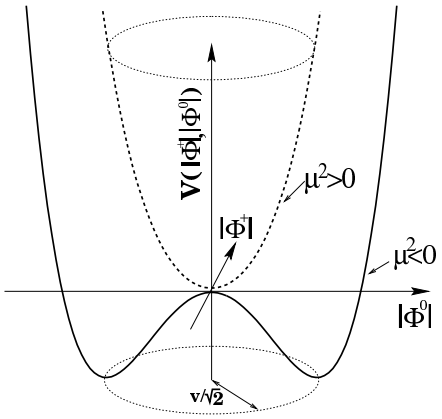

Figure 1.1: *Shape of the potential 1.16 for different signs of μ^2 and λ.*

$$\langle 0 \left| \phi(x) \right| 0 \rangle \equiv v = \frac{1}{\sqrt{2}} \begin{pmatrix} 0 \\ v \end{pmatrix} \tag{1.17}$$

with $v^2 = \frac{-\mu^2}{2\lambda}$. Since at tree level $m_H^2 \sim 2\lambda v^2$, spontaneous symmetry breaking with Higgs mechanism implies $m_H \neq 0$. From experimental measurement[4] $v = (G_F)^{-\frac{1}{2}} \simeq 246\,\mathrm{GeV}$.

It is possible to look at the Higgs mechanism as a perturbation of the vacuum introducing a field *H(x)*:

$$v_{per} = \frac{1}{\sqrt{2}} \begin{pmatrix} 0 \\ v + H(x) \end{pmatrix} . \tag{1.18}$$

In fact we can rewrite Eq. (1.15) in a more convenient (but approximate) form:

$$\phi \cong \frac{e^{i \frac{\overrightarrow{\xi(x)} \cdot \overrightarrow{t_L}}{v}}}{\sqrt{2}} \begin{pmatrix} 0 \\ v + H(x) \end{pmatrix} . \tag{1.19}$$

Where $\xi^{i=1,2,3}$ are the Goldstone bosons and $H(x)$ is the Higgs boson. The exponential term is absorbed by an $SU(2)_L \otimes U(1)_Y$ gauge transformation, $SU(2)_L$ symmetry breaks down and the Goldstone bosons disappear.

The boson fields acquire their masses by coupling to the vacuum value of

[4] The Fermi constant, $G_F = 1.16639(1) \times 10^{-5}\ \mathrm{GeV}^{-2}$, is determined from the muon lifetime [9, 10].

Table 1.5: *Higgs field couplings with fermion and vector bosons.*

	Mass	**Single Coupling**	**Double Coupling**
H	$v\sqrt{2\lambda}$	$\frac{m_H^2}{v}$	$\frac{m_H^2}{2v^2}$
W	$\frac{1}{2}gv$	$2\frac{m_W^2}{v}$	$\frac{m_W^2}{v^2}$
Z	$\frac{1}{2}\frac{gv}{\cos\theta}$	$2\frac{m_Z^2}{v}$	$\frac{m_Z^2}{v^2}$
$fermion$	$\frac{G_F}{2}vg_f$	$\frac{m_f}{v}$	

the Higgs field. Since the minimum for the Higgs field is invariant for *U(1)* transformations, the electromagnetic *U(1)* symmetry is therefore unbroken and the photon remains massless. This invariance is guaranteed by the condition:

$$Q\,|v\rangle = \left(t_L^3 + \frac{Y}{2}\right)|v\rangle = 0 \tag{1.20}$$

i.e. the request that the vacuum is electrically neutral.

Eq. (1.14) can be rewritten as

$$\mathcal{L}_{Higgs} = \mathcal{L}_H + \mathcal{L}_{HW} + \mathcal{L}_{HZ} + \mathcal{L}_{YC}\,, \tag{1.21}$$

where

- $\mathcal{L}_H = \frac{1}{2}\partial^\mu H \partial_\mu H - \lambda v^2 H^2 - 2\lambda v H^3 - \lambda H^4$;
- $\mathcal{L}_{HW} = \frac{1}{4}g^2 v^2 W^{\mu+} W_\mu^- + \frac{1}{2}g^2 v H W^{\mu+} W_\mu^- + \frac{1}{4}g^2 H^2 W^{\mu+} W_\mu^-$;
- $\mathcal{L}_{HZ} = \frac{1}{8}\frac{g^2v^2}{\cos^2\theta_w} Z^\mu Z_\mu + \frac{1}{4}\frac{g^2 v}{\cos^2\theta_w} H Z^\mu Z_\mu + \frac{1}{8}\frac{g^2}{\cos^2\theta_w} H^2 Z^\mu Z_\mu$;
- $\mathcal{L}_{YC} = -\frac{G_F}{2} v \left(g_d \overline{d} d + g_u \overline{u} u\right) - \frac{G_F}{2} H \left(g_d \overline{d} d + g_u \overline{u} u\right)$;

  where $d = (l, d' - type)$ and $u = (\nu, u - type)$ associated to the respective constant couplings.

From equations (1.21) it is easy to obtain the relations given in Tab. 1.5.

The Higgs mechanism allows the incorporation of weak boson masses while preserving the renormalizability of the theory. A theory based on a Lagrangian which does not respect the gauge symmetry is unrenormalizable and loses therefore all predictive power. Conversely, in a spontaneously broken gauge theory

the symmetry is in a sense still present; it is merely "hidden" by our choice of the ground state and the theory can be shown to be renormalizable. The Higgs mechanism gives rise to three massive gauge bosons and a massless one, corresponding to eleven degrees of freedom. Since the initial number of independent fields was twelve (four massless vector bosons with two polarization states each and four scalar fields), one additional scalar gauge boson should appear as a real particle. This is the Higgs boson. When the gauge symmetry is spontaneously broken three massless real fields, the Goldstone bosons, disappear and the W and Z bosons acquire their masses. The degree of freedom linked to the Goldstone bosons becomes the longitudinal degree of freedom of the vector bosons. This is the Higgs mechanism.

1.1.3 The QCD Lagrangian

In the present work no strong sector of Standard Model is treated. Only for completeness the Lagrangian of QCD is given

$$\mathcal{L}_{QCD} = \sum_q \overline{q_i}(i\gamma_\mu D^\mu_{ij} - \delta_{ij} m_q) q_j - \tfrac{1}{4} F^\alpha_{\mu\nu} F^{\mu\nu}_\alpha \ ;$$

$$D^\mu_{ij} = \delta_{ij}\partial^\mu - i g_s \left(\tfrac{\lambda^\alpha}{2}\right)_{ij} A^\mu_\alpha \ , \tag{1.22}$$

$$F^\alpha_{\mu\nu} = \partial_\mu A^\alpha_\nu - \partial_\nu A^\alpha_\mu + g_s f^{\alpha\beta\gamma} A_{\mu\beta} A_{\nu\gamma} \ ;$$

where *i=1, 2, 3* are the colours of quark fields q_i (the *"sum over q"* means sum over quark flavours); $\frac{\lambda^\alpha}{2}$ are the $SU(3)_{color}$ generators (they are usually given in terms of the so-called Gell-Mann matrices [11]) and A^α_μ (with $\alpha = 1, ..., 8$) are the corresponding gauge fields (*i.e.* the gluon fields).

1.1.4 Experimental Success of SM

The Standard Model has been successfully tested at the LEP collider, at the Tevatron and at HERA [5]. Precision tests were performed on the most important observables predicted by the SM (see Table 1.6). The main lesson of the precision tests can be summarized as follows. It has been checked that couplings of quarks and leptons to weak gauge bosons W and Z are indeed precisely those

Table 1.6: *Electroweak precision test results (Winter 2004).*

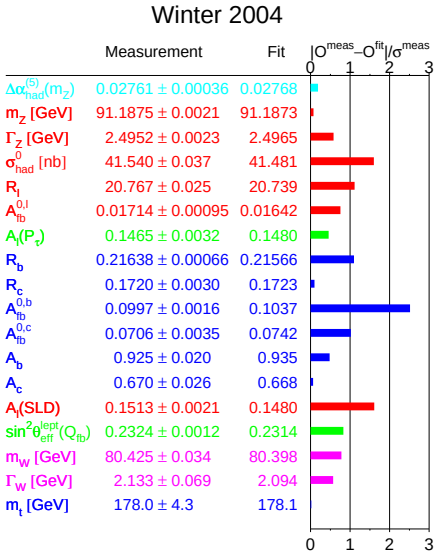

prescribed by the gauge symmetry. The accuracy of a few 0.1% for these tests implies that, not only the tree level, but also the quantum corrections have been verified. Even if not with comparable precision, triple gauge vertexes γW^+W^- and ZW^+W^- have been measured and found in agreement with the predicted non abelian structure of the theory. This means that the gauge symmetry is indeed unbroken in the vertices of the theory: the currents are indeed conserved. Yet there is obvious evidence that the symmetry is otherwise badly broken in the masses. In fact the $SU(2)_L \otimes U(1)_Y$ gauge symmetry forbids masses for all the particles that have been so far observed: quarks, leptons and gauge bosons. But of all these particles only the photon and the gluons are massless (protected by the $SU(3)_{color} \otimes U(1)_{em}$ unbroken colour and electric charge gauge symmetry), all other are massive. The Higgs particle, responsible for the EWSB and the particle masses, has not been found but its mass can well be heavier than the present direct lower limit $m_H > 114.4\,\text{GeV}$ (95% confidence level) obtained at the LEP2 [12].

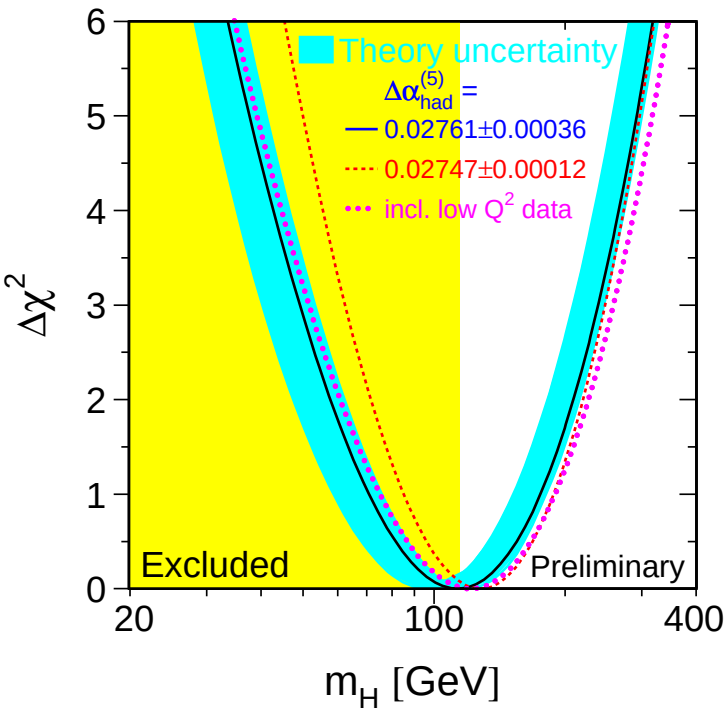

Figure 1.2: *The Blue band: experimental limit on Higgs mass (Winter 2004).*

1.2 Vector Bosons Fusion

1.2.1 V_LV_L Interactions as a Probe of EW Symmetry Breaking

We can rewrite Eq. (1.16) in the following way:

$$V = \lambda\left(\phi^2 - \frac{v^2}{2}\right)^2 \tag{1.23}$$

plus a constant term that can be reabsorbed by a potential translation. Substituting Eq. (1.15) inside Eq. (1.23) and dropping h in $h + v$[5] we obtain:

$$V = \frac{\lambda}{2}\left(\mathbf{w}^2 + h^2\right)^2 + \lambda v h\left(\mathbf{w}^2 + h^2\right) + \lambda v^2 h^2\,, \tag{1.24}$$

where $\mathbf{w}^2 = w_1^2 + w_2^2 + w_3^2$. The equation above illustrates Goldstone's theorem: before breakdown the potential (1.23) had a four-dimensional $O(4)$ symmetry in the space spanned by $\mathbf{w}$ and h, that was reduced to the $O(3)$ symmetry of the space spanned by triplet $\mathbf{w}$ in Eq. (1.24). The number of invariant generators is reduced from the six of $O(4)$ to the three of $O(3)$, each broken generator gives rise to a massless Goldstone boson. In equation (1.24) we can see that the *would-be* Higgs field h has a mass, while the $\mathbf{w}$ (Goldstone bosons) are massless.

The potential of (1.24) viewed in the Lagrangian of (1.14) gives us another information: before the Goldstone boson are adsorbed by vector bosons (during the gauge transformation) *they* are coupled with the Higgs field and not with the transverse vector bosons, which appear in the symmetric term of the Lagrangian. Therefore intimate relations are present among the vector boson masses, the Goldstone bosons and the longitudinal polarization.

A proof of those relations existence is the so called *equivalence theorem.*

Equivalence theorem. If $\mathcal{M}(W_L^+, W_L^-, Z_L, H)$ is an amplitude for the scattering of longitudinal intermediate bosons and the physical Higgs particle and if

[5] There is a slight difference between h and H: the first is scalar field described by Eq. (1.26), and then *could be* the Higgs boson, whereas H is a scalar field that is described by Eq. (1.14) that is equation (1.26) where ordinary derivative is substituted by covariant derivative, and then *is* the Higgs boson.

$\mathcal{M}(w^+, w^-, z, h)$ is the analogous amplitude for the scalar field theory described by (in the 't Hooft- Feynman gauge)

$$\mathcal{L}_{SB} = (\partial^\mu \phi)^\dagger (\partial_\mu \phi) - \lambda \left(\phi^2 - \frac{v^2}{2}\right)^2 \tag{1.25}$$

after symmetry breaking:

$$\mathcal{L}_{SB} = \frac{1}{2}\partial^\mu \mathbf{w} \partial_\mu \mathbf{w} + \frac{1}{2}\partial^\mu h \partial_\mu h - \frac{\lambda}{2}\left(\mathbf{w}^2 + h^2\right)^2 - \lambda v h \left(\mathbf{w}^2 + h^2\right) - \lambda v^2 h^2 \,, \tag{1.26}$$

then for $s \gg m_W^2,\ m_Z^2$

$$\mathcal{M}(W_L^+, W_L^-, Z_L, H) \sim \mathcal{M}(w^+, w^-, z, h) + O\left(\frac{m_W}{\sqrt{s}}\right) . \tag{1.27}$$

Therefore at high energy in the VV-fusion centre of mass, only the longitudinally polarized V's interact with the symmetry breaking sector. Since the longitudinal degrees of freedom of the vector bosons are the signature of symmetry breaking, longitudinally polarized vector boson fusion is the best candidate to study EWSB[6], whereas transversally polarized V's will be a background to our observables.

1.2.2 Longitudinal VB Production

At high energy, there are many competitive mechanisms able to produce W and Z bosons and W_L and Z_L in particular. Some of these are more sensitive than others to the longitudinal components of V's.

One mechanism to produce vector boson pairs at future colliders is through fermion anti-fermion annihilation. This is the case of $q\overline{q}$ annihilation in hadron colliders. This process yields vector boson pairs that are mostly transversely polarized and will usually be a background to the processes considered here.

A second mechanism for producing longitudinal vector boson pairs in hadron

[6] $\mathcal{L}_{SB}$ is more general than $\mathcal{L}_{Higgs}$ in the sense that $\mathcal{L}_{SB}$ is necessary to have Higgs mechanism, but the inverse it is not necessary true! In fact $\mathcal{L}_{SB}$ takes is mean only by supposing that has to explain $SU(2)_L \otimes U(1)_Y$ invariance broken down to the $U(1)_{em}$ subgroup. Therefore with longitudinal vector boson fusion we can probe EWSB also outside the Minimal Standard Model.

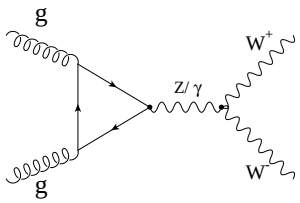

Figure 1.3: *Schematic diagram of gluon fusion*

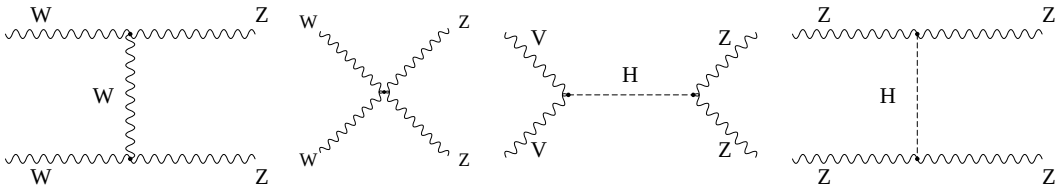

Figure 1.4: $VV \to ZZ$ *diagrams. The first and the last diagrams have also the* u-channel *diagrams.*

colliders is gluon fusion [13]. In this case the initial gluons turn into two vector bosons via an intermediate state that couples to both gluons and electroweak gauge bosons (see diagram 1.3). Examples are: the top quark and possibly new heavy quarks. In this case, only neutral $V_L V_L$ pairs can be produced, and thus this channel is particularly sensitive to new physics with a scalar resonance like a heavy Higgs boson.

Finally, there is the vector boson fusion process ($V_L V_L \to V_L V_L$), which is important in the case of strongly-interacting vector bosons. The major advantage for studying vector boson fusion processes is that they involve all possible channels mediated by scalar and vector resonances, as well as purely non-resonant ones.

In the present work two kinds of longitudinally polarized vector boson fusion are taken in account:

- $V_L V_L \to Z_L Z_L$;
- $W_L^{\pm} Z \to W_L^{\pm} Z$.

In Figure 1.4 and 1.5 the Feynman diagrams for these channels are shown.

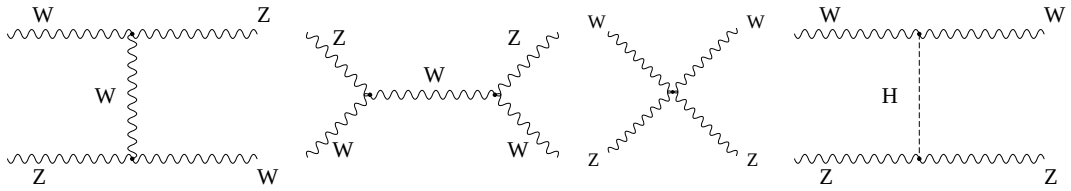

Figure 1.5: $W_L^{\pm}Z \to W_L^{\pm}Z$ *diagrams.*

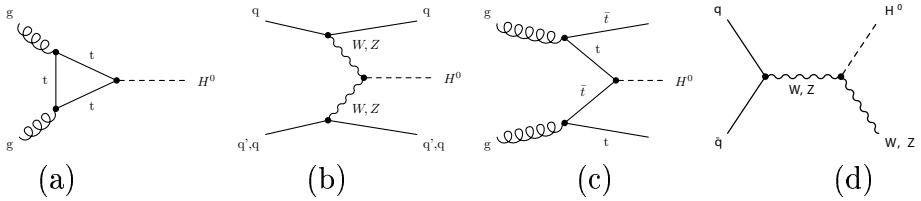

Figure 1.6: *Tree-level diagrams of Higgs production mechanism in* proton-proton *collisions: (a)* gluon-gluon *fusion, (b)* W *and* Z *fusion, (c)* $t\bar{t}$ *associated production, (d)* W *and* Z *associated production.*

1.2.3 Higgs Production and Search

Since not only V_LV_L fusion can produce the Higgs resonance, in this section we will briefly review the different production mechanisms and decay modes of the Higgs boson.

Main processes and cross sections for Higgs production at an hadron collider are shown in Figs. 1.6 and 1.7 respectively. Vector boson fusion is the second most important process for producing the Higgs boson. Gluon-gluon fusion has the largest cross section on the whole m_H spectrum and only at very high Higgs masses does the boson fusion production become comparable. However, even if the VV fusion process has on average a cross section about 5 to 10 times smaller, this channel is extremely interesting because of its clear experimental signature. In fact, the presence of two spectator jets provides a powerful tool to tag the signal events discriminating the backgrounds.

As far as the signature of the Higgs production is concerned, we need to consider the Higgs branching ratio. The Higgs couplings to fermions and gauge bosons are given in Table 1.5. They are proportional to the masses of the decay particles; therefore, the final state with the heaviest particles dominates the

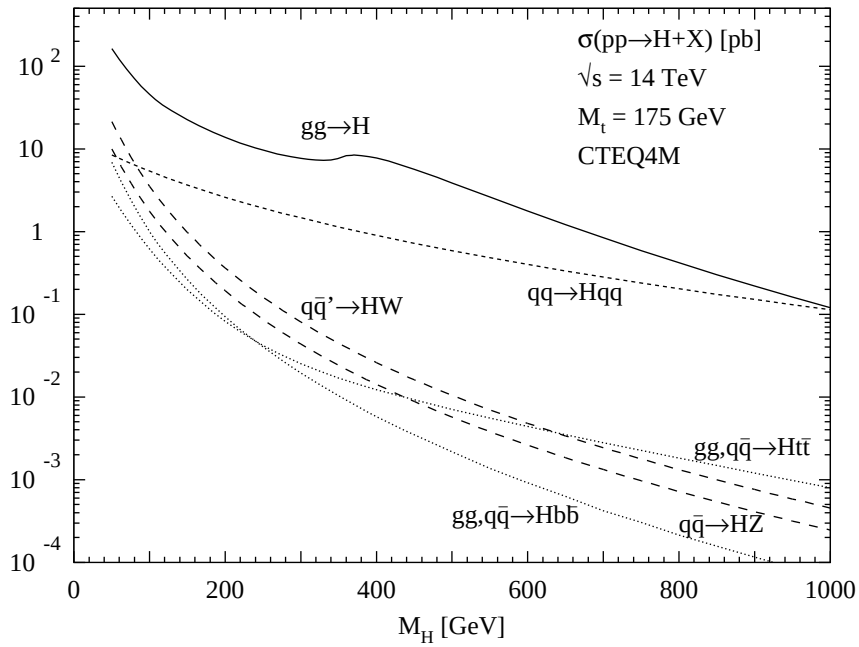

Figure 1.7: *Cross sections of different Higgs production mechanism as a function of the Higgs mass [14].*

Higgs decay when kinematically allowed. Figure 1.8 shows the branching ratio of the Higgs boson as a function of m_H. For low masses ($m_H < 130$ GeV) the $H \to b\bar{b}$ decay is the most important since the b-quark is the heaviest fermion kinematically available. However, this decay channel is difficult to observe because of the huge QCD background. In this mass region the most interesting channel is $H \to \gamma\gamma$ which, despite its low branching ratio ($\sim 10^{-3}$) has a very clean signature. Of course excellent photon energy and angular resolution are required. At high Higgs masses ($\geq 2m_V$) the WW and ZZ final states become available.

The total decay width is obtained by summing all possible decay channels. At low Higgs masses the width remains extremely narrow (a few MeV at $m_H \simeq$ 100 GeV) reaching $\sim$ 1 GeV at $m_H = 200$ GeV. At higher masses it becomes broad: $\Gamma > 100$ GeV above $m_H = 600$ GeV.

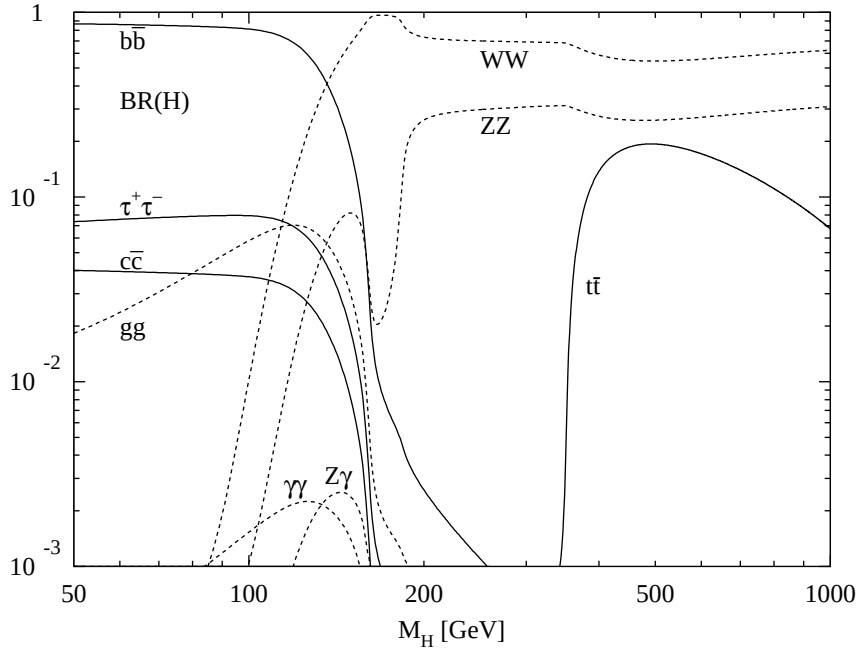

Figure 1.8: *Branching ratio of the Higgs boson as a function of the Higgs mass [14].*

1.2.4 Heavy Higgs

As already seen in the previous section at high invariant masses the Higgs production is mainly due to the gluon-gluon fusion and VV-fusion processes. In this mass region the Higgs boson mainly decays into a WW or ZZ pair and the decay widths are [15]:

$$\Gamma(H \to ZZ) = \frac{g^2}{128\pi}\frac{m_H^3}{m_W^2}\sqrt{1-x_Z}\left(1 - x_Z + \frac{3}{4}x_Z^2\right) \tag{1.28}$$

and

$$\Gamma(H \to W^+W^-) = \frac{g^2}{64\pi}\frac{m_H^3}{m_W^2}\sqrt{1-x_W}\left(1 - x_W + \frac{3}{4}x_W^2\right) \tag{1.29}$$

where

$$x_Z = \frac{4m_Z^2}{m_H^2} = \frac{x_W}{\cos^2\theta_w}\,, \tag{1.30}$$

$$x_W = \frac{4m_W^2}{m_H^2}\,. \tag{1.31}$$

For energetically allowed decays $x_V \leq 1$. As the Higgs mass grows, $x_V \to 0$ and the leading term grows proportional to m_H^3. Summing over the $W^\pm$ and Z channels the Higgs width can be written as

$$\Gamma(H \to VV) \simeq \frac{1}{2} m_H^3 \text{ (TeV)}\,. \tag{1.32}$$

Therefore, we have that $\Gamma \simeq m_H$ when $m_H \simeq 1.4$ TeV, so once the mass becomes larger than a TeV it becomes experimentally very problematic (and perhaps not very significant) to separate the Higgs resonance from the VV continuum.

The ratio between the Higgs decay widths into longitudinally or transversally polarized gauge bosons is:

$$\frac{\Gamma(H \to V_T V_T)}{\Gamma(H \to V_L V_L)} = \frac{\frac{1}{2}x_V^2}{\left(1 - \frac{1}{2}x_V\right)^2}\,. \tag{1.33}$$

The dominance of the longitudinal vector bosons arises from the fact that the longitudinal degrees of freedom are directly related to the Goldstone bosons which are an essential ingredient of the symmetry breaking (see Section 1.2.1).

The different Higgs signatures are related to all possible combinations of W and Z decays. Table 1.7 shows the product of the cross section and the branching ratio for different possible final states. All values are normalized to $H \to ZZ \to l^+l^-l^+l^-$ which is the "gold-plated" mode for the Higgs search. In Table 1.7 some possible final states are omitted since they are not observable, for instance in the $H \to ZZ \to \nu_i\overline{\nu_i}\nu_j\overline{\nu_j}$ channel the final state cannot be reconstructed because of the presence of four undetected neutrinos, while the purely hadronic channels $H \to ZZ \to q_i\overline{q_i}q_j\overline{q_j}$ and $H \to WW \to q_i\overline{q_j}q_k\overline{q_l}$ are not accessible because of the large QCD background.

The branching ratio is not the only parameter which needs to be evaluated in order to judge the feasibility of detecting the Higgs boson in each of the channels of Table 1.7. It is also interesting to understand what are the main sources of background and to verify if it is possible to reconstruct the signal with good accuracy and efficiency. Of course, the fully leptonic final state has

Table 1.7: *Cross sections multiplied by the* BR *for most of the Higgs decay channels normalized to the "gold-plated" channel. Here "l" indicates each type of lepton (*e, μ *and* τ*), not sum over them.*

Decay channel	$\sigma \times BR$
$H \to ZZ \to l^+l^-l^+l^-$	1
$H \to ZZ \to l^+l^-\nu_i\overline{\nu_i}$	6
$H \to WW \to l\nu l\nu$	10
$H \to ZZ \to l^+l^-q_i\overline{q_i}$	21
$H \to WW \to l\nu q_i\overline{q}_j$	64
$H \to ZZ \to \nu_i\overline{\nu_i}q_j\overline{q_j}$	123

a clear signature which allows a precise Higgs mass reconstruction, but it also has a very small BR. The most promising channels are $H \to WW \to l\nu q_i q_j$, which has a large branching ratio, and where the presence of a lepton permits to identify the leptonic W decay, and $H \to ZZ \to l^+l^-q_i\overline{q_i}$ which has a less larger BR than the previous channel, but has a very clean (and unambiguous) leptonic signature.

1.3 Constraints in Spontaneous Symmetry Breaking

1.3.1 Unitarity Constraint

We have seen that at high energies the scattering of longitudinally polarized vector bosons V_L can be approximated by the scattering of the would-be Goldstone bosons $w^\pm$ and z ($w^\pm = (w^1 \pm iw^2)/\sqrt{2}$ and $z = w^3$). Therefore ignoring gauge couplings and gauge boson masses we can parametrize the scattering amplitudes as [16, 17]:

$$\mathcal{M}(W_L^+W_L^- \to Z_LZ_L) = A(s,t,u)\,, \tag{1.34}$$

$$\mathcal{M}(Z_LZ_L \to W_L^+W_L^-) = A(s,t,u)\,, \tag{1.35}$$

$$\mathcal{M}(W_L^+W_L^- \to W_L^+W_L^-) = A(s,t,u) + A(t,s,u)\,, \tag{1.36}$$

$$\mathcal{M}(Z_LZ_L \to Z_LZ_L) = A(s,t,u) + A(t,s,u) + A(u,t,s)\,, \tag{1.37}$$

$$\mathcal{M}(W_L^\pm Z_L \to W_L^\pm Z_L) = A(t,s,u)\,, \tag{1.38}$$

$$\mathcal{M}(W_L^\pm W_L^\pm \to W_L^\pm W_L^\pm) = A(t,s,u) + A(u,t,s)\,, \tag{1.39}$$

where s, t and u are the usual Mandelstam variables and in the Standard Model

$$A(s,t,u) = \frac{-m_H^2}{v^2}\left(1 + \frac{m_H^2}{s - m_H^2 + im_H\Gamma_H\theta(s)}\right)\,, \tag{1.40}$$

where $\Gamma_H = 3m_H^3/32\pi v^2$ is given by the sum over all partial widths, and $\theta(s)$ is Heaviside step function.

Equation (1.37) (see diagrams in Fig. 1.4 [7]) can be taken as an example. Since it is analyzed for $s \gg m_H^2$ the width contribution can be neglected. Thus

$$\mathcal{M}(Z_LZ_L \to Z_LZ_L) = -\sqrt{2}G_F m_H^2\left(\frac{s}{s - m_H^2} + \frac{t}{t - m_H^2} + \frac{u}{u - m_H^2}\right)\,. \tag{1.41}$$

From the partial wave method we have the relation:

$$\mathcal{M}(s,t,u) = 16\pi\sum_{J=0}^{\infty}(2J+1)a_J(s)P_J(\cos\theta)\,, \tag{1.42}$$

where $P_J(\cos\theta)$ are the Legendre polynomials. It is possible exploit their properties of orthogonality to find the partial wave amplitude $a_J(s)$ for orbital angular momentum J:

$$a_J(s) = \frac{1}{32\pi}\int d(\cos\theta_{cm})P_J(\cos\theta_{cm})\mathcal{M}(s,\theta_{cm})\,. \tag{1.43}$$

The corresponding differential cross-section is given by:

[7] In the *s-channel* Higgs exchange V's are replaced by Z's. Moreover no quartic coupling exists for this process.

$$\frac{d\sigma_{el}}{d\Omega} = \frac{1}{64\pi^2 s} |\mathcal{M}|^2 . \tag{1.44}$$

Thus, the elastic cross-section in terms of partial waves is:

$$\sigma_{el} = \frac{16\pi}{s} \sum_{J=0}^{\infty} (2J+1) |a_J(s)|^2 . \tag{1.45}$$

On the other hand, the *optical theorem* relates the total cross-section with the forward elastic scattering amplitude:

$$\sigma_{tot}(1+2 \to \text{anythings}) = \frac{1}{s} \text{Im} \left(\mathcal{M}(s, \cos\theta = 1) \right) . \tag{1.46}$$

Since $\sigma_{el} \leq \sigma_{tot}$ we find the inequality $|a_J|^2 \leq |\text{Im}(a_J)|$, from the which it is possible extract the unitarity condition

$$|\text{Re}(a_J)| \leq \frac{1}{2} . \tag{1.47}$$

It is easy to calculate Eq. (1.43) for the amplitude given by Eq. (1.41) for *J=0* partial wave

$$a_0(Z_L Z_L \to Z_L Z_L) = \frac{-G_F m_H^2}{8\pi} \left[3 + \frac{m_H^2}{s - m_H^2} - \frac{2m_H^2}{s} \ln \left(1 + \frac{s}{m_H^2} \right) \right] , \tag{1.48}$$

therefore for $s \gg m_H^2$ it becomes

$$a_0(Z_L Z_L \to Z_L Z_L) \simeq \frac{-3G_F m_H^2}{8\pi} . \tag{1.49}$$

Combining Eq. (1.49) with the unitarity condition (1.47) it is easy to find that:

$$m_H^2 \leq \frac{4\pi}{3G_F} \simeq (600 \text{ GeV})^2 . \tag{1.50}$$

If m_H is substantially less than the critical value, the magnitude of the amplitude is well within the bound (1.47) everywhere except near the Higgs boson resonance pole, where anyhow finite width corrections are sufficient to rescue the unitarity. In contrast, if m_H attains or exceeds the critical value, the unitarity bound will be violated, at the tree level approximation, at all energies

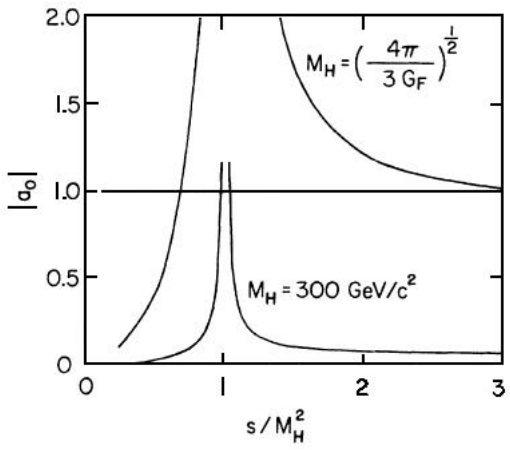

Figure 1.9: *Sketch of the energy dependence of the* J=0 *partial wave amplitude for elastic scattering of longitudinally polarized vector bosons for two choices of the Higgs boson mass. For* $m_H > (4\pi/3G_F)^{1/2}$ *the partial wave unitarity bound (1.47) is violated for* $s > m_H^2$ *[18, 19].*

above the Higgs-boson pole (see fig. 1.9) . Of course no properly calculated amplitude will ever violate unitarity, simply our theory (*i.e.* SMSB) becomes an effective low energy model of a underlying strongly interacting theory.

1.3.2 The Task of the Higgs Boson in the Standard Model

We have just discussed the importance of the Higgs boson in the Standard Model as a field which can give mass to fermions and vector bosons; but it accomplishes another important task. As an example the $WW \to WW$ process can be considered. Considering only the no Higgs exchange diagrams in Fig. 1.10 we find that this amplitude grows like E_{cm}^2:

$$\mathcal{M} \sim \frac{G_F s}{\sqrt{2}}(1 + \cos\theta_{cm}) \tag{1.51}$$

so rewriting Eq. (1.43) for *J=0* we can find

$$a_0 \sim \frac{G_F s}{16\pi\sqrt{2}}\,; \tag{1.52}$$

now using relation (1.47) we obtain a critical energy

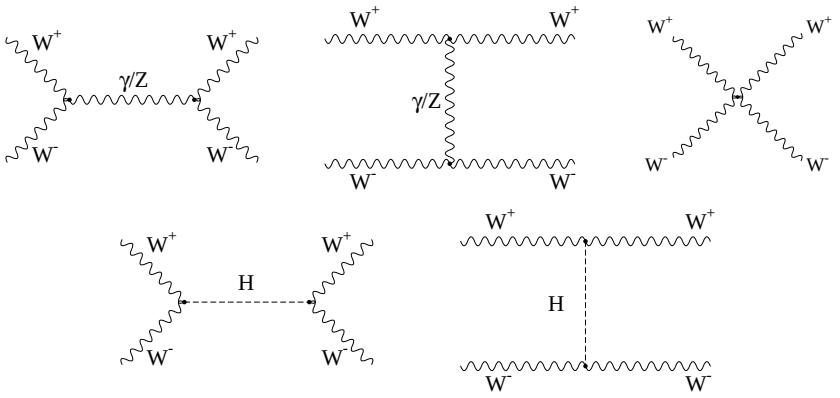

Figure 1.10: $W^+W^- \to W^+W^-$ *diagrams.*

$$s_c = \frac{8\pi\sqrt{2}}{G_F} \simeq (1.7 \text{ TeV})^2 . \tag{1.53}$$

This means that if the Higgs boson does not exist, for $\sqrt{s} \sim 1.7\,\text{TeV}$ new physics must appear (*i.e.* new resonance or strongly interacting behaviour of electroweak force). But if the Higgs boson exists (and it has a mass between the limits previously given), then also diagrams four and five of Fig. 1.10 are present which contribute to the total amplitude as

$$\mathcal{M} \sim -\frac{G_F s}{\sqrt{2}}(1 + \cos\theta_{cm}) . \tag{1.54}$$

Thus the bad behaviour of (1.51) is cancelled by the Higgs exchange diagrams. Considering all diagrams plus the terms that do not grow with energy, we find again the relations (1.34) to (1.39).

Therefore if no Higgs boson exists the SM becomes a low-energy effective theory of an unknown strong interaction. Since the predictivity of a low-energy effective theory is lost at energies beyond the critical threshold (1.53), many phenomenological models are used to obtain results that are, at least, internally consistent. All these models are based on the unavoidable requirement of the scattering amplitude unitarity. For example, the Padé unitarisation model [20] proposes that each scattering channel is dominated by a single resonance in the cross section. This assumption is somehow inferred by analogy between the

new strong interactions and low-energy pion scattering (QCD) which exhibits resonances in several channels. On the other hand, the K-matrix model [21] presents the saturation of the Goldstone boson scattering amplitudes without resonances. These are only two of the possible scenarios and many others have been studied. However, since the aim of the present study is to probe the symmetry breaking mechanism without any model assumption on new physics, no degrees of freedom beyond the Standard Model were considered.

1.3.3 Lower Limit on the SM Higgs

In this section and in the following, limits on Higgs mass are discussed. It is important understand that even if the Higgs boson is found, the SM, for internal consistency, predicts an energy scale at which new physics must appear. This new physics could be investigated by processes studied in this work.

A lower limit [22, 23] on the Higgs mass m_H can be derived from the requirement of vacuum stability. The limit is a function of the top quark mass m_t and of the energy scale Λ where the model breaks down and new physics appears. The possible instability of the Higgs potential $V(\phi^\dagger\phi)$ is generated by quantum loop corrections to the classical expression of $V(\phi^\dagger\phi)$. At large ϕ the derivative $V'(\phi^\dagger\phi)$ could become negative and the potential would become unbound from below. As demonstrated in [24, 25] the stability of the potential for $\phi \sim \Lambda \gg m_Z$ practically coincides with the requirement that the running coupling $\lambda(\mu)$ never becomes negative up to the break down scale Λ.

The one-loop renormalization group equation (RGE) for $\lambda(\mu)$ is:

$$\frac{d\lambda(\mu)}{d\ln\mu} = \frac{1}{8\pi^2}\left[12\lambda^2 + \frac{3}{8}g^4 + \frac{3}{16}\left(g^2+g'^2\right)^2 - 12\left(\frac{m_t}{v}\right)^4 - 3\lambda g^2 + \right. \\ \left. -\frac{3}{2}\lambda\left(g^2+g'^2\right) + 12\lambda\left(\frac{m_t}{v}\right)\right]. \tag{1.55}$$

This equation must be solved together with the one-loop RGEs for the gauge and Yukawa couplings, which, in the Standard Model, are given by[8]:

[8] For the convention adopted here, the system of coupled equations is solved with the initial condition $\lambda(m_H) = m_H^2/2v^2$.

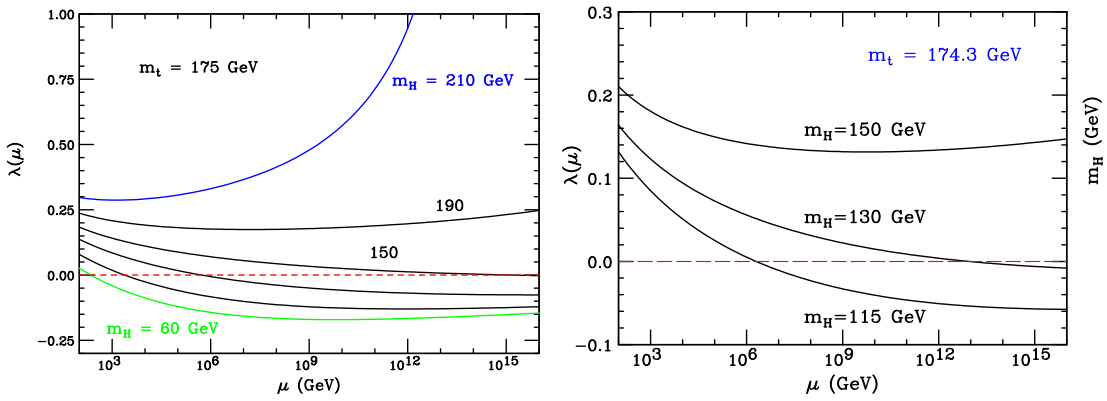

Figure 1.11: *Dependence of quartic coupling constant λ on the energy scale μ.*

$$\begin{aligned}
\frac{dg(\mu)}{d\ln\mu} &= \frac{1}{16\pi^2}\left(-\frac{19}{6}g^3\right), \\
\frac{dg'(\mu)}{d\ln\mu} &= \frac{1}{16\pi^2}\left(\frac{41}{6}g'^3\right), \\
\frac{dg_s(\mu)}{d\ln\mu} &= \frac{1}{16\pi^2}\left(-7g_s^3\right),
\end{aligned} \tag{1.56}$$

$$\frac{dm_t(\mu)}{d\ln\mu} = \frac{1}{16\pi^2}\left(9\left(\frac{m_t}{v}\right)^3 - \left(8g_s^2 + \frac{9}{4}g^2 + \frac{17}{12}g'^2\right)m_t\right).$$

For small m_H with respect to m_t it is possible that

$$\frac{d\lambda(t)}{dt} < 0 \qquad t = \ln\left(\frac{\Lambda}{\mu}\right); \tag{1.57}$$

thus λ can become negative. In Figure 1.11 the dependences of $\lambda(\mu)$ from μ for two different Higgs mass are shown. One can also invert the relations in Figure 1.11, obtaining the m_H limits as a function of Λ (Figure 1.12). The precise measurement of the top mass is crucial in order to impose a lower bound on the Higgs mass. The top mass effect on this limit is shown in Fig. 1.13, where different values of m_t change the curve in Figure 1.12.

It is remarkable that if $m_t \sim (174 \div 178)$ GeV and $\Lambda \sim M_{Planck}$, then m_H must be larger than 130 GeV. On the other side, if $m_H < 130\,\text{GeV}$ (and m_t is in the range indicated) the SM breaks down well below M_{Planck}: new physics must appear at the scale where SM breaks down.

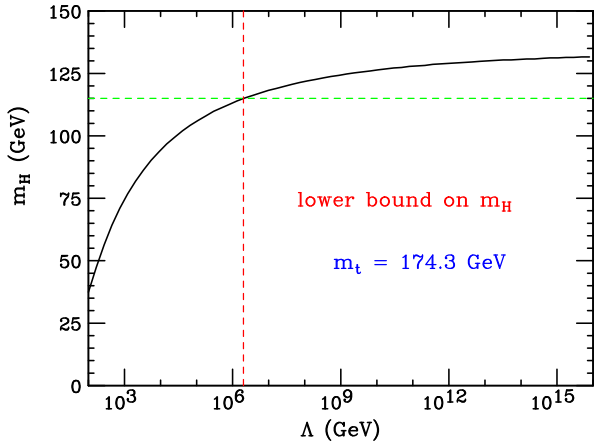

Figure 1.12: *Higgs boson mass lower limit as a function of the breakdown energy scale* Λ.

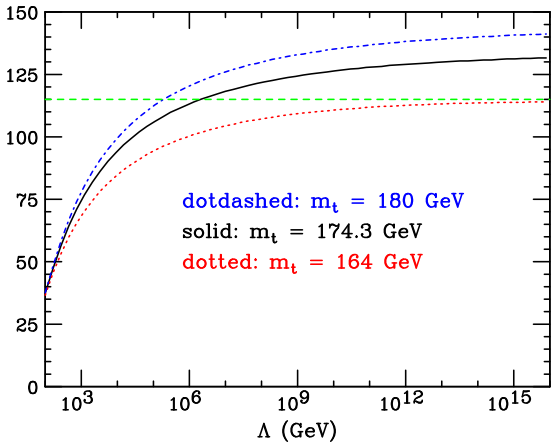

Figure 1.13: *Top mass effect on Higgs boson mass lower limit.*

1.3.4 Upper Limit on the SM Higgs

Similarly an upper bound on m_H (with mild dependence on m_t) can be obtained from the requirement that up to the scale Λ no Landau pole appears. In fact [26] if we consider the renormalization group equation for λ in the simplified case when gauge and Yukawa couplings are neglected, we can find:

$$\beta(\lambda) = \frac{3\lambda^2}{2\pi^2}\,. \tag{1.58}$$

The variation of the coupling with the scale is summarized by the β-function:

$$\beta(\lambda) = \mu\frac{d\lambda}{d\mu}\,. \tag{1.59}$$

Combining Eq. (1.59) with Eq. (1.58), it is possible to compute the behaviour of the coupling constant as a function of the scale:

$$\frac{1}{\lambda(\mu)} = \frac{1}{\lambda(\Lambda)} + \frac{3}{2\pi^2}\ln\frac{\Lambda}{\mu}\,; \tag{1.60}$$

isolating $\lambda(\Lambda)$ in equation (1.60) we find:

$$\lambda(\Lambda) = \frac{\lambda(\mu)}{1 - \lambda(\mu)\frac{3}{2\pi^2}\ln\left(\frac{\Lambda}{\mu}\right)}\,. \tag{1.61}$$

We can see that $\lambda(\Lambda)$ has a Landau pole for

$$\Lambda = \mu\exp\left(\frac{2\pi^2}{3\lambda(\mu)}\right)\,. \tag{1.62}$$

Vacuum stability requirement forces Eq. (1.62) to be:

$$\Lambda < \mu\exp\left(\frac{2\pi^2}{3\lambda(\mu)}\right)\,. \tag{1.63}$$

Thus for energy scale $\mu = m_H$,[9] and remembering that $m_H^2 \sim 2\lambda(m_H)v^2$, at tree level, an upper bound on Higgs mass is obtained:

$$\Lambda < m_H\exp\left(\frac{4\pi^2 v^2}{3m_H^2}\right)\,. \tag{1.64}$$

[9]The Higgs mechanism has to be valid, at least, up to this scale of energy, in order to performs its task.

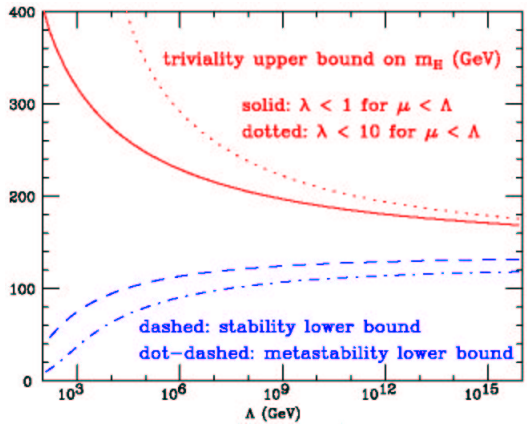

Figure 1.14: *Upper and lower bounds on m_H.*

The relation (1.64) implies that for a given Higgs boson mass, there is a finite cutoff energy at which the description of the theory as a fundamental theory stops making sense. This means that the standard Higgs model can only be regarded as an effective theory valid below this cutoff . The theory of a relatively light weakly coupled Higgs boson can be self-consistent to a very high energy. Conversely, Higgs mass has not to be too large. For example, if the theory has to be valid up to a typical Grand Unified Theory scale energy, 10^{16} GeV, then the Higgs boson mass has to be less than about 170 GeV. Since we have computed the β-function in perturbation theory, this answer is only reliable at energy scales at which $\lambda(\mu)$ (as well as the Higgs boson mass) is small. Non-perturbative lattice calculations are available. Estimates indicated that if the theory has to be valid up to 4 TeV, the mass of the Higgs boson has to be less than about 800 GeV.

The upper limit (1.64) is the so called *"triviality bound"*, in fact from Eq. (1.63) it is easy to find that:

$$\lambda(\mu) < \frac{2\pi^2}{3\ln\left(\frac{\Lambda}{\mu}\right)}, \tag{1.65}$$

which shows that for $\Lambda \to \infty$, $\lambda \to 0$. So if the SM is valid up to the Grand Unification Theory scale, Higgs sector interactions are weak.

Chapter 2

The LHC Collider and the CMS Detector

2.1 The Large Hadron Collider (LHC)

In order to explore the Electroweak Symmetry Breaking Mechanism up to the TeV scale, a high luminosity and high centre-of-mass energy collider is needed. The perfect machine for this task would have been the Superconducting Super Collider (SSC) which should have been built in the USA. It had been designed to collide beams of protons at a centre-of-mass energy of 40 TeV. Unfortunately the project was terminated because of financial problems. Therefore the best candidate for the investigation of the EWSB mechanism in general, and of the WW fusion process in particular, will be the Large Hadron Collider at CERN which will start running in 2007.

2.1.1 Design of the LHC Machine

As stated before, the discovery of any kind of new physics in the TeV region needs a machine able to collide high energy particles with very high luminosity. Since the energy loss due to synchrotron radiation of a particle of mass m and energy E turning in a ring of radius R is proportional to $E^4/(m^4 R)$, an accelerator ring too large to be affordable would be needed to accelerate electrons to high energies. On the other hand, the idea of a proton-anti-proton collider

Table 2.1: *LHC parameters for $p-p$ and $Pb-Pb$ collisions.*

Parameter	**p − p**	**^{208}Pb^{82+}**
Center-of-mass energy (TeV)	14	1148
Number of particles per bunch	1.1×10^{11}	$\sim 8\times10^{7}$
Number of bunches	2808	608
Design Luminosity ($cm^{-2}s^{-1}$)	10^{34}	2×10^{27}
Luminosity lifetime (h)	10	4.2
Bunch length (mm)	53	75
Beam radius at interaction point (μm)	15	
Time between collisions (NC)	24.95	124.75
Bunch crossing rate (MHz)	40.08	0.008
Circumference (km)	26.659	
Dipole field (T)	8.3	

has to be discarded because it would be too difficult to produce enough anti-particles to reach the needed luminosity. That is why a *proton-proton* collider is the right solution for very high energy physics.

The LHC accelerator will be built in the existing 27 km long tunnel where the LEP collider was installed. The maximum beam momentum and the maximum centre-of-mass energy are limited by the magnetic field intensity; LHC will reach a centre-of-mass energy of 14 TeV. It will run with a bunch crossing rate of 40 MHz (with a bunch structure such that only 80% of the bunches will be filled [32]). During the first three years of running the luminosity will be 2×10^{33} cm^{-2}s^{-1} (usually called "Low Luminosity"). After this initial period the so called "High Luminosity" of 10^{34} cm^{-2}s^{-1} will be reached.

LHC will not only accelerate protons at high luminosity but it will also be able to accelerate heavy ions. Some LHC parameters are given in Table 2.1.

2.1.2 LHC Experimental Environment

Since protons are not elementary particles, hard collisions can be thought of as parton collisions in which the interacting particles carry only a fraction of the proton energy determined by the Parton Density Functions (PDFs). This means that the initial total energy and the rest frame of the interaction are

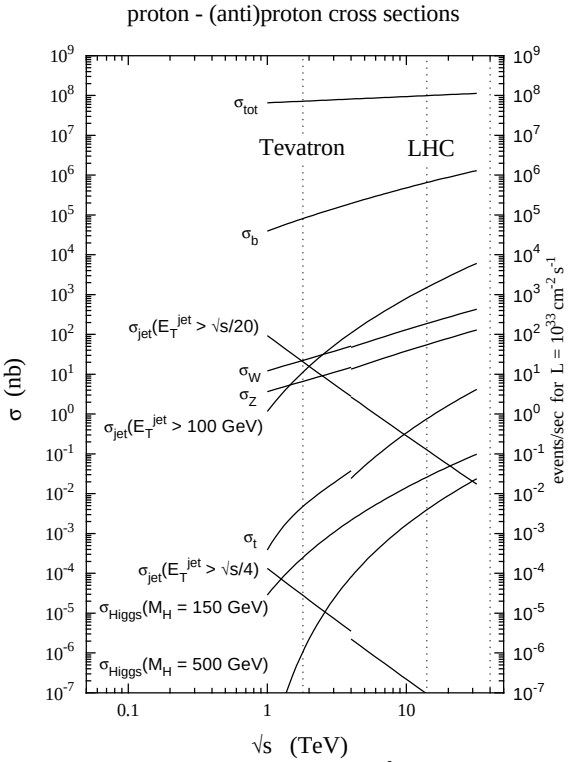

Figure 2.1: *Cross sections and event rates of several processes as a function of the center-of-mass energy of* proton-proton *collisions [33].*

not known: we only know the initial transverse energy of the system. On the other hand this situation has the advantage that a wide range of energies can be explored with fixed-energy beams.

Figure 2.1 shows cross sections for different processes as a function of the centre-of-mass energy in $p-p$ collisions. The total cross section is very large while the cross section of interesting events, for example Higgs production, lies orders of magnitude below it. LHC will compensate the low Higgs production cross sections through its very high luminosity; the drawback is that the total event rate becomes so high that several interactions overlap in the same bunch crossing. Every interesting event will have several "minimum bias" events piled up on the top of it. Considering the bunch crossing rate of 40 MHz, the design luminosity of 10^{34} cm^{-2}s^{-1} and the total non-diffractive inelastic $p-p$ cross section of 55 mb predicted by PYTHIA, the average number of piled up events will be 17.3 for each bunch crossing. This high interaction rate is not only very

demanding for detectors trigger and data acquisition systems but also implies an intense radiation environment. All LHC detectors should have a very fast response time and the readout electronic should also be very fast. Moreover, to cope with event pile-up, high granularity is required to avoid particle overlap.

2.1.3 LHC Experiments

The two proton beams intersect at four points where experiments are placed. Two of these house the ALICE detector [34], which will be used for the study of heavy ion collisions, and LHC-B [35], a detector optimized for the study of *b-mesons* and *b-Baryons*. The two other regions house the general-purpose experiments ATLAS [36] and CMS. Since their physics goals are similar, these two detectors share many common features:

- precision electromagnetic calorimetry;
- good muon identification and precision momentum measurement through large magnet systems;
- lepton identification and precision measurement up to $\eta = 2.5$;
- calorimetry with large η coverage in order to obtain the required missing E_T resolution.

The main differences between these two detectors are related to the magnetic field configuration. The Compact Muon Solenoid (CMS) uses a big superconducting solenoid which generates a strong solenoidal field, while ATLAS uses a toroidal field produced by three sets of air-core toroids complemented by a small inner solenoid. The CMS solenoidal magnet supplies a very intense field and the resulting system is very compact: calorimeters can be installed inside the magnet improving electron and photon energy measurement. Precise tracking exploits both the constant field within the magnet and the field inside the return yoke. Among the disadvantages of this kind of setup we have to consider that multiple scattering within the yoke degrades the muon system resolution. On the other hand ATLAS, using a toroidal magnetic field, has the advantage that p_T resolution does not have any dependence on pseudorapidity. Moreover

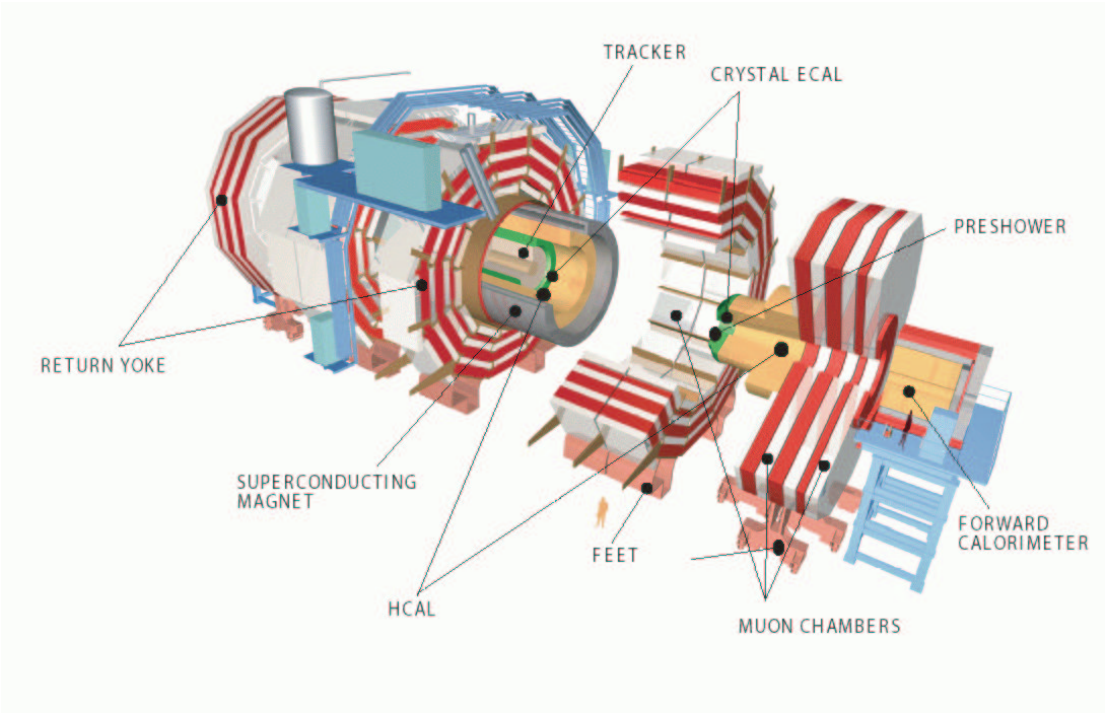

Figure 2.2: *The CMS detector. Barrel wheels are numbered Z= -2, -1, 0, 1, 2.*

an air-core toroid together with excellent detector alignment allows a good momentum resolution even without the inner tracker. Figures 2.3 and 2.2 show schematic pictures of the ATLAS and CMS detectors. The CMS experiment is described in a more detailed way in Section 2.2.

2.2 The Compact Muon Solenoid Detector (CMS)

The main goal of LHC will be the investigation of the Electroweak Symmetry Breaking Mechanism. The two general-purpose experiments ATLAS and CMS should therefore be able to reveal all kinds of new physics. The discovery potential of these detectors is very high since, considered the LHC centre-of-mass energy, it will be possible to detect new particles up to masses of $3-5$ TeV. To achieve this task, the CMS Collaboration designed a very compact detector characterized by a strong magnetic field generated by a 4 T superconducting

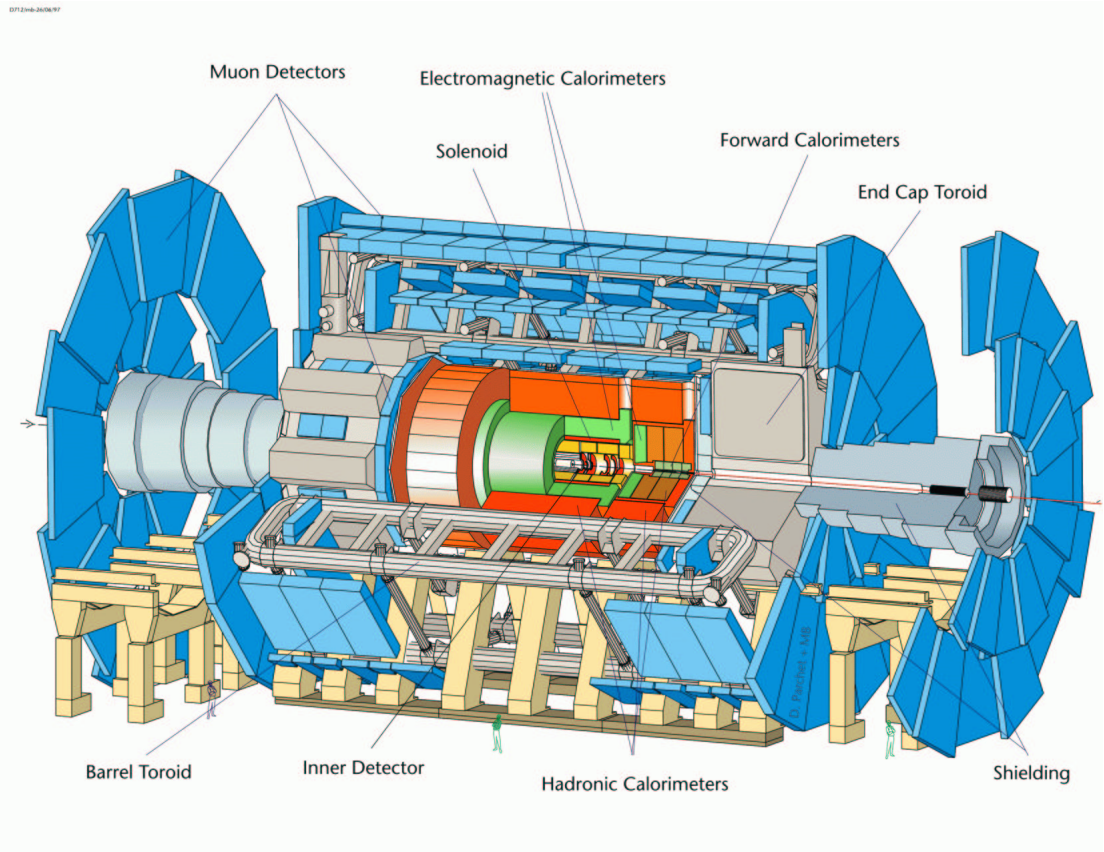

Figure 2.3: *The ATLAS detector.*

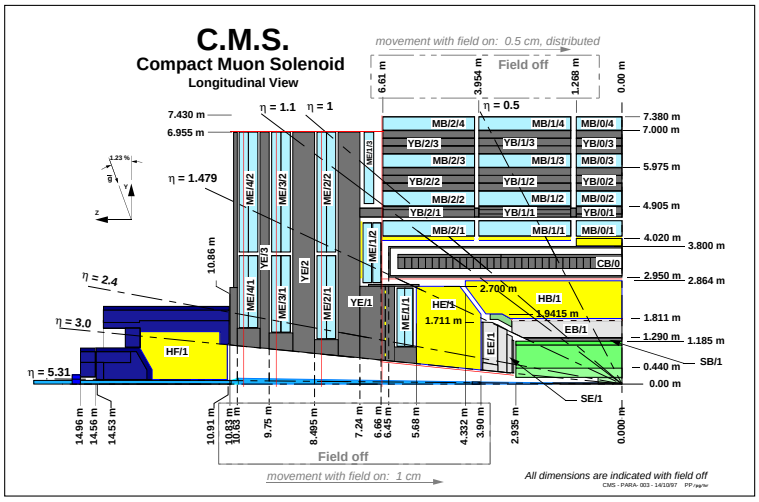

Figure 2.4: *Longitudinal view of one quarter of the CMS detector.*

solenoid. The next sections provide a general description of this detector.

2.2.1 Overall Design

The CMS [37] detector is a cylindrical barrel 21.6 m long closed by two endcap disks, with a diameter of 15 m and a total weight of almost 12500 tonnes. Figure 2.4 shows a longitudinal view of one quarter of the CMS detector while the cross sectional view of the barrel region is shown in Fig. 2.5.

The CMS coordinate frame is a right-handed system where the x axis points to the centre of the LHC ring, the y axis points upward and the z axis is parallel to the beam. However reconstruction algorithms use a spherical coordinate system based on the distance r from the z axis, the azimuthal angle ϕ with respect to the x axis and the pseudo-rapidity η. Pseudo-rapidity is a very convenient quantity to describe physics at LHC. Since the centre-of-mass of the interaction could be boosted along the beam direction it is very useful to use experimental quantities that are invariant under such boosts as the transverse momentum p_T or the *rapidity*. Rapidity is defined as:

$$y = \frac{1}{2} \ln \frac{E + p_z}{E - p_z} \tag{2.1}$$

and is often used to describe angular distributions because it has the property

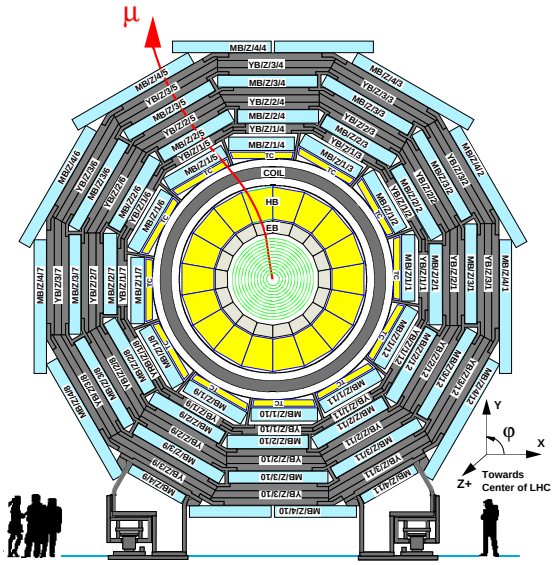

Figure 2.5: *Transverse view of the barrel region of the CMS detector.*

that the shape of dN/dy distributions is invariant under boosts along the z direction. For $p \gg m$ the rapidity is approximated by the *pseudorapidity*:

$$\eta = -\ln \tan \frac{\theta}{2}, \tag{2.2}$$

where θ is the angle between the particle momentum and the z axis. The pseudorapidity has the advantage that it depends only on θ and can be also used for particles of unknown mass and momentum.

The basic design criteria of CMS are:

- a redundant muon system, to achieve precise muon identification and momentum measurement;
- high resolution electromagnetic calorimeters for precise energy measurement of photons and electrons;
- a high quality inner tracking system to allow good reconstruction of particle tracks even in the most difficult experimental conditions.

To achieve these objectives CMS will use a design driven by the choice of its magnet; a 13 m long superconducting solenoid [38] with a diameter of 5.9 m

will supply a 4 T magnetic field, which is kept uniform by a massive iron return yoke. This magnet will be cooled with liquid helium. The yoke houses the muon system composed of drift tube detectors in the barrel region and cathode strip chambers in the endcaps (up to $|\eta| < 2.4$) complemented by a system of resistive plate chambers with a coverage of $|\eta| < 2.1$. The muon system is described in detail in Section 2.2.5.

The innermost tracking detector has to cope with a very high track multiplicity. Therefore, to allow precise vertex reconstruction and reliable *b-tagging*, a very fine granularity is needed. For this reason a silicon pixel detector was chosen; it consists of three barrel layers and two forward disks. Moreover, outside the pixel detector, a silicon strip detector is installed, with a radius of about 1.2 m. The whole silicon system (described in Section 2.2.2) allows charged track reconstruction with at least 12 measurement points and a coverage up to $|\eta| < 2.5$.

The calorimeter system is also placed inside the solenoid. It has therefore to be thick enough to avoid hadronic cascades leaking into the muon system. The electromagnetic calorimeter (ECAL) is a homogeneous calorimeter composed of $PbWO_4$ scintillating crystals covering the region $|\eta| < 3$. In the endcaps it will be supplemented by a lead/silicon preshower detector in order to improve the pion rejection efficiency and the resolution in the determination of the electron and photon direction. A more detailed description of the ECAL is given in Section 2.2.3.

The hadronic sampling calorimeter consists of plastic scintillators plates and copper alloy absorbers. It has the same pseudorapidity coverage as the ECAL but is complemented by a very forward calorimeter (HF) which reaches $|\eta| < 5.3$, improving the hermeticity of the detector. The HCAL is described in Section 2.2.4.

2.2.2 The Tracker

The inner tracker [39, 40] will provide reconstruction of high-p_T charged tracks in the region $|\eta| < 2.5$ with high efficiency and momentum resolution. The detector is composed of several layers of silicon detectors. The first layers are crucial for the measurement of the impact parameter and, since they are close to

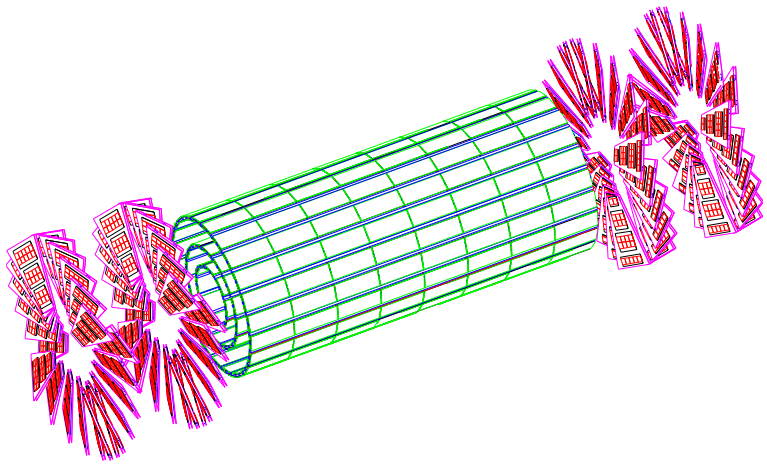

Figure 2.6: *Three-dimensional view of the full pixel detector.*

the interaction point, they have to cope with a very high particle flux; therefore, finely segmented pixel detectors are used. The other layers are composed of single-sided silicon strip detectors extending up to $r = 110$ cm and $|z| = 270$ cm. The short distance of the device from the interaction point imposes special requirements of radiation hardness.

The Pixel Detector The pixel detector, thanks to its high-resolution three-dimensional measurement, will allow excellent charged track reconstruction and impact parameter measurement, identification of τ and *b-jets* and three dimensional vertex reconstruction. The pixel detector is composed of three barrel layers at mean radii of 4.4 cm, 7.3 cm and 10.2 cm, extending for a total length of 53 cm and two endcap disks extending in radius from 6 to 15 cm placed on each side, at $|z| = 34.5$ cm and 46.5 cm. This layout will guarantee at least two pixel hits for tracks originating within $2\,\sigma_Z$ of the nominal collision point, up to about $|\eta| < 2.2$. Fig. 2.6 shows a three-dimensional representation of the pixel detector.

The full detector consists in a total of 4.4 millions of square *n-type* silicon pixels with a size of 150μm $\times$ 150μm on a *n-type* silicon substrate. A spatial resolution of $\sim 15\mu$m is obtained. With this kind of layout, standalone track reconstruction, that requires three hits per track, will also be possible with good efficiency. However, in the initial low-luminosity phase only two barrel layers

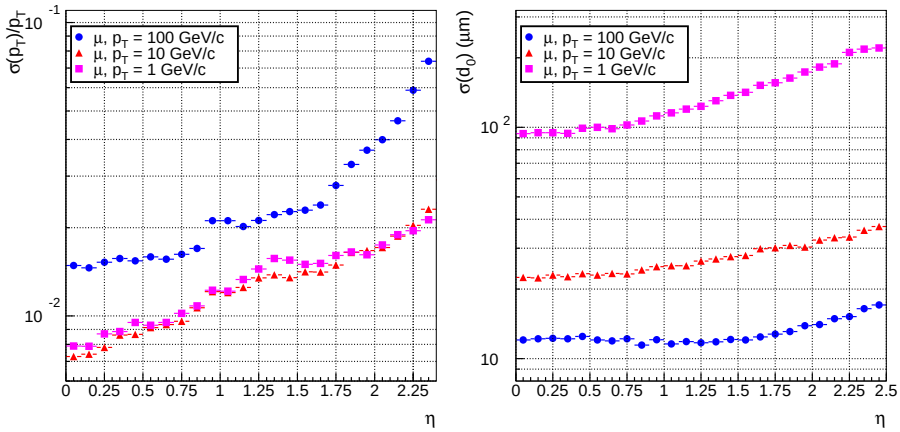

Figure 2.7: *Resolution of the tracker on the transverse momentum (left) and the transverse impact parameter (right) as a function of pseudorapidity, for single muons with transverse momentum of 1, 10, 100 GeV/c [41].*

and one endcap disk will be installed. The standalone track reconstruction will therefore not be possible and the region where each track gives two hits will be limited to $|\eta| < 2.0$.

The Silicon Microstrip Detector In addition to the pixel detector the tracker is composed of several layers of silicon microstrip detectors; they provide high spatial precision and time resolution combined with adequate radiation hardness. There are about 15000 microstrip detectors, with a pitch size from 80 to 180 μm. In the inner part they are organized in four barrel layers and three small forward disks while in the outer part there are six barrel layers and nine forward disks. Some of the modules will be "stereo" modules, composed by two detectors mounted back-to-back with the strip rotated by 100 μrad in order to provide a measurement in the coordinate orthogonal to the strips. Fig. 2.7 shows the resolution of the full tracker for the transverse momentum and the impact parameter.

2.2.3 The Electromagnetic Calorimeter

The physics process that imposes the strictest requirements on the electromagnetic calorimeter (ECAL) [42] performance is the intermediate mass Higgs

decay into two photons: the goal is a 1% two-photon invariant mass resolution. The natural choice to achieve this task is a homogeneous calorimeter; the CMS collaboration chose a crystal calorimeter composed of about 80000 lead tungstate (PbWO4) crystals. Lead tungstate is a fast, radiation-hard scintillator characterized by a small Moliere radius (21.9 mm) and short radiation length (8.9 mm). In the barrel the crystals are 230 mm long while in the endcaps they are 220 mm long, corresponding to 25.8 and 24.7 radiation lengths, respectively; the short radiation length allows a good shower containment in the limited space available for the ECAL.

The calorimeter system should also be able to distinguish between showers initiated by neutral pions and photons, or charged pions and electrons, which require good granularity. Crystals are trapezoidal with a square front face of $22 \times 22\,\mathrm{mm}^2$ in the barrel and $30 \times 30\,\mathrm{mm}^2$ in the endcaps, matching the Moliere radius. This granularity is not high enough in the endcap regions where a preshower device with higher granularity will be used; it consists of two lead radiators and two planes of silicon strip detectors with a total radiation length of 3 X_0. This detector will allow rejection of photon pairs from π^0 decays which may fake a single photon.

In the barrel scintillator light is collected by silicon avalanche photo-diodes while, in the endcaps, vacuum photo-triodes are used.

As shown in Fig. 2.8, the geometric coverage of the ECAL extends up to $|\eta| < 3.0$.

Usually the energy (E) resolution of a calorimeter is parametrized as

$$\left(\frac{\sigma}{E}\right)^2 = \left(\frac{a}{\sqrt{E}}\right)^2 + \left(\frac{\sigma_n}{E}\right)^2 + c^2, \tag{2.3}$$

where a is called stochastic term, corresponding to the statistical fluctuations in the number of primary processes that generate the signal, σ_n is the noise term including the energy equivalent of the electronic noise and pile-up effects and c is a constant term related to the calibration of the calorimeter. The different contributions to the energy resolution as a function of the measured energy are shown in Fig. 2.9.

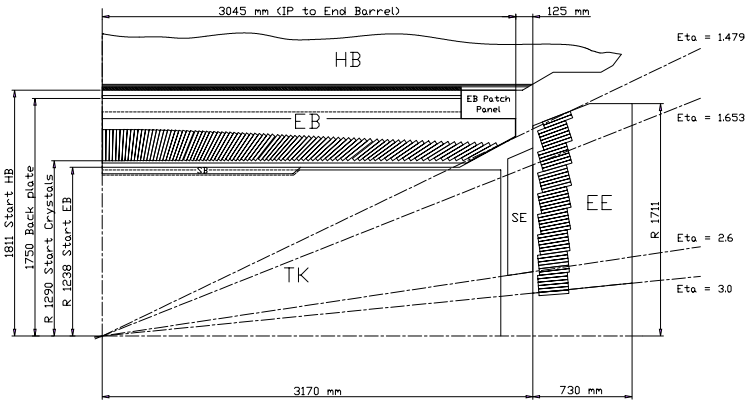

Figure 2.8: *Longitudinal view of one quarter of the ECAL.*

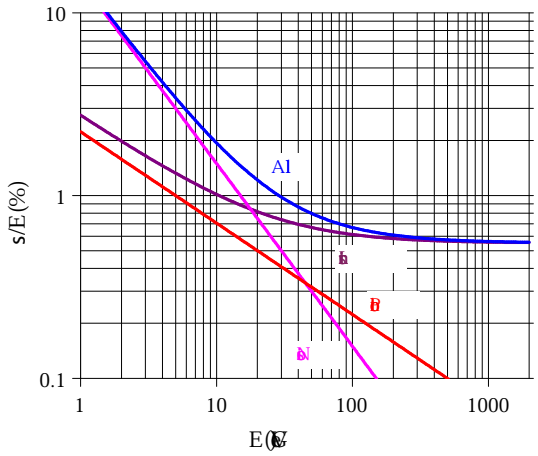

Figure 2.9: *Different contributions to the energy resolution of the ECAL [42]. The curve labeled "intrinsic" includes the shower containment and a constant term of 0.55%.*

2.2.4 The Hadron Calorimeter

The hadron calorimeter (HCAL) [43] surrounds the ECAL and works together with it to measure direction and energy of jets and transverse missing energy. One of the main design requirement for the HCAL is therefore a high hermeticity. Moreover, the identification of forward jets is very important for the rejection of many backgrounds. For these reasons, the barrel and the endcap parts, which cover up to $|\eta| = 3.0$, are complemented by a very forward calorimeter which extends the coverage up to $|\eta| = 5.3$. The barrel and the endcap calorimeters with active plastic scintillator layers interleaved with brass absorber plates; the read out system is composed of wavelength-shifting fibers. Only the first layer is read out separately while all others are read out together in towers of size $\Delta\eta \times \Delta\phi = 0.087 \times 0.087$. In the barrel region full shower containment is not possible within the magnet volume and an additional "tail catcher" is placed outside the magnet.

The very forward calorimeter is placed outside the magnet yoke, 11 m from the interaction point. It uses quartz fibers parallel to the beam, inserted in steel absorber plates. The energy resolution is $\sigma/E \sim 65\%\sqrt{E} \oplus 5\%$ in the barrel; $\sigma/E \sim 85\%\sqrt{E} \oplus 5\%$ in the endcaps and $\sigma/E \sim 100\%\sqrt{E} \oplus 5\%$ (E in GeV) in the very forward calorimeter.

2.2.5 The Muon System

The tasks of the muon system [44] are the identification of muons and measurement of their transverse momenta with or without the contribution of the inner tracker. Muon detection is of central importance because it provides a clean signature for many physics processes playing an important role. The muon system is integrated in the iron return yoke of the magnet. The material in front of the muon system shields the detector from charged particles other than muons allowing muon identification even at high luminosity running conditions. The CMS muon system is composed of three independent subsystems using different technologies. In the barrel, where the track occupancy is low and the magnetic field is well contained in the iron plates of the return yoke, drift tube detectors (DT) are installed. In the endcap region, Chatode Strip Chambers (CSC) are used because of their good spatial and time resolution which allows usage with

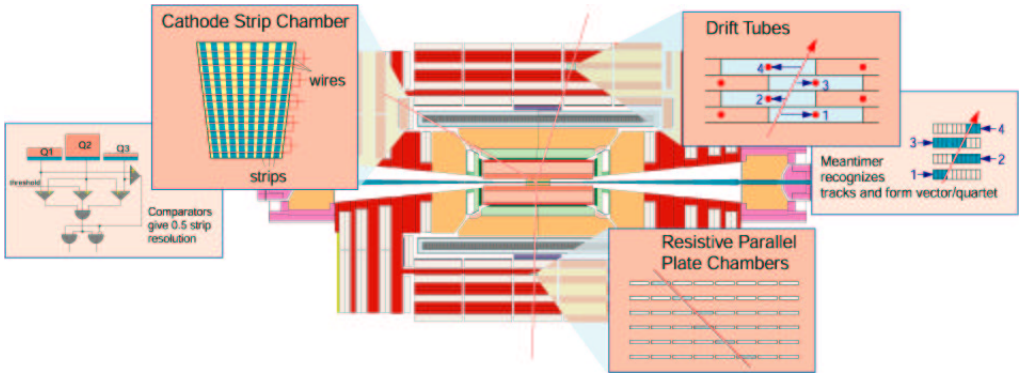

Figure 2.10: *Longitudinal view of the muon system.*

high occupancy levels and in presence of large inhomogeneous magnetic fields. Both in the barrel and in the endcaps the system is complemented by resistive plate chambers (RPC); they have a limited spatial resolution but fast response and very good time resolution, very useful in bunch crossing identification and triggering. They are also used in addition to DTs and CSCs in the p_T measurement thereby obtaining redundancy. The RPC system covers the region $|\eta| < 2.1$. The muon system layout is shown in Fig. 2.10.

DT chambers are arranged in four *stations* (*i.e.* concentric cylinders) named MB1, MB2, MB3 and MB4; each station consists of twelve chambers except for MB4 which is composed of fourteen chambers. CSCs are arranged in four disks (also called *stations*), placed between the iron disks of the yoke, and labeled ME1, ME2, ME3, ME4.

2.2.6 The CMS Trigger

As already seen in Section 2.1.2, the LHC experimental environment is very demanding for the trigger system: at high luminosity the total event rate is of the order of 10^9 Hz while the rate of interesting events is very small. Fig. 2.11 shows cross sections and event rates for the production of various final states as a function of their mass.

The maximum storage rate for read out data is about 100 Hz; the goal of the trigger system is therefore to perform such huge on-line selection. Moreover the time available to perform this selection is limited: with a bunch crossing

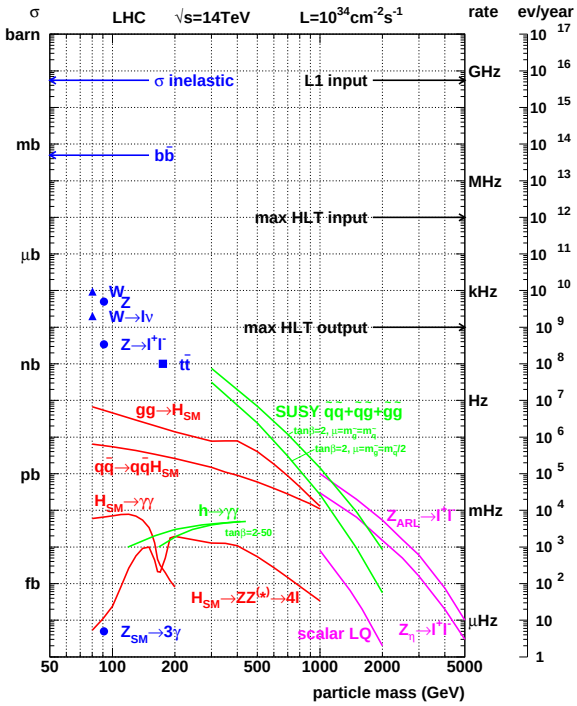

Figure 2.11: *Cross section and event rates at* 10^{34} $cm^{-2}s^{-1}$ *as a function of the mass of produced objects.*

rate of 40 MHz decisions must be taken every 25 ns, a time too small even to read out all raw data from the detector.

The trigger must be able to select events on the basis of their physics, making it necessary to use sophisticated on-line selection algorithms. To achieve this, the trigger selection will be organized in several steps (called *levels*), where each step refines the selection using only a part of the available data. In this way, higher trigger levels have to process fewer events and have more time available to use more complicated algorithms.

In order to reduce possible dead time, the first step of the CMS trigger, the Level-1 trigger, is implemented on dedicated programmable hardware. The Level-1 uses data from the calorimeters and the muon detectors with coarse granularity to reduce the event rate to a level acceptable for the Data Acquisition System (DAQ). At the beginning the CMS DAQ system will be able to handle an event rate of up to 50 kHz. Later, when LHC reaches the full design luminosity, it will be increased to 100 kHz. Events selected by the Level-1 trigger go through the High Level Trigger (HLT) selection. This step is based on software running on a farm of commercial processors. Within the HLT, further logical steps can be identified (Level-1 and Level-2) but this classification is somehow arbitrary.

In the following a brief discussion of the Level-1 trigger is given.

2.2.6.1 The Level-1 Trigger

The Level-1 trigger [45], to cope with a bunch crossing rate of 40 MHz, is subdivided in a sequence of blocks executing a group of operations within 25 ns. At every bunch crossing each block passes its results to the next block and analyzes a new event. In the meantime the complete detector data are stored in pipeline memories which are able to store data from 128 bunch crossings. Therefore, the Level-1 decision must be taken within 3.2 μs including the transmission time between the detector and the counting room (up to 600 ns) and, in the case of DT detectors, the electron drift time (up to 400 ns). The Level-1 trigger is composed of three subsystems: the Calorimeter Trigger, the Muon Trigger and the Global Trigger.

The Calorimeter and the Muon Trigger identify “trigger objects" but do not perform any selection themselves. Trigger objects can be isolated and non- iso-

lated electron/photons, forward, central and τ-jets and muons. The best four candidates are delivered to the Global Trigger together with the measurement of their position, their transverse energy or momentum and a quality flag. The Global Trigger selects the events using programmable trigger algorithms. Up to 128 of these algorithms can run in parallel and they select events requiring several objects with energy or momentum above predefined thresholds or considering topological conditions and correlation between objects.

The calorimeter trigger identifies isolated electrons/photons (they cannot be distinguished at this stage), non isolated electrons/photons, central jets, forward jets and τ-jets. Moreover it sends to the Global Trigger also a measurement of the total and the missing energy of the event.

The Muon Trigger [45] identifies muons by reconstructing their position and transverse momentum, provides bunch crossing assignment with high efficiency as well. It will not cover the whole pseudorapidity range covered by the muon system: its geometric acceptance will be limited to $|\eta| < 2.1$. The whole muon system contributes to the trigger giving, with its redundancy, a robust and reliable trigger with high efficiency and good background rejection. The best muon candidates from the different subsystems (DTs, CSCs and RPCs) are matched by the Global Muon Trigger (GMT) by combining their parameters in an optimal way. The simplest Level-1 muon trigger is based on a threshold on the p_T of GMT tracks.

The Level-1 Trigger Table Even if Level-1 trigger algorithms can use complex criteria based on topological conditions and correlations, the best choice, whenever possible, is to use "inclusive" criteria in order to avoid biasing the selected sample. The simplest trigger criteria are in general the requirements of one (single-object trigger) or two (di-object trigger) objects of the same type with E_T or p_T higher than a certain threshold. Another possibility is the request of multiple objects of the same or different type (multiple-object trigger). Of course in the case of special channels specific exclusive algorithms can be used. The choice of Level-1 thresholds is driven by the maximum event rate (bandwidth) handled by the DAQ system. Even if the DAQ is thought to accept an event rate of 50 kHz in the first period and 100 kHz in the following, only one third of this bandwidth will be allocated using the rest as safety margin [41].

Table 2.2: *L1 trigger table at low luminosity [41].*

Trigger	**Threshold** (GeV or GeV/c)	**Rate** (kHz)	**Cumulative Rate** (kHz)
Inclusive isolated electron/photon	29	3.3	3.3
Di-electrons/di-photons	17	1.3	4.3
Inclusive muon	14	2.7	7.0
Di-muons	3	0.9	7.9
Single tau-jet trigger	86	2.2	10.1
Two tau-jets	59	1.0	10.9
1-jet, 3-jets, 4-jets	177, 86, 70	3.0	12.5
Jet $\times$ *ET miss*	88×46	2.3	14.3
Electron $\times$ *Jet*	21×45	0.8	15.1
Minimum-bias (calibration)		0.9	16.0
Total			16.0

The available bandwidth is then shared between the Level-1 objects described before.

The result is a set of thresholds called trigger table. In Table 2.2 and Table 2.3 the trigger tables at low and high luminosity respectively are shown.

2.2.6.2 The High Level Trigger (HLT)

The second step of the on-line selection is the High Level Trigger [41]. Its goal is to reduce the event rate from the maximum Level-1 event rate of 100 kHz to a rate of the order of 100 Hz. This is the maximum rate acceptable for storage and further processing of events which will have, on average, a size of almost 1 MB.

The HLT is fully implemented on software running on a farm of commercial processors, each processing one full event at a time. The result is a fully programmable system which allows complete flexibility of the algorithms. The only limits come from the maximum available CPU time and bandwidth. Moreover, the use of standard commercial components not only leads to significant economies in the cost of hardware but also allows to benefit from future technology developments, especially for what regards CPU speed and network band-

Table 2.3: *L1 trigger table at high luminosity [41].*

Trigger	**Threshold** (GeV or GeV/c)	**Rate** (kHz)	**Cumulative Rate** (kHz)
Inclusive isolated electron/photon	34	6.5	6.5
Di-electrons/di-photons	19	3.3	9.4
Inclusive muon	20	6.2	15.6
Di-muons	5	1.7	17.3
Single tau-jet trigger	101	5.3	22.6
Two tau-jets	67	3.6	25.0
1-jet, 3-jets, 4-jets	250, 110, 95	3.0	26.7
Jet $\times$ *ET miss*	113×70	4.5	30.4
Electron $\times$ *Jet*	25×52	1.3	31.7
Muon $\times$ *Jet*	15×40	0.8	32.5
Minimum-bias (calibration)		1.0	33.5
Total			33.5

width.

The code used in the HLT will be identical to the code used in the off-line data analysis. Therefore, it will benefit from the continuous improvements in the reconstruction software. This flexibility will also allow to adapt the system to unforeseen conditions or developments.

The goal of the High Level Trigger is to discard unwanted events as soon as they are recognized as such. To achieve this task the selection is organized in a chain of logical steps. Each of them consists of progressively more sophisticated and CPU-time consuming selection algorithms in order to reduce the event rate to a level acceptable for the following step. It is customary to identify two steps, the Level-2, where the data of the calorimeter and the muon detector are used, and the Level-3, which also uses the information from the inner tracker, for which reconstruction is more time consuming. The HLT reconstruction algorithms are implemented according to the principle of regional reconstruction: the objects are reconstructed using only the information coming from a limited region of one (or more) subdetectors. This leads to significant CPU savings and allows to discard uninteresting events without reading the full event.

Chapter 3

CMS Software and Event Simulation

In a modern high-energy physics experiment, most of the data analysis is done using computers [46]. When the data from LHC will be processed, only a very small fraction of the events selected will ever be directly examined by the physicists using visualization programs. Most tasks, such as monitoring, triggering, calibration, are computerized. To handle these data amounts efficiently and reliably, many software tools have been developed for physics processes simulation, detector simulation, event triggering and reconstruction, and data analysis, to name just a few.

For this study signal and background events were generated using the PYTHIA [47] generator. Then they were processed with the fast simulation package CMSJET [48], which gives a reasonable approximation of the detector efficiency and acceptance.

This Chapter gives a brief overview of the most common software tools in use at the CMS experiment, especially of those related to this thesis, along with a description of the generated samples.

3.1 Priority and Challenges for CMS software

The major challenges for LHC software and computing today include:

- Events are big (raw event is 2MB).

- At the design luminosity of $10^{34}\,\mathrm{cm}^{-2}\mathrm{s}^{-1}$ approximately 17 minimum bias events per crossing are produced. With the bunch crossing time so short (25 ns) a realistic detector digitization has to take into account the fact that events from different bunch crossings contribute to the digitization. At least 9 crossings (-5 to +3) contribute to calorimetry digitization while muon digitization is affected by even more crossings. Typically, information from more than 150 (9×17) minimum bias events is needed for each signal event. Thus for 1 million signal events it would be required to generate more than 150 millions minimum bias events. This is impossible with the current available CPU, storage etc. Instead the minimum bias events are included in the digitization step and the simulated minimum bias events are recycled. For that a data set consisting of a few hundred thousands minimum bias events has been created. For each signal event the necessary minimum bias events are randomly selected in a straightforward manner. Problems can arise when one single minimum bias event by itself would trigger the detector, since this event would trigger many times. Therefore it is necessary to filter the minimum bias events. The events removed have to be taken into account. The advantage of this approach is that it is easy to study the same signal events at different luminosities and also with and without pile-up. The size of the 150 minimum bias events which have to be read in for each signal event is greater than 50MB. This results in a massive data movement problem.

- The CMS Tracker is immersed in a high magnetic field of 4 Tesla. The tracks of low momentum charged particles loop in the magnetic field and can persist for many crossings. This requires track finding in a very complex environment.

- The total tracker material adds up to 1 radiation length resulting in lots of bremsstrahlung for the electrons. This makes matching tracks to calorimeter clusters a non-trivial task (see Figure 3.1).

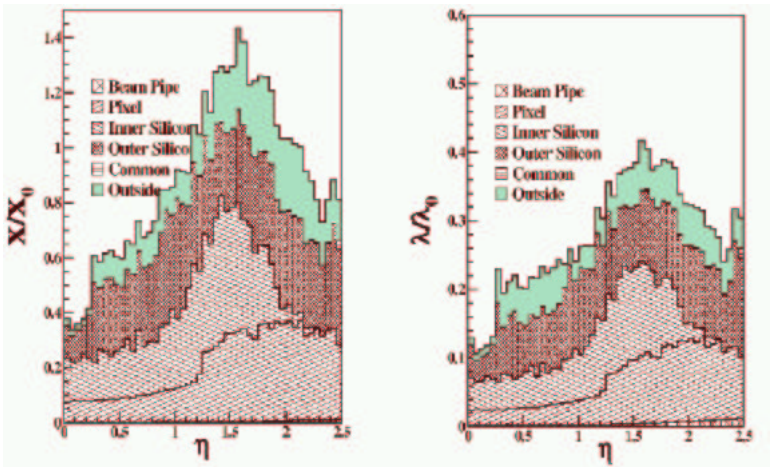

Figure 3.1: *Material budget as a function of η for the different tracker subunits. On the left: material thickness in units of radiation length versus η. On the right: material thickness in units of interaction length versus η.*

3.2 Monte Carlo Generators

Until the LHC start in 2007, no data will be taken by CMS. Nevertheless, physicists are at work to prepare their physics reconstruction and data analysis tools using simulated data.

A simulation chain starts with the generation of physics events with an event generator, such as PYTHIA [47], Herwig [49], IsaJet/IsaSUSY [50], TAUOLA [51], TopRex [52], CompHEP [53], AlpGEN [54] or MadGraph [55]. These events are preselected according to loose Level-1 cuts to reduce the amount of unnecessary computations needed in the subsequent steps.

The several physics generators available in the CMS software environment are collected in the CMKIN (CMS KINematics interface with physics generators) [56] package. The simulated events by the generators are stored as HEPEVT ntuples.

3.2.1 The PYTHIA Event Generator

The PYTHIA [47] Monte Carlo event generator is frequently used in high-energy physics simulations. It is able to produce a complete set of final states for a wide range of processes. In particular it is used for the simulation of hard interactions

in $e^+ - e^-$, $p - p$ and $e - p$ colliders. PYTHIA includes a wide selection of fundamental electroweak and strong Standard Model processes. Additionally, it generates "minimum-bias" events and many non-Standard Model processes. For most of the reactions PYTHIA uses a combination of analytical results and various models instead of exact calculations.

Most of the samples used in this study were generated with PYTHIA version 6.158. PYTHIA's output was stored in the standard HEPEVET structure in HBOOK files and subsequently processed with the CMSJET fast simulation package (see Section 3.4.1).

3.3 Event Simulation

Signal and background events were generated using the PYTHIA [47] Monte Carlo generator (see Section 3.2.1).

In order to correctly take into statistical account each process, a weight for each data sample was set. The weight assigned to each generated event was calculated as:

$$W = \frac{\sigma L}{N_{Gen\,events}}, \tag{3.1}$$

where σ is the cross section of the process, $N_{Gen\,events}$ is the number of generated events for that process and L is the integrated luminosity.

3.3.1 Signal Samples

Among the several sets of parton distribution functions available in PYTHIA, we chose for all our samples GRV 94L [57]. It is a simple leading order fit to experimental data and it is the default in the PYTHIA version that we used. To simulate multiple interactions, a model that assumes double Gaussian spatial distributions of hadronic matter inside the proton was used. Within this model the impact parameter between the interacting partons is variable.

The signal samples were generated using processes $VV \to ZZ$ and $W^{\pm}Z \to W^{\pm}Z$, where all the vector bosons are longitudinally polarized. PYTHIA does not generate scattering processes of transversally polarized vector bosons. In

Table 3.1: *Cross section, number of generated and selected events for different Higgs masses. The total cross section value are referred to generated events and not to the events selected according to the required kinematics and decay modes.*

Signal samples					
Higgs mass (GeV)	**Cross section (fb)**		**Generated events**		**Selected events**
	ZZ	*ZW*	*ZZ*	*ZW*	
500	9.132	0.667	91 596	92 902	90 000
1000	3.049	1.039	91 845	92 625	90 000
2000	1.778	1.402	92 317	92 601	90 000
10000	1.677	1.465	92 362	92 483	90 000

the calculation of the two selected processes, PYTHIA uses the Effective Vector-Boson Approximation (EVBA) [58, 59] (see the Appendix); this method is equivalent to the Effective Photon Approximation (EPA) used in QED (also called Weizsäcker-Williams approximation). Using this approximation the fermion-fermion cross section is written as a product of a probability distribution and the cross section for on-shell vector boson scattering. The probability distribution describes the emission of vector bosons from fermions.

Among all possible final states the semi-leptonic one was chosen: only the events with one Z (W) decaying into a quark and anti-quark pair and the other Z decaying into a muon and an antimuon were selected. Given the geometric acceptance of the CMS detector (see Section 2.2.5), it was required that the generated muons satisfy the cuts $|\eta| < 2.5$ and $P_T^{\mu} > 3.0\,\text{GeV}$.

In order to explore the full spectrum of heavy Higgs masses, different datasets (for both ZZ and ZW signatures) were generated using $m_H = 500\,\text{GeV}$, $m_H = 1000\,\text{GeV}$, $m_H = 2000\,\text{GeV}$ and $m_H = 10000\,\text{GeV}$. The cross section, the number of generated events and the number of selected events for each of these datasets are shown in Table 3.1.

3.3.2 Background Samples

In order to assess the possibility of discriminating our signal from the background, processes with a final state similar to that of the signal were generated.

Not all possible backgrounds were considered at this stage of the study: only a selection of the most important was generated, namely the $t\bar{t} \to W^+W^-b\bar{b}$ process, the production of Z + *jet*, as well as the ZW associated production and the production of ZZ pairs. The first includes all processes with a production of a top anti-top pair; from the top decay a W and a b-quark are produced. The final state is therefore a six fermion final state similar to the one of VV-fusion processes. The Z + *jet* background, in case of leptonic Z decay, has a dangerous final state as well. Even if the topology of processes with a single Z in the final state is very different from that of the signal, the huge cross section makes the discrimination of this background difficult. The production of a pair of Z bosons with semileptonic Z decays may fake the signal signature (as well as the ZW background, where the W decays hadronically and the Z decays leptonically) and its discrimination mainly relies on the requirement of forward jets originating from the quarks which radiated the vector bosons (see Section 4.1).

It is worth noticing that a very important source of background is missing in the current study: the scattering of transversally polarized vector bosons, which has the same topology as the signal. Unfortunately, no Monte Carlo generator was available to simulate this process. However, the cross section for this reaction can be calculated exactly within the Standard Model, and it is therefore possible to get a good estimation the effects of this background[1].

Table 3.2 shows the cross section and the number of events of all the background samples. In the following sections more details about these samples are given. For the generation of these data set the Higgs mass has been set to 150 GeV.

3.3.2.1 $t\bar{t} \to W^+W^-b\bar{b}$ Background

All processes with a $t\bar{t}$ pair in the final state are a significant background because the branching ratio of the top quark into a W and a b-jet is almost 100%. These kinds of events are therefore characterized by a six fermion final state very similar to that of the signal. These events were generated using the processes

[1] The equivalence theorem (see section 1.2.1) and the equation (1.33) ensure that V_LV_L-fusion dominates for high energy scales.

Table 3.2: *Cross section, number of generated and selected events for background samples.*

Background samples			
Sample	**Cross section (fb)**	**Generated events**	**Selected events**
$t\bar{t}$ *(at least 1* μ*)*	$622.049 \cdot 10^3$	463 789	200 000
$t\bar{t}$ *(2* μ*)*	$619.423 \cdot 10^3$	528 269	49 995
$t\bar{t}$ $(\mu^+\mu^-)$	$620.545 \cdot 10^3$	7 138 185	450 000
Z *+ 1 jet*	$1.373 \cdot 10^7$	1 032 939	624 999
ZZ	653.764	286 624	250 000
ZW	663.385	281 111	250 000

$q_i\overline{q_i} \to t\bar{t}$ and $gg \to t\bar{t}$. Three kinds of samples, in which all possible W decays were allowed, were generated, but different requirement on the number and the charge of the muons were applied:

1. At least one muon in final state;
2. two muons (any kind);
3. one muon and one anti-muon.

The only kinematic requirements for these events was that the (anti-)muons in the final state had $p_T^\mu > 3.0\,\text{GeV}$ and $|\eta| < 2.5$. The same choice of PDFs and multiple interaction model as for the signal samples was made. Moreover, for this sample, a hybrid scheme of fragmentation functions was chosen. Within this scheme light flavours are treated with symmetric Lund fragmentation functions while different functions can be separately chosen for charm and heavier flavours.

3.3.2.2 Z + *jet* Background

The fragmentation scheme chosen is the string fragmentation according to the Lund model. Final-state QCD and QED radiation was activated and the Z boson was forced to decay leptonically. PYTHIA is not the most appropriate Monte Carlo generator to produce this sample, since it can generate only one jet at quite high p_T, while the others are soft because they are produced via

gluon-strahlung. In future studies a different Monte Carlo generator should be used, like CompHEP [53] or MadGraph [55]. This background is insidious due to its high cross section compared to that of the signal (see Tables 3.1 and 3.2).

3.3.2.3 ZZ and ZW Background

An important background for the VV-fusion process is the production of Z pairs and the ZW associated production by fermion-antifermion annihilation ($f_i\overline{f_i} \to ZZ$) and fermion-antifermion scattering ($f_i\overline{f_j} \to ZW^{\pm}$).

The generator uses for this processes a cross section derived from the narrow-width limit, but extended to include Breit-Wigner shapes, with mass-dependent width, for the final state particles. In the narrow-width approximation, the process is separated in the on-shell production of vector bosons and their decay. The most dangerous final state is the semileptonic one. The Z pair was therefore forced to decay into a quark and anti-quark pair and a muon and an antimuon (likewise ZW, where $Z \to \mu^+\mu^-$ and $W^{\pm} \to q_i\overline{q_j}$). The muons were required to be within the detector acceptance ($|\eta| < 2.5$) with $p_T^{\mu} > 3.0\,\mathrm{GeV}$. The choice of the other PYTHIA parameters was made consistently with all other samples: the GRV 94L PDF set was chosen and multiple interactions were switched on.

3.4 Detector Simulation

The purpose of the detector simulation is to transform the simulated physics events into simulated detector measurements. The detector efficiencies, noise levels and measurement uncertainties are simulated in detail. The output of the detector simulation should closely resemble the data that the experiment will produce.

The main simulation tools for the CMS experiment are based on the OSCAR [60]/GEANT4 [61] package for tracking and the ORCA [62] program for reconstruction.

For the simulation of the CMS detector response OSCAR, Object oriented Simulation for CMS Analysis and Reconstruction, is used. OSCAR is based on GEANT4.[2]

[2]Geant4 is a toolkit for the simulation of the passage of particles through matter.

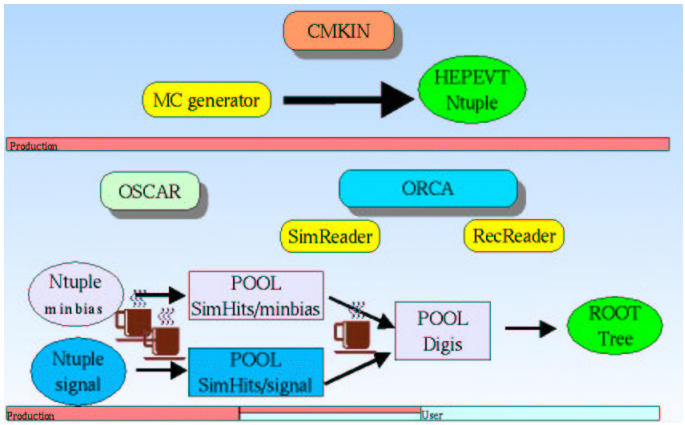

Figure 3.2: *CMS software chain.*
The Pile-up is selected randomly from a sufficiently large database of minimum bias events. After digitization the resulting objects are stored in POOL DB.

OSCAR reads the HEPEVT produced by CMKIN generators and produces the so-called SimHits in the form of POOL[3] database files. It translates the events in the interaction region into hits in the detector. The SimHits contain information like: entry point, detector id, particle type, momentum, etc. In OSCAR the geometry description [63] is handled through DDD [64], Detector Description Database. The detector description is realized in the XML language. Each software package utilizes this description to process the data according to the set-up of the detector. Therefore the OSCAR/GEANT4 package transforms the particles and tracks of the physics events into simulated hits in the detector, such as tracker hits and energy deposited in calorimeter crystals. OSCAR is interfaced to CARF for the persistent storage (see below).

The SimHits produced by OSCAR are subsequently read by ORCA (see Figure 3.2).

The CMS reconstruction framework is called ORCA, Object oriented Reconstruction for CMS Analysis. ORCA, as the name suggests, takes care of the event reconstruction but it also implements the High Level Trigger algorithms that will be run on a CPU farm when CMS is operational. ORCA can be used for final detector optimizations, trigger studies or global detector performance evaluation. To this end it provides a sub-detector reconstruction skeleton into

[3]Pool Of persistent Objects for LHC [70].

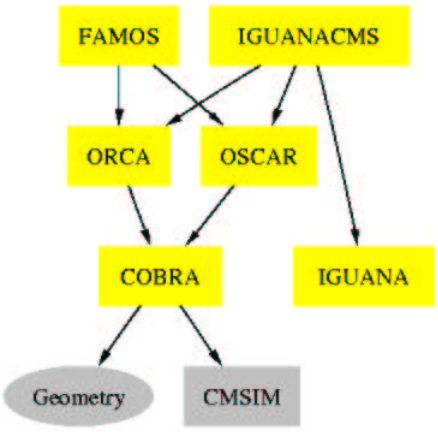

Figure 3.3: *Major CMS software packages and their interrelations. OSCAR, CMSIM (obsolete) and FAMOS are programs used for detector simulation. ORCA is used for software triggering, event reconstruction and data-analysis. COBRA contains common routines for reconstruction, analysis and simulation shared by ORCA and OSCAR. IGUANA [66] is used for visualization.*

which new developers can implement realistic objects and algorithms. Another important task of ORCA is the digitization of detector simulation data from OSCAR. It simulates detector efficiencies, electronics noise and statistical fluctuations, and gives output similar to the one that will be obtained from the real CMS detector. The raw simulated data are then processed by the simulated Level-1 trigger and the high level triggers in ORCA. The requested event data is written on disk in compact form for physics analysis.

For some parts of its functionality, ORCA relies on other software packages. The most important of these is COBRA [65], Coherent Object-oriented Base for Reconstruction, Analysis and simulation. It provides services common to both ORCA and OSCAR. ORCA visualization is handled through IGUANA, Interactive Graphics for User ANAlysis. The interrelations of the software packages are shown in Figure 3.3.

It should be noted that many of the programs mentioned above are in continuous development. Due to the increasing complexity of the programs, the CMS collaboration decided to use object oriented technology and C++ has been chosen as the programming language. This allows the use of many modern C++ standard tools (*e.g.* the C++ standard library). The Software and runtime

environment is managed and distributed using SCRAM [67]. The source code is organized into modules using CVS [68] in order to support a multi-developer environment. All the packages are embedded in the CARF framework.

The Framework The CMS framework is called CARF.[4] To achieve maximum flexibility, CARF implements an implicit invocation architecture (Action on Demand) [69] where modules register themselves at creation time and are invoked when required. In this way only those modules really needed are loaded and executed. CARF pins Database objects (POOL [70]) in memory for the duration of an event. The user does not see if the object is transient or in the Database. All modules see the same persistent data and each module can change its local copy of the data, but persistent data cannot unintentionally be changed.

Even if these powerful tools are widely used in the CMS collaboration, the full detector simulation is not used for the preliminary study presented here. Detailed detector simulation is time consuming and in some cases rough approximations for detector response are sufficient. FAMOS [71], FAst MOnte Carlo Simulation, is being developed, but at the present time stable version is not yet existing. For this reasons the CMSJET fast simulation package was used. However in the future the present study will be repeated using the full detector simulation.

3.4.1 The CMSJET Fast Simulation Package

CMSJET [48] is a package for fast non-GEANT simulation of the CMS detector response, basically designed for jet physics applications. CMSJET 4.801 was used to process the PYTHIA output in HEPEVET Ntuple format. Reconstructed objects were written out in Ntuples together with the particle four-momenta at the parton level.

CMSJET simulates particle tracking by smearing the momentum of the generated tracks and assuming predefined efficiencies for their detection and reconstruction. The calorimeter system (see Fig. 3.4) is represented through

[4] CMS Analysis and Reconstruction Framework.

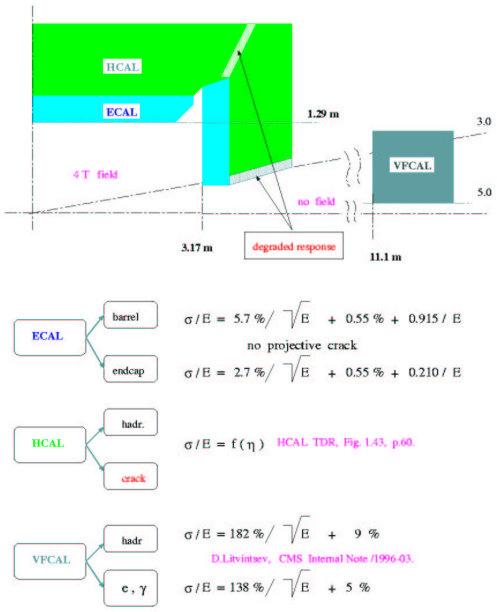

Figure 3.4: *The CMSJET 4.801 calorimetry model.*

a set of cylinders and conical volumes with the granularity discussed in Section 2.2.3 for the ECAL and Section 2.2.4 for the HCAL. The magnetic field used for particle tracking is uniform up to the calorimeter surface and negligible outside the HCAL endcaps. Smearing effects for the jet energy and momentum are simulated according to the calorimeter resolution. A simplified noise model is used for ECAL and HCAL.

Jet finding is performed using a cone algorithm. The size of the cone is set to $\Delta R = \sqrt{\Delta\phi^2 + \Delta\eta^2} = 0.5$ on the whole pseudorapidity range covered by calorimeters ($|\eta| < 5$, see Section 2.2.4). In the CMSJET version used for this analysis, no jet calibration is applied. For this reason the reconstructed jet energy has a systematic "shift" towards low values if compared to the energy of the parent partons.

Muons are identified within the pseudorapidity range $|\eta| < 2.4$. The muon reconstruction simulation is very simplified. It was however considered adequate for the present exploratory study.

CMSJET contains some routines for pile up treatment, which was considered in this study.

All the signal and background samples used for this study were generated with PYTHIA and processed through CMSJET at the CMS-farm in Torino.

3.4.2 Full and Fast Simulation

As seen in Section 3.4.1 the fast simulation is based on the parametrization[5] of both the effect of the interactions of particles with matter (*e.g.* the multiple scattering and the Bethe-Block energy loss) and the detector response. Conversely in the full simulation the material and the detector response are simulated with Monte Carlo Techniques and the particles are followed step by step. Given that, it is inevitable that there are some differences between the two CMS experiment simulations. In this section it will be shown that for the present study the discrepancies are not such as to invalidate the analysis.

About 950 events with $m_H = 2000$ GeV, with *pile-up*, were processed by the full simulation on digital unix machines. In the following some plots are shown.

Figure 3.5 compares the distribution of number of jets for the OSCAR/ORCA chain (with Δr cone of 0.5) and the CMSJET one. The differences are due in part to the low statistics available for the full simulation and to differences in jet reconstruction algorithms (see figure 3.5).

For what concerns the muon number distribution, no significant differences are present (Figure 3.6) between the two simulations. In Figure 3.7 the p_T distribution of the Z that decay leptonically is shown. The statistics for the full simulation is low, but the two distribution are consistent.

Obviously CMSJET is an approximation of a detector simulation, therefore cuts and reconstruction parameters used in this work have to tuned on the full simulation, in a near future. The use of the full simulation will provide new tools: as an example a better control of the detector will allow to study the systematic errors and reject backgrounds like the $t\bar{t}$ using the information on the secondary vertex.

[5]The parameters are extracted from the full simulation. When LHC will be operational, the parameters can be taken from real detector. A test on the full simulation will be done comparing the parameters extracted from it with the ones taken from real detector.

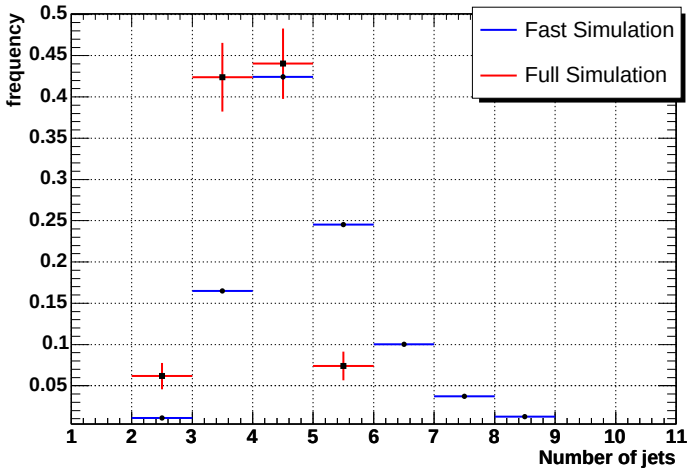

Figure 3.5: *Comparison of number of jets per event between fast (blue) and full (red) simulation.*

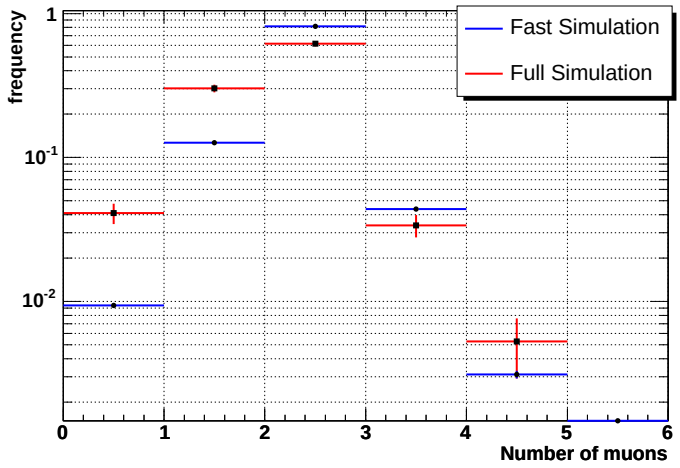

Figure 3.6: *Comparison of number of muons per event between fast (blue) and full (red) simulation.*

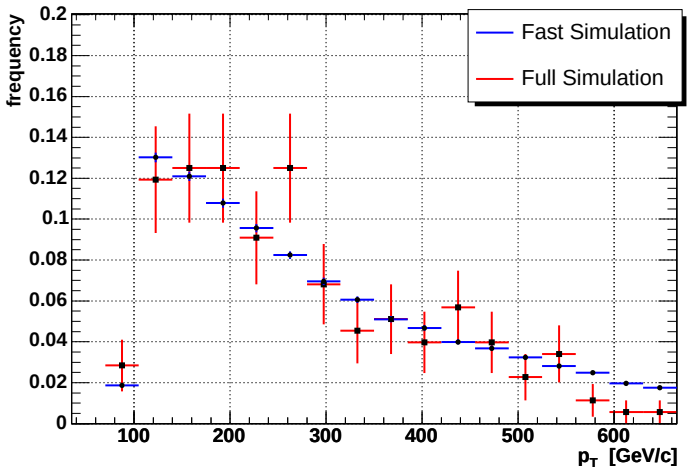

Figure 3.7: *Comparison of p_T distributions of the Z which decays leptonically between fast (blue) and full (red) simulation.*

Chapter 4

Data Analysis

This Chapter summarizes the key results of the present work, which focuses on a model-independent study of the reactions [1]:

$$pp \to j_F j_B Z_L Z_L + X \to j_F j_B \mu^+ \mu^- jj + X \tag{4.1}$$

$$pp \to j_F j_B Z_L W_L + X \to j_F j_B \mu^+ \mu^- jj + X \,. \tag{4.2}$$

As seen in Section 1.2.1, vector boson fusion is a very promising family of processes to study the electroweak symmetry breaking. The aim of this Chapter is to demonstrate that VV-fusion events can be reconstructed in the CMS detector and that the cross section of the process, as a function of the centre-of-mass energy ($\sigma_{VV}(M_{inv}^{fusion})$), is a good observable of EWSB.

Other important parameters are the resolution on $\sigma_{VV}(M_{inv}^{fusion})$, the signal reconstruction efficiency and the integrated luminosity needed to reach an appropriate[2] signal over background ratio ($S/\sqrt{B}$).

Moreover, it is important to determine if the two processes (4.1) and (4.2) are experimentally distinguishable.

In the first part of this Chapter, the main features of signal and background are described. Understanding the signal and the background kinematics as well

[1] The subscripts "F" and "B" mean *forward* and *backward*, because the jets originated from the quarks that have emitted the V's are concentrated in the high pseudorapidity region.

[2] One standard deviation from the background corresponds at 95% of confidence level. Three and five deviations correspond respectively to an evidence for and a discovery of new physics.

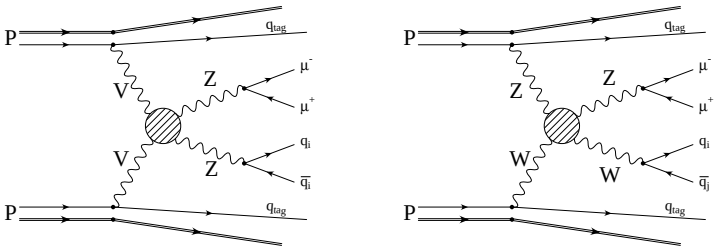

Figure 4.1: *The signal topology.*

as the detector response is crucial in order to be able to reconstruct the signal events and reject the background. Then cuts to reduce the background and the results are discussed.

4.1 The Signal

In $p-p$ collisions, the signature of the VV-fusion signal is based on the fact that the final state has six fermions (see Figure 4.1): in a heuristic way it is possible to see the vector boson fusion process as follows. Two protons approach and a vector boson is emitted from a quark (or an anti-quark) of each proton. The two V's interact (the fusion process is described at tree-level by diagrams in Figs. 1.4 and 1.5) yielding two V's in the final state. The final state considered is the one where the Z decays into two muons and the other V into two quarks. In addition, there are two more jets from the quarks which have radiated the V's, the so called *tag jets*. They are the signature that the two V's in the final state have been produced by a vector boson fusion process, and are a powerful tool to reject most of the background. Usually the remnants of the interacting protons escape undetected into the beam pipe.

The central jets and the two leptons are used to reconstruct the VV system invariant mass while the forward jets, originating from the hadronisation of the quarks that radiated the vector bosons, are used to tag the events. The calorimetry system of the CMS detector has a large pseudorapidity coverage, with the HF calorimeter allowing jet reconstruction up to $\eta = \pm 5$.

The two signal processes taken in account are:

- $V_L V_L \to Z_L Z_L \to \mu^+\mu^- jj$

- $W_L Z_L \to W_L Z_L \to jj\mu^+\mu^-$,

where one Z always decays leptonically and the other vector boson hadronically.

The two signals have common features and experimentally the only possibility to distinguish them is by reconstructing the invariant mass of the hadronically decaying vector bosons. One of the goals of this work is to understand if it is possible to single them out.

In order to explore the sensitivity of the analysis method to the whole heavy Higgs mass spectrum, we generated Monte Carlo data sets with different Higgs masses: $m_H = 500$ GeV, $m_H = 1000$ GeV, $m_H = 2000$ GeV and $m_H = 10000$ GeV. In the first two samples, the VV invariant mass spectrum exhibits a resonance at the Higgs mass. The other two samples simulate the no-Higgs scenario.

The kinematics One of the most important kinematic variables is the pseudorapidity η. The study of its distribution allows to single out the tag jets with respect to the jets from the vector boson decay and to reject a large fraction of the background.

Figure 4.2 shows the η distributions for the two families of jets: tag jets are mainly in *forward-backward* regions (*i.e.* the end-caps), whereas jets[3] from V's are in the central region (*i.e.* the barrel).

Further differences between the two kinds of jets lie in their transverse momentum and energy distributions (see fig. 4.3). Applying requests on η, p_T and E, it is therefore possible to distinguish the vector bosons jets from the tag jets.

4.2 The Background

In order to estimate the signal over background ratio, the most important backgrounds are taken into account. In this section a detailed description of the kinematics of backgrounds is given.

The most difficult background to the fusion of longitudinally polarized W and Z boson, is given by $V_L V_T$ and $V_T V_T$ scattering. However, at this stage of the study, this background is not considered because no appropriate Monte Carlo

[3] Also the muons from the Z are in the barrel.

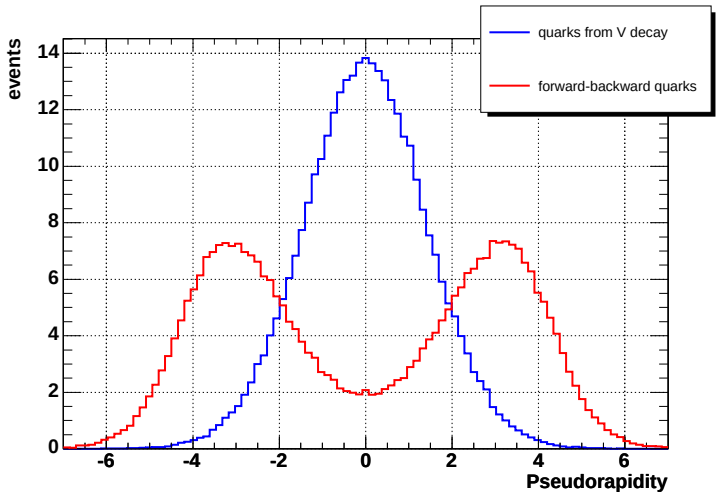

Figure 4.2: *Pseudorapidity distributions of quarks from vector boson decay and forward-backward quarks (signal parton level).*

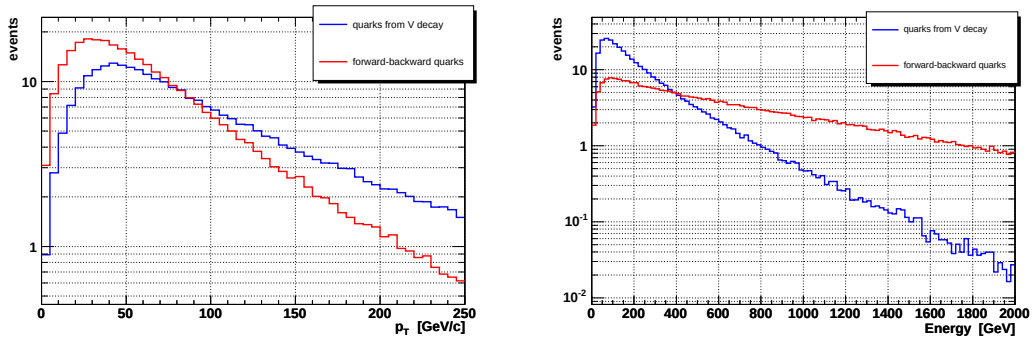

Figure 4.3: *Transverse momentum and energy distributions of quarks from vector boson decay and of forward-backward quarks (signal parton level).*

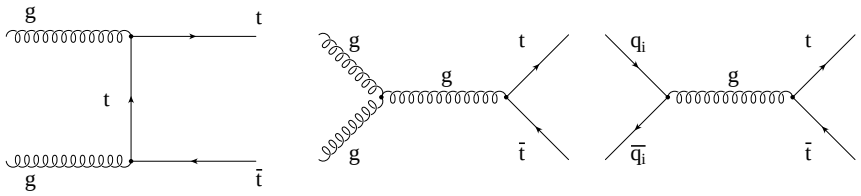

Figure 4.4: *Tree-level Feynman diagrams for the $t\bar{t}$ background.*

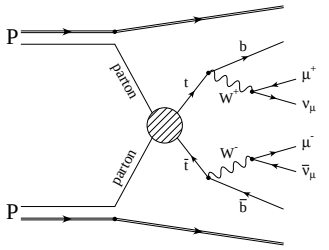

Figure 4.5: *$t\bar{t}$ background topology. The above decays combination is one of the possibles to obtain two muons in the final state.*

generator was available. For the same reason the bremsstrahlung radiation of vector bosons is not included.

4.2.1 $t\bar{t}$ Background

This background is given by the reaction

$$pp \to t\bar{t} + X \to b\bar{b}W^+W^- + X \to j_b j_b \mu^+ \mu^- jj + X\,. \tag{4.3}$$

Two partons (quarks or gluons) from the two incoming protons interact to give a top anti-top pair (see Figure 4.4). Since the top decays into a W boson and a b-quark with a branching ratio of almost 100 %, the $t\bar{t}$ process also gives a six fermion final state (fig. 4.5). Since both the W's and the B hadrons can decay leptonically, the final state has a very similar topology to that of the signal.

The kinematics In Figure 4.6 the pseudorapidity distribution for $t\bar{t}$ is shown. The pseudorapidity of the b-quarks peaks in the barrel region, whereas tag quarks from the signal are in end-cap regions. As a consequence, the rejection

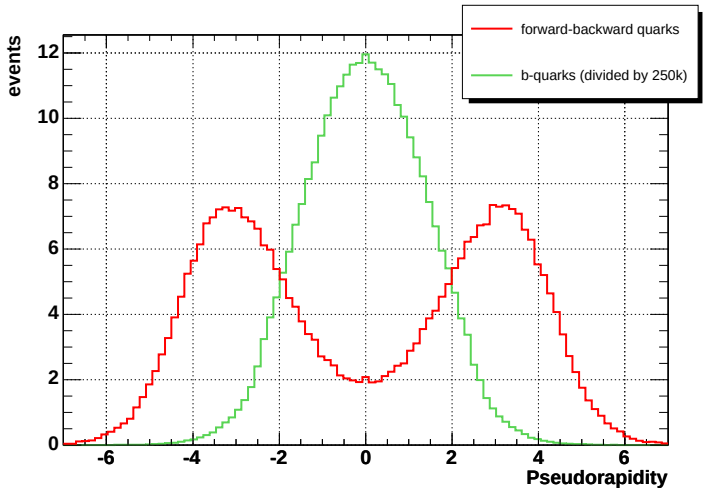

Figure 4.6: *Pseudorapidity distribution of* b*-quarks from* $t\bar{t}$ *background compared with that for the signal forward-backward quarks (parton level).*

of this background can be largely achieved by requiring two jets with high η and $\Delta\eta$. Moreover, there are differences between the $t\bar{t}$ and signal processes in the p_T and energy distributions. Figures 4.7 and 4.8 show that quarks for the signal have a larger energy and transverse momentum than quarks from the $t\bar{t}$ process.

4.2.2 *ZZ* and *WZ* Associated Production

This background is characterized by the presence of a Z pair or a WZ boson pair, which then decay in a semileptonic final state. A schematic description of the two processes

$$pp \to ZZ + X \to \mu^+\mu^- jj + X \tag{4.4}$$

$$pp \to ZW + X \to \mu^+\mu^- jj + X \tag{4.5}$$

is given in Figure 4.9. The main diagrams of these processes are shown in Figure 4.10. The absence of quarks in the forward-backward region helps the analysis algorithm to single out this kind of events as background.

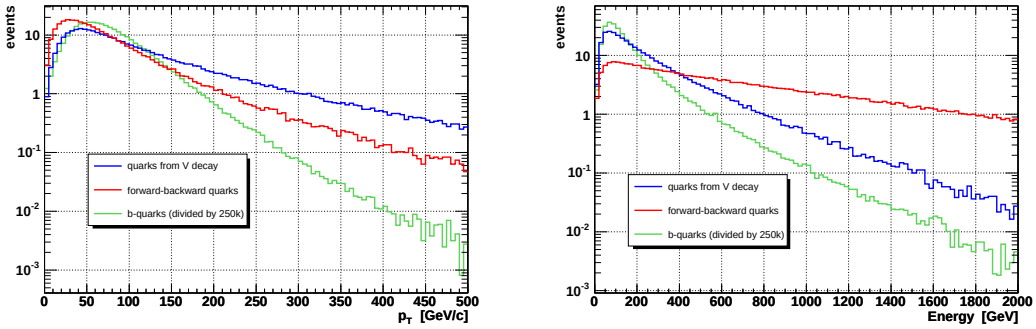

Figure 4.7: *Transverse momentum and energy distributions of* b*-quarks from* $t\bar{t}$ *background compared with those for the signal quarks (parton level).*

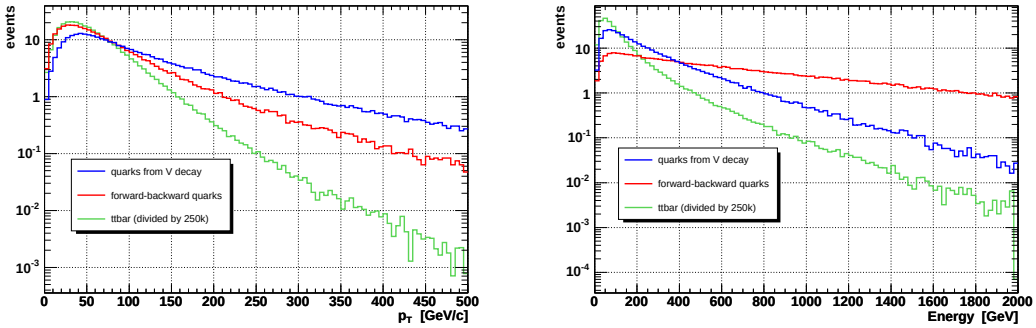

Figure 4.8: *Transverse momentum and energy distributions of quarks from the vector boson for the* $t\bar{t}$ *background compared with those for the signal quarks (parton level).*

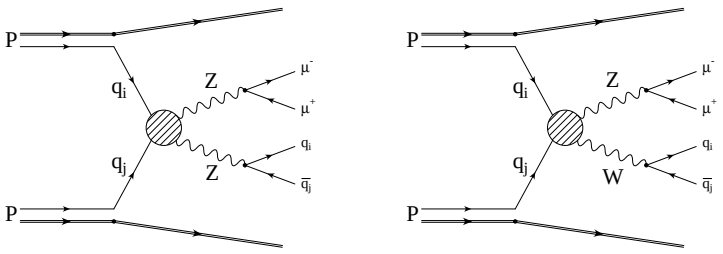

Figure 4.9: ZZ *and* ZW *background topology. One vector boson is forced to decay in two muons and the other in a quark pair.*

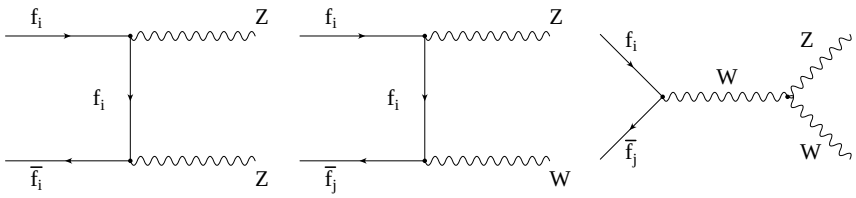

Figure 4.10: *Tree-level Feynman diagrams for* ZZ *and* ZW *backgrounds.*

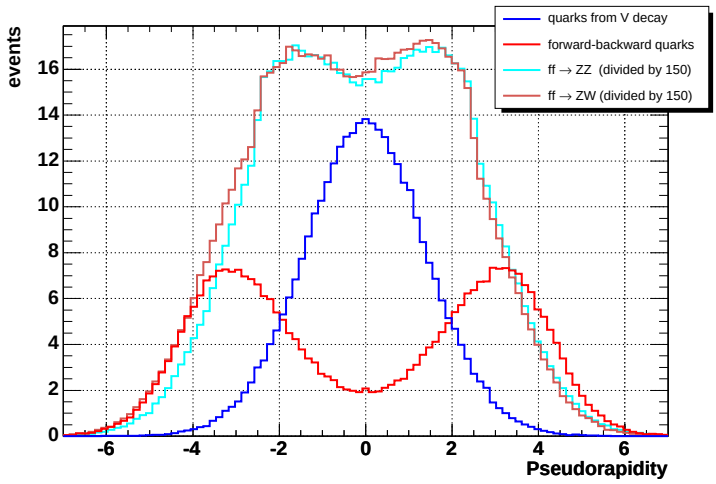

Figure 4.11: *Pseudorapidity distribution of quarks from vector boson for* ZZ *and* WZ *backgrounds compared with that for the signal quarks (parton level).*

The kinematics The pseudorapidity of the quarks from the hadronically decaying vector boson is distributed mostly at low η (fig. 4.11), as for the signal. However, since the p_T and the energy distributions (Fig. 4.12) of the quarks and the muons are softer than those from the signal, a set of cuts on these kinematic variables allows to suppress this background.

4.2.3 Z + jet Background

This background (Figure 4.13) is described by the tree-level diagrams in Figure 4.14. The Z boson is produced together with a quark or a gluon, which then hadronizes in one hard jet. Other jets are produced via parton splitting, and are mainly soft. Similarly to the ZZ and WZ associated production backgrounds,

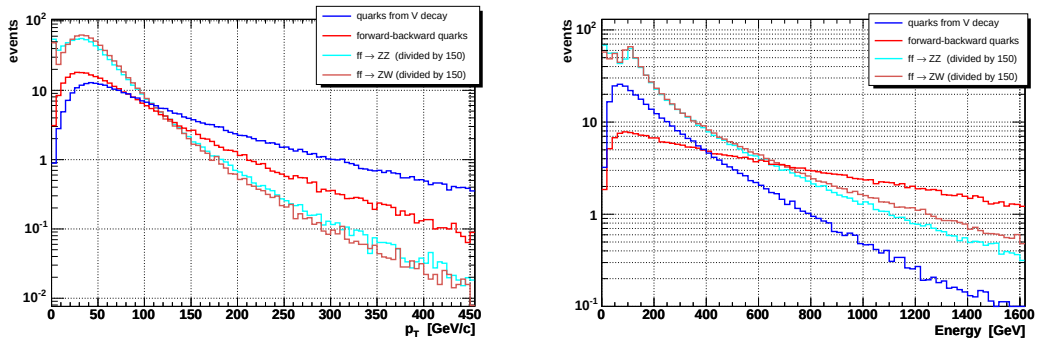

Figure 4.12: *Transverse momentum and energy distributions of quarks from vector boson for* ZZ *and* WZ *backgrounds compared with those for the signal quarks (parton level).*

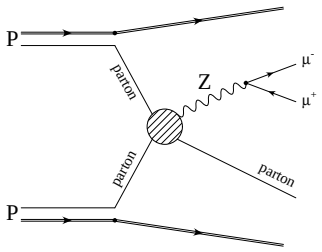

Figure 4.13: *Z + jet background topology.*

the absence of quarks in the forward-backward region allows to reject most of the *Z + jet* events.

The kinematics The quark from this process (Fig. 4.13) has, on average, low pseudorapidity, similarly to the quarks from the vector boson decay in signal events. However comparing the two spectra it is possible to see that the *Z + jet* distribution is less steep than that of the signal. In Figure 4.16 the quark transverse momentum and energy distributions are shown: since the p_T and the energy are softer than that from the signal, appropriate requirements on these variables suppress this background.

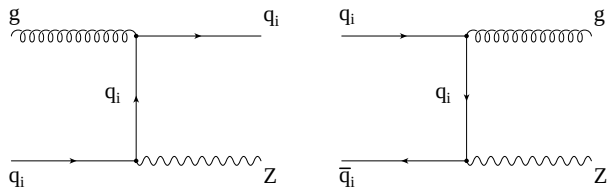

Figure 4.14: *Some of the Feynman diagrams for the* Z + jet *background.*

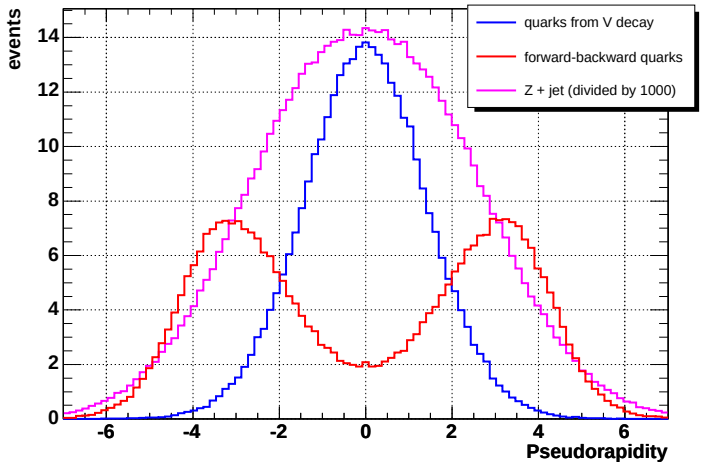

Figure 4.15: *Pseudorapidity distribution of quarks for* Z + *quark background compared with that for the signal quarks (parton level).*

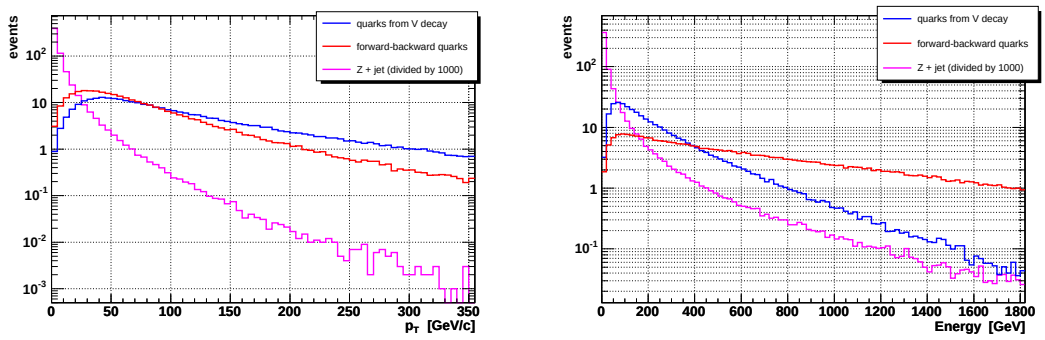

Figure 4.16: *Transverse momentum and energy distributions of quarks for* Z + *quark background compared with those for the signal quarks (parton level).*

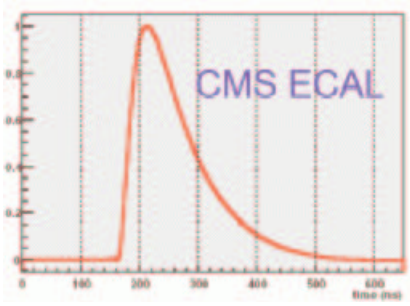

Figure 4.17: *Time response of the CMS electromagnetic calorimeter.*

4.3 Signal Reconstruction and Background Rejection

Two are the main goals of the present analysis: the determination of the VV-fusion cross section as a function of the centre-of-mass energy and the rejection of the background. Five main steps can be identified in the analysis procedure:

1. Pile-up rejection.
2. Minimal requirements on the topology of the events: at least one μ^+ and one μ^-, more than three jets and the tag jets.
3. Cuts on the muons and jet kinematic variables.
4. Vector boson reconstruction.
5. Cuts on vector boson kinematic variables.

4.3.1 Pile-up Rejection

Due to the high $p-p$ cross section and finite response times of the detectors (*e.g.* the ECAL, as shown in Fig. 4.17), a lot of backgrounds come from secondary proton-proton collisions. There are two kinds of pile-up events: "in-time" and "out-of-time". In-time pile-up comes from $p-p$ collisions that occurred in the same bunch crossing as the event(s) selected by the trigger. Out-of-time pile-up is due to $p-p$ collisions in previous and following bunch crossings (Figure 4.18).

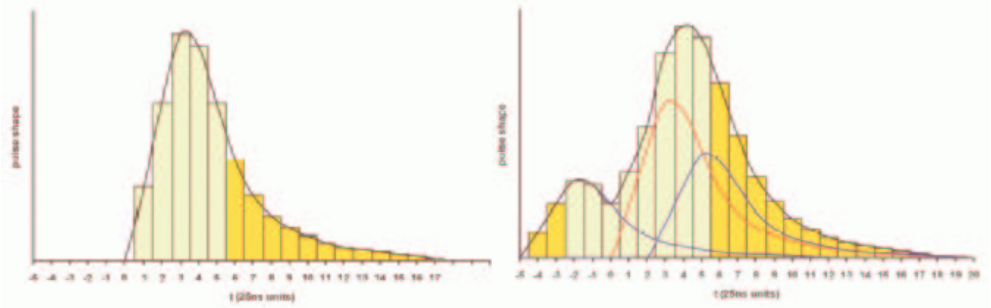

Figure 4.18: *Left: "in-time" pile-up: particles from the same bunch crossing but from a different $p-p$ interaction. Right: "Out-of-time" and "in-time" pile-up effect: left-over signals from interactions in previous crossings are summed over the current bunch signal.*

As shown in Figures 4.19 and 4.20, pile-up jets populate the high pseudorapidity region and have low p_T compared to the ones from hard processes (see the same Figures). Therefore a cut of 25 GeV on the transverse momentum of jets is applied. Since jets from the background processes discussed in the previous Sections have a p_T distribution softer than the signal one, this cut allows to reject also some of that background. In Table 4.1 the effect of this cut is summarized.

4.3.2 Requirements on Event Topology

In order to reconstruct the signal events and reject the background with a different topology than the signal, three main constraints are needed:

- at least one μ^+ and one μ^-;
- the number of jets greater than three;
- the presence of jets in the forward and backward regions.

$\mu^+\mu^-$ request Since the CMS detector will have a good momentum resolution and a perfect magnetic field control, requests on particle charges can be made. The request of at least one μ^+ and one μ^- in the final state is a strong constraint. The effects of this request are listed in Table 4.2.

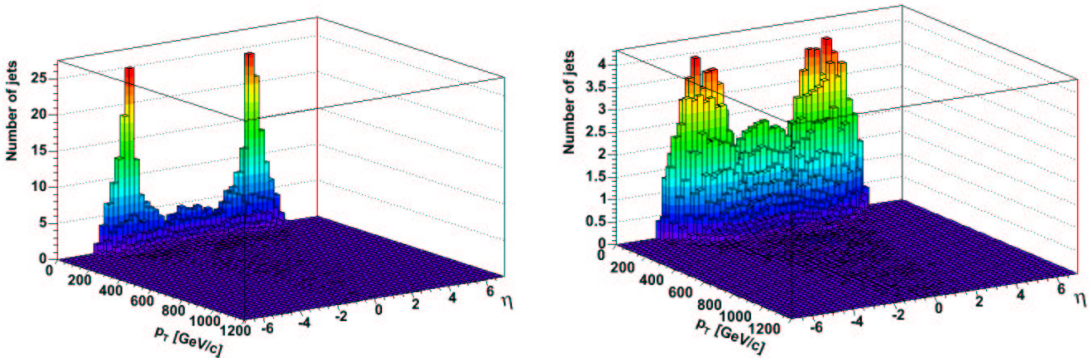

Figure 4.19: *On the left: distribution of jet energy and pseudorapidity for a data set ($m_H = 2000$ GeV) processed with pile-up. On the right: the same data set processed without pile-up. Pile-up jets are mostly at low transverse momentum.*

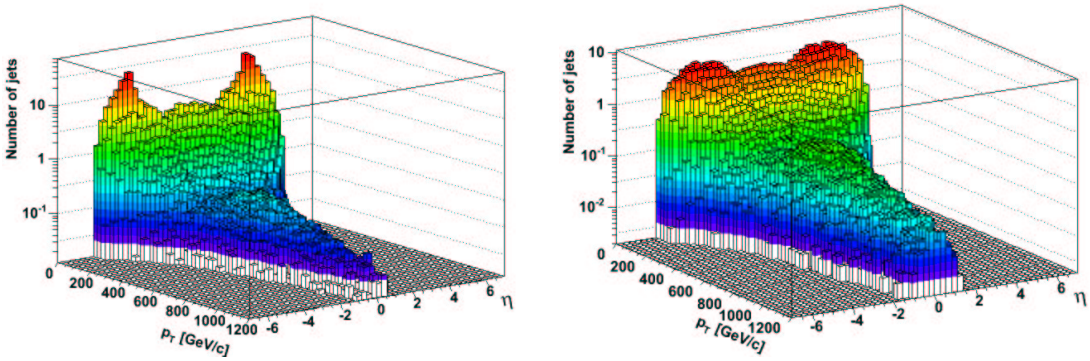

Figure 4.20: *The same plots as in the previous figure, but in a logarithmic scale.On the left: distribution of jet energy and pseudorapidity for a data set processed with pile-up. On the right: data set processed without pile-up. Pile-up jets are mostly at low transverse momentum, whereas jets from hard processes populate the whole p_T range, up to 2000 GeV.*

Table 4.1: *Efficiency of the pile-up removal cut.*

Samples	Efficiency
Signal in ZZ ($m_H = 500$ GeV)	99.99 %
Signal in ZW ($m_H = 500$ GeV)	99.99 %
Signal in ZZ ($m_H = 1000$ GeV)	99.98 %
Signal in ZW ($m_H = 1000$ GeV)	$\sim$ 100 %
Signal in ZZ ($m_H = 2000$ GeV)	99.97 %
Signal in ZW ($m_H = 2000$ GeV)	99.99 %
Signal in ZZ ($m_H = 10000$ GeV)	99.97 %
Signal in ZW ($m_H = 10000$ GeV)	99.99 %
$qq \to ZZ$ background	95.95 %
$qq \to ZW$ background	96.48 %
Z + jet background	45.67 %
$t\bar{t}$ at least 1 muon	99.91 %
$t\bar{t}$ 2 muons any charge	99.81 %
$t\bar{t}$ 1 $\mu^+$and 1 μ^-	99.81 %

Number of jets The signal topology is characterized by four jets in the final state. The request to have at least four jets with p_T greater than 25 GeV is the minimum one in order to correctly reconstruct the signal. In Figure 4.21 the distributions of the number of jets for the signals and the backgrounds are shown. The effects of this cut are shown in Table 4.2.

Tag jets This is one of the most powerful cuts. As shown in Table 4.2, it allows to reject most of the background. The signal efficiency is also reduced by this request. However application of the cut results in a net increase of the signal over background ratio.

The tag jets reconstruction is performed through a set of requests on single jets and on the candidate pair of tag-jets. First of all only jets with both $|\eta| \geq 1.5$ and $E \geq 100$ GeV (see Figures 4.2 and 4.3) are taken in account; then all the possible pairs of jets are taken in turn as tag jet candidates. Candidates undergo cuts on the energy, on the transverse momentum and on the pseudorapidity difference between the two tag-jets candidates:

- $E_1 + E_2 > 500$ GeV,

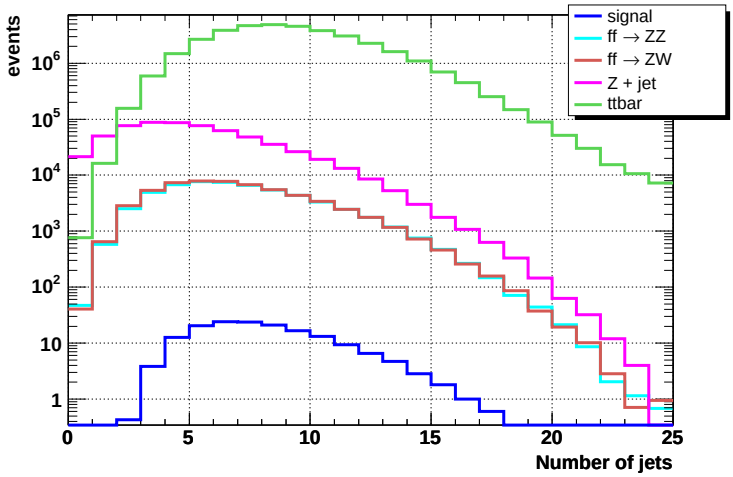

Figure 4.21: *Number of jets per event for the signal ($VV \rightarrow ZZ$ with $m_H = 10000$ GeV) and for the background samples.*

- $p_T^1 + p_T^2 > 35$ GeV,
- $\Delta\eta > 3.5$.

This last request has the non negligible effect to reject almost all the $t\bar{t}$ background, since, even if it is a six fermion final state, the $\Delta\eta$ between the two jets has very low values (see Figure 4.22).

Among the pairs that have passed the selection criteria, the one with the best combination of E, p_T and $\Delta\eta$ is taken as tag-jet pair.

The signal and background efficiencies after these three requests are shown in Table 4.2.

4.3.3 Kinematic Cuts

Figure 4.23 shows the p_T distribution of all the reconstructed muons. The muons from the background are mainly at low transverse momentum. Thus the request of having one μ^+ and one μ^- both with p_T greater than 20 GeV rejects a good fraction of the background (see Table 4.3).

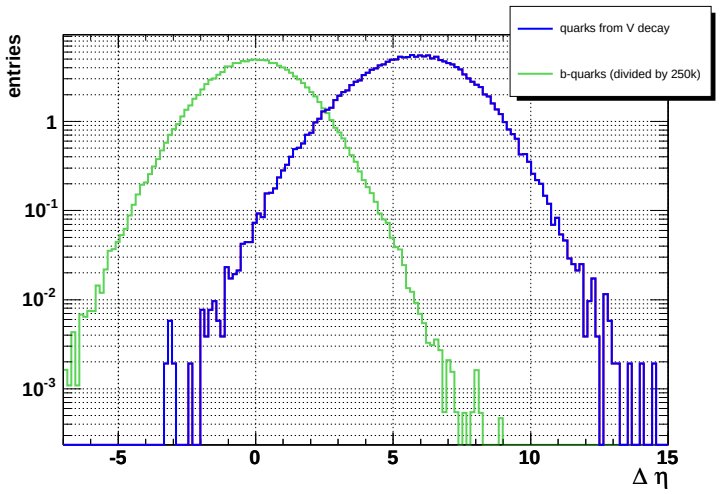

Figure 4.22: *$\Delta\eta$ among the two tag jets compared with signal tag quarks (parton level distributions).*

Table 4.2: *Efficiencies of topological cuts.*

Samples	μ charge	Num. of jets	Jets tag	Combined
Signal				
ZZ $(m_H = 0.5\ TeV)$	88.02 %	93.55 %	49.08 %	43.83 %
ZW $(m_H = 0.5\ TeV)$	82.56 %	92.20 %	47.89 %	40.38 %
ZZ $(m_H = 1\ TeV)$	88.76 %	91.21 %	52.80 %	47.53 %
ZW $(m_H = 1\ TeV)$	83.97 %	92.18 %	50.13 %	42.93 %
ZZ $(m_H = 2\ TeV)$	86.15 %	91.29 %	50.54 %	44.31 %
ZW $(m_H = 2\ TeV)$	85.48 %	92.18 %	52.40 %	45.58 %
ZZ $(m_H = 10\ TeV)$	85.59 %	91.11 %	49.72 %	43.42 %
ZW $(m_H = 10\ TeV)$	85.83 %	92.19 %	52.96 %	46.60 %
Background				
$qq \rightarrow ZZ$	59.26 %	45.63 %	5.87 %	3.27 %
$qq \rightarrow ZW$	61.58 %	43.32 %	6.66 %	4.20 %
$Z + jet$	26.84 %	16.89 %	4.30 %	0.83 %
$t\bar{t}$ *at least 1 muon*	6.60 %	91.35 %	11.23 %	0.69 %
$t\bar{t}$ *2 μ's any charge*	29.39 %	88.46 %	12.04 %	3.06 %
$t\bar{t}$ *1 μ^+ and 1 μ^-*	45.17 %	87.20 %	10.75%	4.83 %

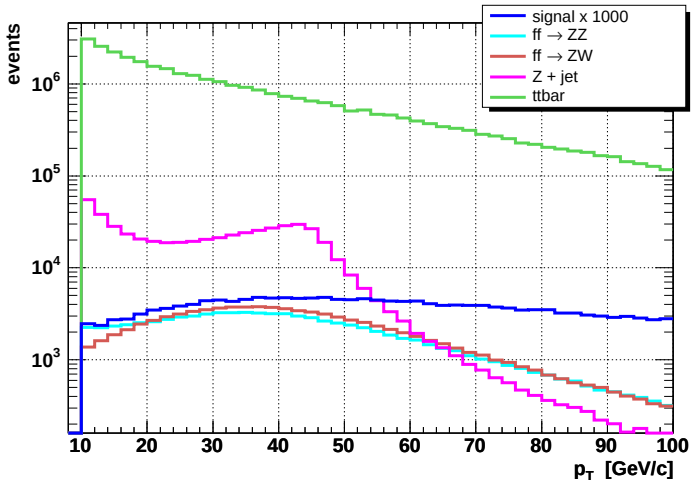

Figure 4.23: *Transverse momentum distributions of the muons in the event. The signal is multiplied by* 10^3.

The distribution of the $p-p$ invariant mass is shown in Figure 4.24 for the background and the signal.

Imposing a cut at 1 TeV, the efficiencies shown in Table 4.3 are obtained.

4.3.4 Vector Bosons Reconstruction

A correct reconstruction of the vector bosons is a key aspect of the analysis not only for the signal reconstruction and the background rejection, but also to answer the question: are $VV \to ZZ$ *and* $ZW \to ZW$ *distinguishable?*

4.3.4.1 $Z \to \mu^+\mu^-$ Reconstruction

Since about 4.5% of the events have three or more muons (see Figure 4.25) a selection to identify the correct $\mu^+\mu^-$ pair is necessary.

The reconstruction algorithm combines all the possible muon anti-muon pairs. A first selection of the pairs is done exploiting the collinearity in p_Z, as shown in Figure 4.26 for the generated samples. Since there are few events in which the two muons are not properly collinear ($p_Z^{\mu^+} \cdot p_Z^{\mu^-} < 0$), a less stringent request on the p_Z collinearity was applied. The pairs which satisfy one of these equations:

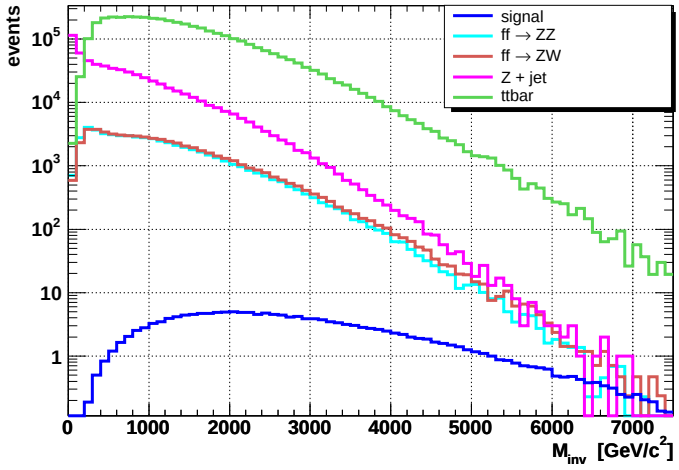

Figure 4.24: *Total invariant mass of the $p-p$ process (the jets with p_T lesser than 25 GeV are not taken into account). Cutting at 1 TeV, the background is suppressed, preserving high signal over background ratio. (The signal is $VV \to ZZ$ with $m_H = 10000$ GeV)*

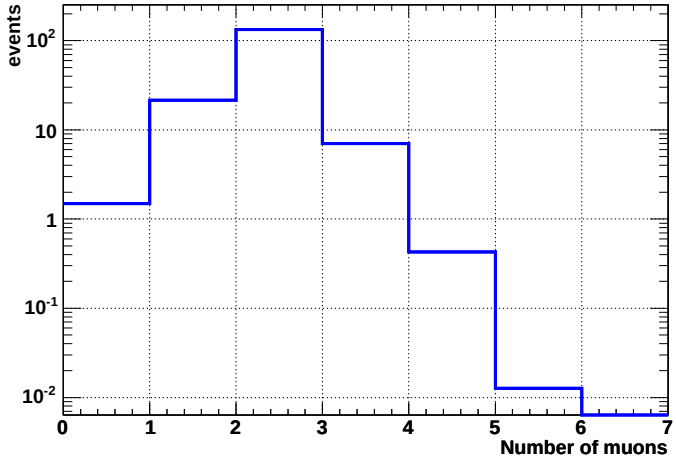

Figure 4.25: *Number of muons per event for the ZZ signal ($m_H = 10000$ GeV).*

Table 4.3: *Efficiencies after cuts on the total invariant mass (1 TeV) of the process and on the muons transverse momentum (20 GeV). It is remarkable that for high Higgs masses the efficiency for the two channels $VV \to ZZ$ and $ZW \to ZW$ tend to the same value.*

Samples	p_T of muons	Total invariant mass	Combined
Signal			
ZZ ($m_H = 0.5$ TeV)	82.75 %	93.22 %	77.81 %
ZW ($m_H = 0.5$ TeV)	75.55 %	90.68 %	69.55 %
ZZ ($m_H = 1$ TeV)	84.73 %	95.12 %	81.57 %
ZW ($m_H = 1$ TeV)	77.84 %	92.36 %	72.85 %
ZZ ($m_H = 2$ TeV)	81.02 %	92.96 %	76.50 %
ZW ($m_H = 2$ TeV)	80.14 %	93.85 %	76.20 %
ZZ ($m_H = 10$ TeV)	80.28 %	92.80 %	75.62 %
ZW ($m_H = 10$ TeV)	80.60 %	94.06 %	76.75 %
Background			
$qq \to ZZ$	48.57 %	48.93 %	24.65 %
$qq \to ZW$	51.90 %	51.08 %	27.65 %
Z + jet	20.37 %	28.39 %	8.02 %
$t\bar{t}$ at least 1 muon	3.14 %	60.31 %	2.00 %
$t\bar{t}$ 2 μ's any charge	13.84 %	61.31 %	8.76 %
$t\bar{t}$ 1 μ^+ and 1 μ^-	21.54 %	60.81 %	13.66 %

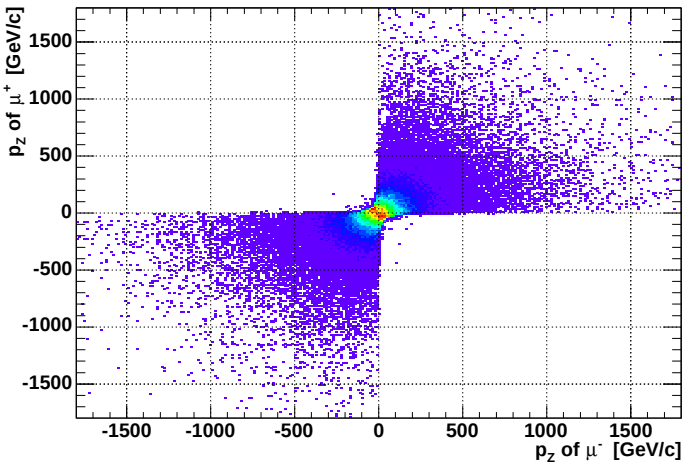

Figure 4.26: *Collinearity in p_Z between muon and anti-muon (parton level) in the signal process.*

$$\begin{cases} p_Z \text{ of } \mu^+ > \frac{-9\times10^3}{p_Z \text{ of } \mu^-} & \text{for } p_Z \text{ of } \mu^- > 0 \\ p_Z \text{ of } \mu^+ < \frac{-9\times10^3}{p_Z \text{ of } \mu^-} & \text{for } p_Z \text{ of } \mu^- < 0 \end{cases} \tag{4.6}$$

pass the selection. If more than one pair is left, then the one with the highest p_T is chosen. In Table 4.4 the reconstruction efficiencies after the p_Z collinearity request are listed. This reconstruction method is enough to single out the right pair, but not to single it out from the background pairs. Therefore other three requirement are imposed:

- 85 GeV $\leq M_{inv}(Z_{lep}) \leq$ 97 GeV ,
- $\eta_{\mu^-} - 2.8 < \eta_{\mu^+} < \eta_{\mu^-} + 2.8$,
- $p_T^{Z_{lep}} \geq 100$ GeV .

In Table 4.5 the relative and the total efficiencies are given.

The resolution R is defined as:

$$R = \frac{\text{parton level value - reconstucted value}}{\text{parton level value}} . \tag{4.7}$$

Table 4.4: *Efficiencies for $Z \to \mu^+\mu^-$ reconstruction, with the only requirement on the p_Z collinearity.*

Signal Samples	Efficiency
ZZ ($m_H = 0.5$ TeV)	99.19 %
ZW ($m_H = 0.5$ TeV)	98.67 %
ZZ ($m_H = 1$ TeV)	99.03 %
ZW ($m_H = 1$ TeV)	98.73 %
ZZ ($m_H = 2$ TeV)	98.87 %
ZW ($m_H = 2$ TeV)	98.81 %
ZZ ($m_H = 10$ TeV)	98.80 %
ZW ($m_H = 10$ TeV)	98.70 %

Background Samples	Efficiency
$qq \to ZZ$	94.51 %
$qq \to ZW$	91.38 %
Z + jet	84.63 %
$t\bar{t}$ at least 1 muon	98.10 %
$t\bar{t}$ 2 μ's any charge	97.71 %
$t\bar{t}$ 1 μ^+ and 1 μ^-	97.61 %

Table 4.5: *Selection efficiencies for the Z_{lep} reconstruction algorithm.*

Samples	M_{inv} cut	$\eta\eta$ cut	p_T cut	Combined
Signal				
ZZ ($m_H = 0.5$ TeV)	80.01 %	87.02 %	99.93 %	69.55 %
ZW ($m_H = 0.5$ TeV)	80.39 %	70.88 %	99.84 %	56.99 %
ZZ ($m_H = 1$ TeV)	79.80 %	87.12 %	99.92 %	69.13 %
ZW ($m_H = 1$ TeV)	80.19 %	77.70 %	99.89 %	62.05 %
ZZ ($m_H = 2$ TeV)	79.88 %	80.09 %	99.85 %	63.68 %
ZW ($m_H = 2$ TeV)	80.05 %	82.50 %	99.91 %	65.66 %
ZZ ($m_H = 10$ TeV)	80.41 %	78.17 %	99.82 %	62.63 %
ZW ($m_H = 10$ TeV)	80.23 %	82.95 %	99.90 %	66.16 %
Background				
$qq \to ZZ$	74.48 %	17.41 %	98.41 %	12.54 %
$qq \to ZW$	80.29 %	15.63 %	97.80 %	11.47 %
Z + jet	70.18 %	2.25 %	95.60 %	1.33 %
$t\bar{t}$ at least 1 muon	5.06 %	11.90 %	97.62 %	0.95 %
$t\bar{t}$ 2 μ's any charge	4.89 %	10.98 %	97.66 %	0.52 %
$t\bar{t}$ 1 μ^+ and 1 μ^-	5.22 %	11.67 %	97.39 %	0.87 %

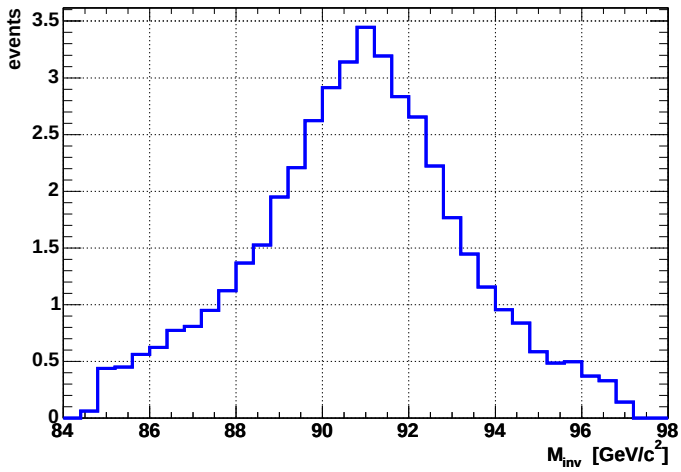

Figure 4.27: *Invariant mass of $Z \to \mu^+\mu^-$ in the no Higgs scenario signal sample ($m_H = 10$ TeV in ZZ events). Mean value is (90.9 ± 0.7) GeV and the width is $\Gamma = (2.1 \pm 0.9)$ GeV.*

A resolution of $R \sim 1.5$ % is obtained on $M_{inv}^{Z_{lep}}$ for the signals. In Figure 4.28 the resolution on the invariant mass of the Z into two muons is shown.

The resolution distribution is fitted using two Gaussian curves in order to control the tail at low masses. The deviation from the single Gaussian fit is due to the bremsstrahlung photon emission from muons. Therefore the invariant mass of the Z is underestimated. The resolution achieved is $(1.5 \pm 0.3)\%$ corresponding to the width of the first Gaussian.

4.3.4.2 $V \to jj$ Reconstruction

The selection of the jets from the vector boson decay is carried out using two algorithms, which follow two different approaches: *thinning* and *composition.* Both select only jets with $|\eta| < 3$. The jets previously recognized as tag jets are not taken into account.

Thinning The basic concept is the following: compute the invariant mass of all the selected jets, then remove the jets one by one until the invariant mass of all remaining jets is within a defined mass interval. In this analysis at most two jets are removed from the initial set. The procedure is the following:

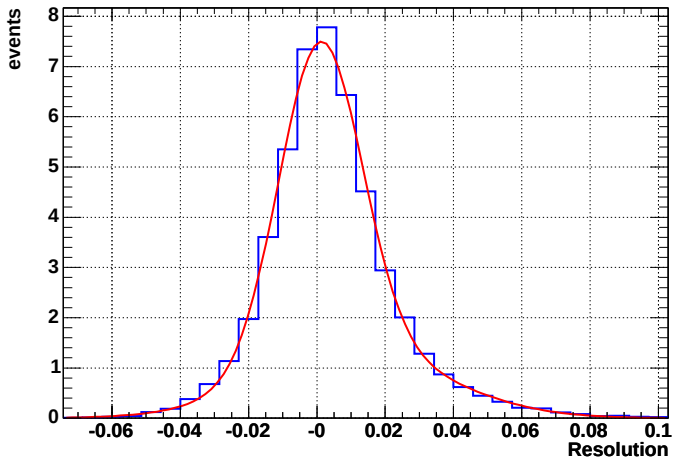

Figure 4.28: *Invariant mass resolution for* $Z \to \mu^+\mu^-$ *(*$m_H = 10$ *TeV in* ZZ *events).*

1. All the final state jets with $|\eta| < 3$ and $p_T > 25$ GeV are taken in account. In general this set of jets contains n jets:

$$\text{Initial set} \;=\; \begin{pmatrix} J_1 \\ J_2 \\ \dots \\ J_n \end{pmatrix} . \tag{4.8}$$

The invariant mass of the n jets is computed and if

$$40 \text{ GeV} < M_{inv}\left(\sum_{i=1}^{n} J_i\right) < 140 \text{ GeV} , \tag{4.9}$$

where J_i is the 4-vector of the i^{th} jet, then $\sum_{i=1}^{n} J_i$ is taken as the Lorentz vector of the vector boson. Otherwise, two cases can be identified:

(a) if $M_{inv}\left(\sum_{i=1}^{n} J_i\right) < 40$ GeV the thinning method fails.

(b) else if $M_{inv}\left(\sum_{i=1}^{n} J_i\right) > 140$ GeV then n sets, each made of *n-1* jets, are created.

$$\begin{pmatrix} J_1 \\ J_2 \\ \dots \\ J_n \end{pmatrix} \Longrightarrow \begin{pmatrix} J_2 \\ J_3 \\ \dots \\ J_n \end{pmatrix} \begin{pmatrix} J_1 \\ J_3 \\ \dots \\ J_n \end{pmatrix} \dots \begin{pmatrix} J_1 \\ J_2 \\ \dots \\ J_{n-1} \end{pmatrix} \tag{4.10}$$

2. The previous step is repeated for all the n sets of jets, with the following difference: if the statement (4.9) is satisfied by one of these sets, it does not become automatically the 4-vector of the vector boson, but it is loaded into a container. The sets which have the total invariant mass bigger than 140 GeV are split in *n-1* sets, each one made of *n-2* jets:

$$\begin{pmatrix} J_1 \\ \dots \\ J_{i-1} \\ J_{i-1} \\ \dots \\ J_n \end{pmatrix} \Longrightarrow \begin{pmatrix} J_2 \\ \dots \\ J_{i-1} \\ J_{i+1} \\ \dots \\ J_n \end{pmatrix} \dots \begin{pmatrix} J_1 \\ \dots \\ J_{i-2} \\ J_{i+1} \\ \dots \\ J_n \end{pmatrix} \dots \begin{pmatrix} J_1 \\ \dots \\ J_{i-1} \\ J_{i+1} \\ \dots \\ J_{n-1} \end{pmatrix} \tag{4.11}$$

3. A loop over the *n-1* sets of jets concludes the search. If the statement (4.9), without any exception, is false then the thinning method fails. Otherwise if the request on the total invariant mass of the set is satisfied, then the corresponding 4-vector is loaded into the previously introduced container.

4. If the container of the sets of jets is not empty, then the set with the highest p_T is associated to the vector boson.

Composition. This algorithm forms all possible jet pairs with:

- $p_Z^{jet_1} \cdot p_Z^{jet_2} \geq 0$,
- $p_T > 120$ GeV ,
- 74 GeV $< M_{inv}(\text{jet}_1 + \text{jet}_2) <$ 105 GeV .

If more than one pair is reconstructed, then the following is requested:

- $\Delta r < 2$, see Figure 4.29.

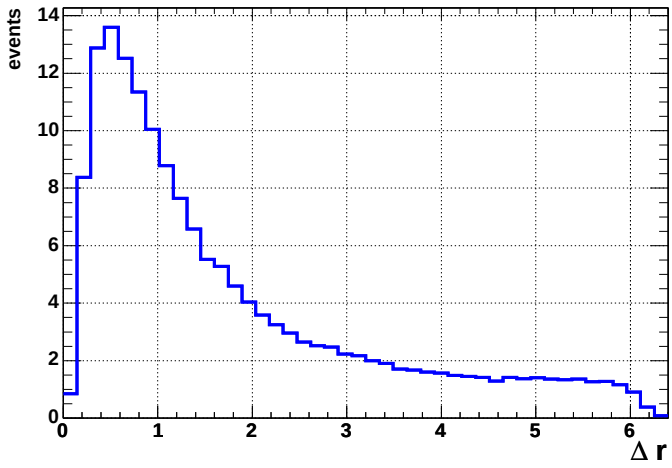

Figure 4.29: *Δr distribution for quarks from vector boson decay for the signal ($m_H = 10$ TeV in ZZ events, parton level).*

where Δr is defined as:

$$\Delta r = \sqrt{(\Delta\Phi)^2 + (\Delta\eta)^2}\,. \tag{4.12}$$

In case there are two or more pairs left, then the one with the highest p_T is chosen.

The composition algorithm is called if the thinning one fails. If the composition also fails, the thinning is called again but considering only jets with p_T greater that 200 GeV.

The hadronically decayed vector boson reconstruction efficiencies are listed in Table 4.6. In Figure 4.30 the invariant mass distributions for the processes $ZW \to ZW$ and $VV \to ZZ$ are shown. The two samples cannot be distinguished.

4.3.5 Cuts and Requests on the Signal

Many features of the signal can be exploited. The following requirements on the vector boson kinematic variables, such as invariant mass and transverse momentum, have been imposed:

Table 4.6: *Reconstruction efficiencies of vector bosons which decay hadronically.*

Samples	Thinning	Composition	Total
Signal			
ZZ $(m_H = 0.5\ TeV)$	50.63 %	13.92 %	64.55 %
ZW $(m_H = 0.5\ TeV)$	48.91 %	7.43 %	56.34 %
ZZ $(m_H = 1\ TeV)$	67.27 %	8.37 %	75.64 %
ZW $(m_H = 1\ TeV)$	54.15 %	7.41 %	61.56 %
ZZ $(m_H = 2\ TeV)$	62.77 %	8.23 %	71.00 %
ZW $(m_H = 2\ TeV)$	58.70 %	6.96 %	65.66 %
ZZ $(m_H = 10\ TeV)$	60.97 %	8.31 %	69.28 %
ZW $(m_H = 10\ TeV)$	60.46 %	6.45 %	66.91 %
Background			
$qq \rightarrow ZZ$	28.07 %	6.04 %	34.11 %
$qq \rightarrow ZW$	28.43 %	2.99 %	31.42 %
$Z + jet$	20.29 %	∼0 %	20.29 %
$t\bar{t}$ *at least 1 muon*	30.77 %	7.69 %	38.46 %
$t\bar{t}$ *2* μ*'s any charge*	∼50 %	∼0 %	∼50 %
$t\bar{t}$ *1* μ^+*and 1* μ^-	26.60 %	10.64 %	37.24 %

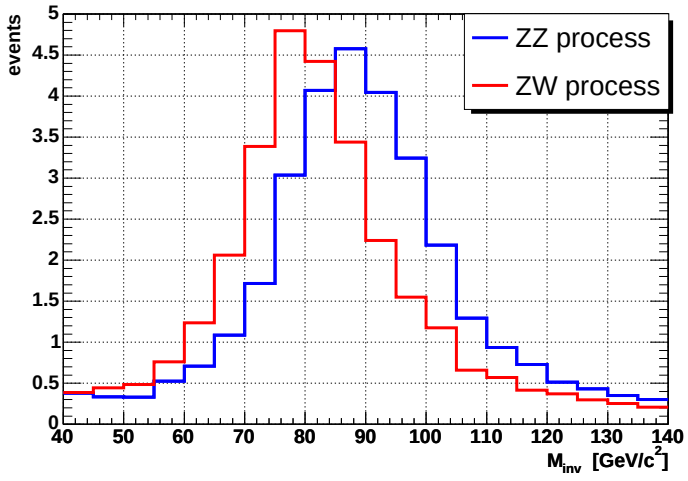

Figure 4.30: *Invariant mass of vector boson reconstructed from the jets with* $m_H = 10\ TeV$*. Since the mean values are* $m_W = (81 \pm 4)\ GeV$ *and* $m_Z = (88 \pm 4)\ GeV$*and the width for both is* $\Gamma_V = (11 \pm 5)\ GeV$*, the two samples cannot be distinguished.*

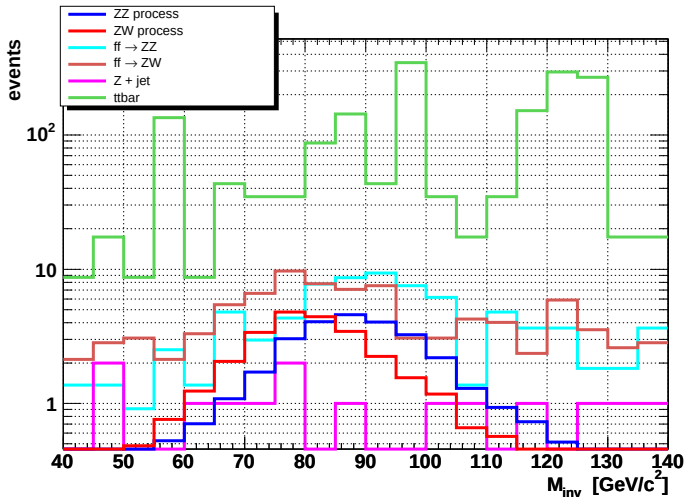

Figure 4.31: *Jet-jet invariant mass ($m_{V_{had}}$) distribution for the signal ($m_H = 10000$ GeV) and the background.*

- 50 GeV $< m_{V_{had}} <$ 120 GeV.

  Figure 4.31 shows the signal and background distributions as function of the jet-jet invariant mass $m_{V_{had}}$: some background is suppressed by this cut, in particular the combinatorial one. The $Z + jet$ and $t\bar{t}$ backgrounds do not exhibit a resonance structure. In Table 4.7 the efficiencies after this cut, for signal and background samples, are given. The mean efficiency for the signal is $\sim 93\%$, whereas for the background goes from $\sim 83\%$ to 40%.

- $p_T^{Z_{had}} > 110$ GeV.

  In spite of the low statistics for the background, it is possible to see how this cut acts. The p_T distributions for the background is peaked at low values. Therefore making a request on the transverse momentum of the vector boson which decays hadronically, more than half of the background can be discarded (Table 4.8). This cut also affects the signal, in particular the ZW's, which does not have a resonant channel for the Higgs. As the "Higgs" mass increases, ZW channels tend to have the same efficiency as the ZZ.

Table 4.7: *Efficiencies after the cuts on the invariant mass of the vector boson which decays hadronically. The efficiencies correspond to the events in which the vector boson was reconstructed.*

Signal Samples	$m_{V_{had}}$
$ZZ\ (m_H = 0.5\ TeV)$	94.26 %
$ZW\ (m_H = 0.5\ TeV)$	91.36 %
$ZZ\ (m_H = 1\ TeV)$	95.45 %
$ZW\ (m_H = 1\ TeV)$	93.21 %
$ZZ\ (m_H = 2\ TeV)$	92.19 %
$ZW\ (m_H = 2\ TeV)$	93.60 %
$ZZ\ (m_H = 10\ TeV)$	92.49 %
$ZW\ (m_H = 10\ TeV)$	93.27 %

Background	$m_{V_{had}}$
$qq \rightarrow ZZ$	82.86 %
$qq \rightarrow ZW$	77.78 %
Z + *jet*	64.29 %
$t\bar{t}$ *at least 1 muon*	40.00%
$t\bar{t}$ *2* μ*'s any charge*	75.00%
$t\bar{t}$ *1* μ^+ *and 1* μ^-	82.86 %

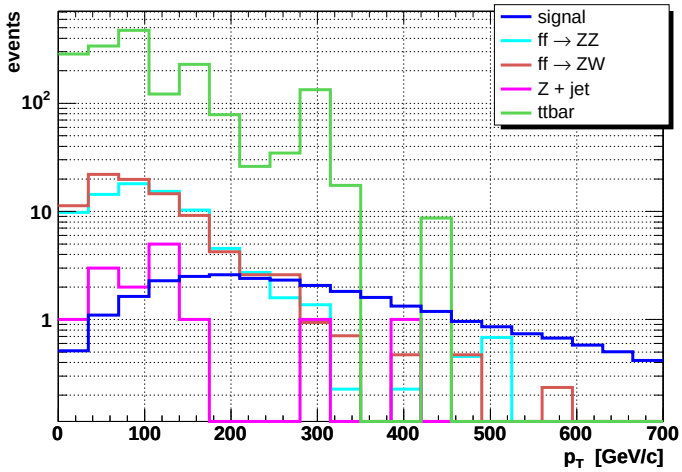

Figure 4.32: *Transverse momentum distribution for the signal ($m_H = 10000$ GeV) and the background, of the vector boson reconstructed from jets.*

Table 4.8: *Efficiencies after the cuts on the transverse momentum of the vector boson which decays hadronically. The efficiencies correspond to the events in which the vector boson was reconstructed.*

Signal Samples	$p_T^{Z_{had}}$
ZZ ($m_H = 0.5$ TeV)	87.75 %
ZW ($m_H = 0.5$ TeV)	75.26 %
ZZ ($m_H = 1$ TeV)	93.61 %
ZW ($m_H = 1$ TeV)	82.12 %
ZZ ($m_H = 2$ TeV)	89.64 %
ZW ($m_H = 2$ TeV)	87.86 %
ZZ ($m_H = 10$ TeV)	88.60 %
ZW ($m_H = 10$ TeV)	88.10 %

Background	$p_T^{Z_{had}}$
$qq \to ZZ$	43.43 %
$qq \to ZW$	39.42 %
Z + *jet*	50.00 %
$t\bar{t}$ *at least 1 muon*	40.00 %
$t\bar{t}$ *2* μ*'s any charge*	0 %
$t\bar{t}$ *1* μ^+ *and 1* μ^-	58.57 %

- $M_{inv}(\text{jet tag}_1 + \text{jet tag}_2) > 450$ GeV.

  The invariant mass of the tagging jet system is used to discriminate between real spectator jets of the signal and fake forward jets from background processes. In fact the invariant mass spectrum (see Figure 4.33) of the two tag jets decreases steeply below 500 GeV, while the same spectrum for all backgrounds decreases at lower invariant masses. The requirement of tag jet invariant mass bigger than 450 GeV is therefore applied. In Table 4.9 the signal and background efficiencies are shown.

- Angle between μ^+ and μ^- three-vectors (lab. frame) in the range (0.075÷1.67) rad.

  As is shown in Figure 4.34 the distribution of the angle between the muon and the anti-muon for the signal is limited to the region ∼(0.07÷1.7) rad.

- Angle between the two vector boson three-vectors (lab. frame) greater than 0.2 rad.

  The spectrum of the angular difference between the vector boson three-vectors (see Figure 4.35) for the signal grows from 0 up to π, whereas for the background it is constant. Therefore a cut at low angular difference can increase $S/\sqrt{B}$. Table 4.11 shows the fraction of events that survives this cut. A harder cut (*i.e.* at 0.5 rad) will be placed only when

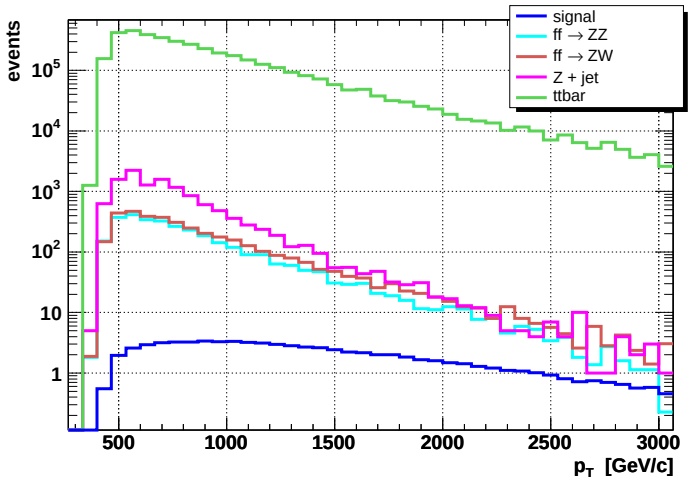

Figure 4.33: *Invariant mass distribution of the sum of tag jet 4-vectors. (Signal m_H=10000 GeV, in ZZ)*

Table 4.9: *Efficiencies after the cuts on the invariant mass of the jets tag. The efficiencies correspond to the events in which the vector boson which decays hadronically was reconstructed.*

Signal Samples	$M_{inv}^{tag\ jets}$
$ZZ\ (m_H = 0.5\ TeV)$	99.66 %
$ZW\ (m_H = 0.5\ TeV)$	99.64 %
$ZZ\ (m_H = 1\ TeV)$	99.77 %
$ZW\ (m_H = 1\ TeV)$	99.70 %
$ZZ\ (m_H = 2\ TeV)$	99.74 %
$ZW\ (m_H = 2\ TeV)$	99.78 %
$ZZ\ (m_H = 10\ TeV)$	99.74 %
$ZW\ (m_H = 10\ TeV)$	99.76 %

Background	$M_{inv}^{tag\ jets}$
$qq \rightarrow ZZ$	95.43 %
$qq \rightarrow ZW$	97.09 %
$Z + jet$	85.71 %
$t\bar{t}$ *at least 1 muon*	100 %
$t\bar{t}$ *2* μ*'s any charge*	100 %
$t\bar{t}$ *1* μ^+ *and 1* μ^-	100 %

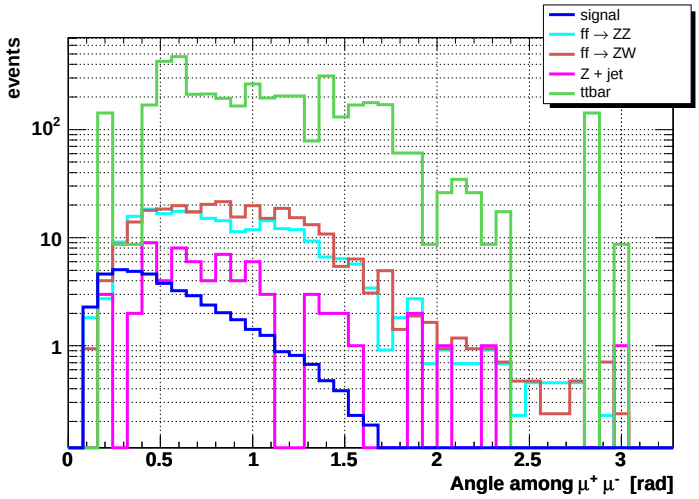

Figure 4.34: *Distribution of the angle between muon and anti-muon from the decay of the* Z *boson* ($m_H = 10000\ GeV$).

Table 4.10: *Efficiencies after the cut on the angle between the two muons from the* Z *boson decay. The efficiencies correspond to the events in which thee vector boson which decays hadronically was reconstructed.*

Signal Samples	$\widehat{\mu^+\mu^-}$
$ZZ\ (m_H = 0.5\ TeV)$	98.75 %
$ZW\ (m_H = 0.5\ TeV)$	97.84 %
$ZZ\ (m_H = 1\ TeV)$	99.58 %
$ZW\ (m_H = 1\ TeV)$	98.62 %
$ZZ\ (m_H = 2\ TeV)$	98.94 %
$ZW\ (m_H = 2\ TeV)$	99.01 %
$ZZ\ (m_H = 10\ TeV)$	99.07 %
$ZW\ (m_H = 10\ TeV)$	98.77 %

Background	$\widehat{\mu^+\mu^-}$
$qq \to ZZ$	92.86 %
$qq \to ZW$	93.39 %
Z + *jet*	71.43 %
$t\bar{t}$ *at least 1 muon*	80.00 %
$t\bar{t}$ *2* μ*'s any charge*	100 %
$t\bar{t}$ *1* μ^+ *and 1* μ^-	71.43 %

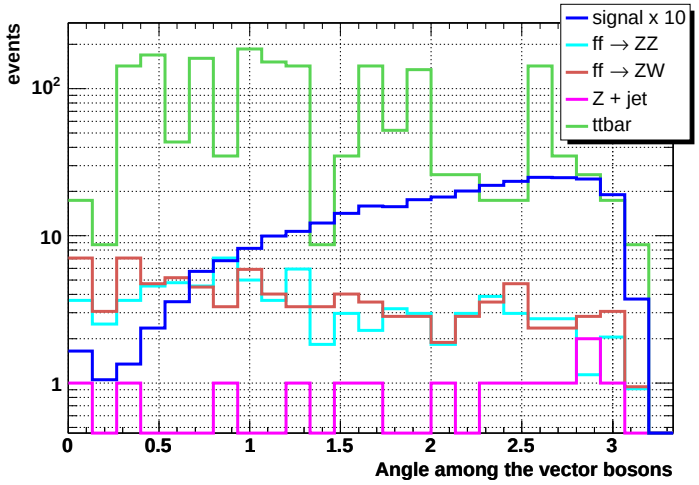

Figure 4.35: *Distribution of the angle between the vector bosons ($m_H = 10000$ GeV).*

background statistics will be huge.

- Δr between the two vector bosons greater than 1.

  In Figure 4.36 the distributions of Δr for signal and background samples are shown. It would be better to place a more stringent cut *i.e.* $1.5 < \Delta r < 5$, but due to low background statistics it would affect the signal over background ratio. In future when background statistics will be huge, this cut will also be refined.

The combined efficiencies for this set of cuts are shown in Table 4.13.

4.3.6 Summary on the Selection Criteria and Total Efficiencies

One of the major background sources is the pile-up (section 4.3.1). A cut at 25 GeV on the jet transverse momentum allows to suppress it while maintaining a high signal efficiency (close to 100%). Also a large part of the background survives this cut, except $Z + jet$ which is reduced by more than a factor two. This is due to the low average p_T of the single jet coming from the $Z + jet$ hard process (see Figure 4.16).

Table 4.11: *Efficiencies after the cuts on the angle between the two reconstructed vector bosons. The efficiencies correspond to the events in which the hadronically decayed vector boson was reconstructed.*

Signal Samples	$\widehat{VV}$
$ZZ\ (m_H = 0.5\ TeV)$	99.27 %
$ZW\ (m_H = 0.5\ TeV)$	98.83 %
$ZZ\ (m_H = 1\ TeV)$	99.49 %
$ZW\ (m_H = 1\ TeV)$	99.24 %
$ZZ\ (m_H = 2\ TeV)$	99.31 %
$ZW\ (m_H = 2\ TeV)$	99.25 %
$ZZ\ (m_H = 10\ TeV)$	99.35 %
$ZW\ (m_H = 10\ TeV)$	99.42 %

Background	$\widehat{VV}$
$qq \rightarrow ZZ$	93.43 %
$qq \rightarrow ZW$	90.48 %
Z + *jet*	92.86 %
$t\bar{t}$ *at least 1 muon*	100 %
$t\bar{t}$ *2* μ*'s any charge*	100 %
$t\bar{t}$ *1* μ^+ *and 1* μ^-	95.71 %

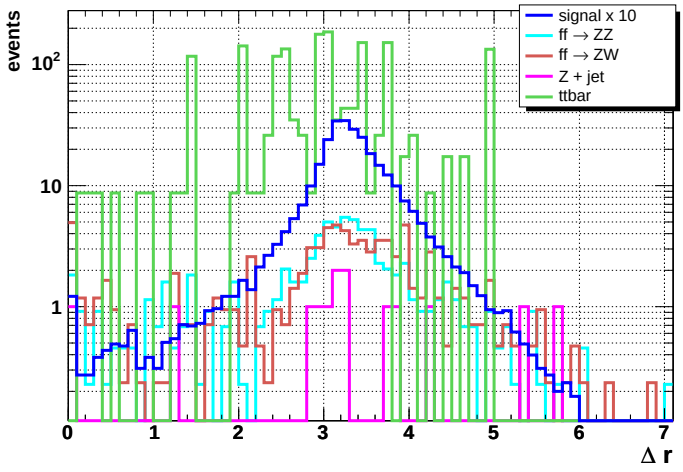

Figure 4.36: Δr *distribution between the two vector bosons* ($m_H = 10000\ GeV$).

Table 4.12: *Efficiencies after the cuts on the Δr between the two reconstructed vector bosons. The efficiencies correspond to the events in which the $V \to jj$ was reconstructed.*

Signal Samples	Δr
ZZ $(m_H = 0.5\ TeV)$	98.70 %
ZW $(m_H = 0.5\ TeV)$	96.98 %
ZZ $(m_H = 1\ TeV)$	99.04 %
ZW $(m_H = 1\ TeV)$	98.18 %
ZZ $(m_H = 2\ TeV)$	98.49 %
ZW $(m_H = 2\ TeV)$	98.45 %
ZZ $(m_H = 10\ TeV)$	98.42 %
ZW $(m_H = 10\ TeV)$	98.69 %

Background	Δr
$qq \to ZZ$	91.71 %
$qq \to ZW$	86.77 %
Z + *jet*	92.86 %
$t\bar{t}$ *at least 1 muon*	100 %
$t\bar{t}$ *2* μ*'s any charge*	100 %
$t\bar{t}$ *1* μ^+ *and 1* μ^-	91.43 %

Table 4.13: *Combined efficiencies after the six cuts explained in the text. The efficiencies correspond to the events in which the $V \to jj$ was reconstructed.*

Signal Samples	**Combined**
ZZ $(m_H = 0.5\ TeV)$	81.83 %
ZW $(m_H = 0.5\ TeV)$	67.55 %
ZZ $(m_H = 1\ TeV)$	89.05 %
ZW $(m_H = 1\ TeV)$	76.35 %
ZZ $(m_H = 2\ TeV)$	81.66 %
ZW $(m_H = 2\ TeV)$	81.66 %
ZZ $(m_H = 10\ TeV)$	81.17 %
ZW $(m_H = 10\ TeV)$	81.50 %

Background	**Combined**
$qq \to ZZ$	31.43 %
$qq \to ZW$	24.34 %
Z + *jet*	7.14 %
$t\bar{t}$ *at least 1 muon*	20.00 %
$t\bar{t}$ *2* μ*'s any charge*	0 %
$t\bar{t}$ *1* μ^+ *and 1* μ^-	32.86 %

Since the signature of the signal is well defined, requirements on event topology (Section 4.3.2) are applied and are the most powerful tool to reject the background. The mean efficiency for the signal samples is about 44%, whereas for the background it is only a few percent. Another set of requirements on global kinematic variables of the event can further reduce the remaining background (Section 4.3.3).

The two vector bosons in the final state have to be reconstructed (Section 4.3.4). The reconstruction efficiency of the Z which decays leptonically (see Section 4.3.4.1) is close to 99% for the signal samples, whereas for the background it is 3÷4% lower. Important cuts on the muon pairs coming from the Z decay are applied. While the signal efficiencies are around 64%, the background ones are about one percent for Z + *jet* and $t\bar{t}$ and 12% for the ZZ, ZW production.

Also the V which decays hadronically must be reconstructed. Two different methods are adopted: thinning and composition (see Section 4.3.4.2). The mean reconstruction efficiency is 66% for signal and 30% for the background. Figure 4.30 addresses the issue of the discrimination of $VV \to ZZ$ from $ZW \to ZW$: they are not distinguishable.

After the vector boson reconstruction, a set of cuts is applied (Section 4.3.5). The most important is the cut on the p_T of the vector boson which decays hadronically: it reduces to a half the number of background events in which the V has been reconstructed. The low statistics for the background data sets does not allow to quantify the performance of the other cuts, however their effect is shown in Table 4.13: their combination allows to reject about 80% of the reconstructed vector bosons which decay hadronically for the background, and only 20% for the signal.

The total efficiencies after all cuts are given in Table 4.14 for the signal and in Table 4.15 for the background.

Background

After all the cuts only a small fraction of the background survives. In particular the Z + *jet* and $t\bar{t}$, which have a very high cross section (see Table 3.2), are kept under control.

Table 4.14: *Total efficiencies for the signal samples.*

Signal Samples	Total Efficiency
ZZ ($m_H = 0.5$ TeV)	15.57 %
ZW ($m_H = 0.5$ TeV)	8.46 %
ZZ ($m_H = 1$ TeV)	21.75 %
ZW ($m_H = 1$ TeV)	12.17 %
ZZ ($m_H = 2$ TeV)	16.08 %
ZW ($m_H = 2$ TeV)	15.67 %
ZZ ($m_H = 10$ TeV)	14.93 %
ZW ($m_H = 10$ TeV)	16.30 %

Table 4.15: *Total efficiencies for the background samples.*

Background Samples	Total Efficiency
$qq \rightarrow ZZ$	0.04 %
$qq \rightarrow ZW$	0.03 %
Z + *jet*	0 %
$t\bar{t}$ *at least 1 muon*	0.0005 %
$t\bar{t}$ *2* μ*'s any charge*	0 %
$t\bar{t}$ *1* μ^+ *and 1* μ^-	0.0027 %

Signal

The efficiency of the signal is quite high for all the samples and, as will explained in the following section, allows to reach a good signal over background ratio.

Since the analysis is optimized for the no-Higgs scenario, the efficiencies for high Higgs masses are larger than the ones for low Higgs mass (m_H = 500 GeV). It is important to notice that the efficiencies for $m_H = 500$ GeV and $m_H = 1000$ GeV in ZW are smaller than the others for two related reason:

1. the analysis is tuned on the ZZ process;
2. the ZZ process, at (quite) low Higgs masses, has a resonant s channel with Higgs exchange (see diagrams in Figure 1.4).

Tuning the analysis on the ZZ process does not bias the final result. In fact for the no-Higgs scenario the differences in the kinematics between ZW and ZZ processes are suppressed (see Figures 1.4 and 1.5) and the two efficiencies (and also the cross sections, see Table 3.1) become equal. On the other hand, in case of a light Higgs boson mass, the ZW process has a very small cross section with respect to the ZZ one, which has a resonance at $\sqrt{s} \simeq m_H$ due the s channel Higgs exchange diagram.

For this reasons and for the fact that the two processes are not experimentally distinguishable, in the following, for the signal over background ratio computation, the two signal event samples will be merged.

4.4 The Results

The goal of this analysis is the reconstruction of the vector boson fusion processes and the simultaneous rejection of the background. In Figures 4.37 and 4.38 the selection efficiencies, as a function of the invariant mass of the VV pair, are shown. The efficiencies for the signals grow with the VV centre-of-mass energy, reaching 30 % in the region of major interest, *i.e.* 500 GeV (1 TeV) for the $m_H = 500$ GeV ($m_H = 1$ TeV) sample and over 700 GeV for the no-Higgs scenario samples (m_H at 2 TeV and 10 TeV). The background efficiency is below the percent level.

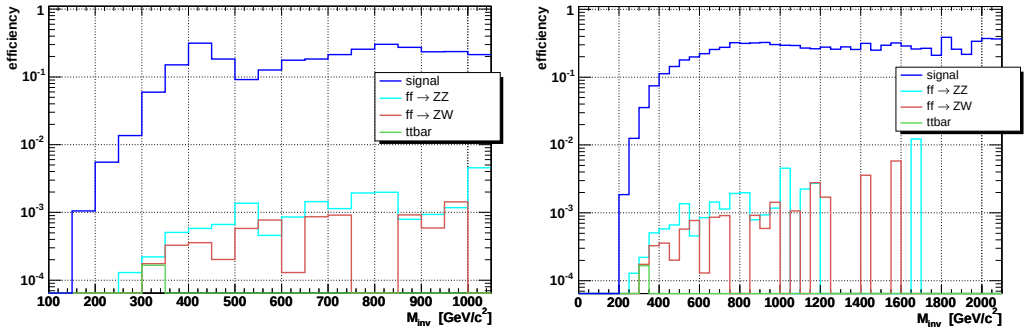

Figure 4.37: *Efficiency as a function of invariant mass of the* VV*-fusion process, for* $m_H = 500\ GeV$ *and* $m_H = 1000\ GeV$.

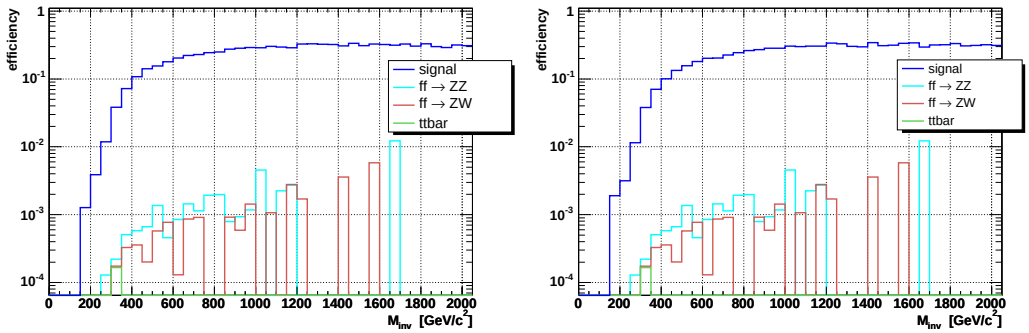

Figure 4.38: *Efficiency as a function of invariant mass of the* VV*-fusion process, for* $m_H = 2000\ GeV$ *and* $m_H = 10000\ GeV$.

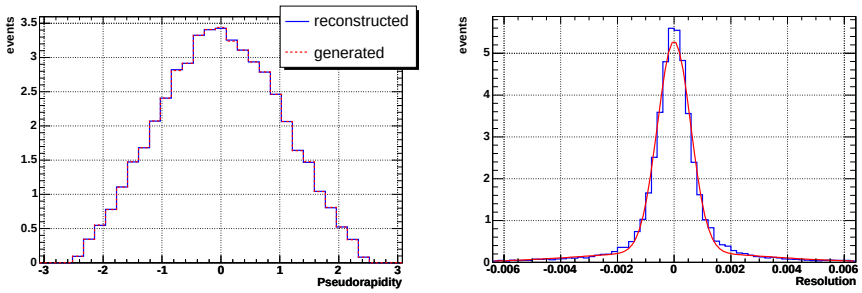

Figure 4.39: *Left: pseudorapidity distribution for the two muons in the final state, compared with the generated muon η. Right: the corresponding resolution on the muons pseudorapidity. ($m_H = 10000$ GeV)*

In order to measure the main parameters of the VV-fusion process, *i.e.* η, p_T and M_{inv} for each boson have to be well known, together with the invariant mass of the VV state.

To estimate the resolution, see Eq. (4.7), on the reconstructed signal observables, a comparison with the Monte Carlo generated observables has been carried out.

As CMSJET does not assume any jet energy calibration, the jet energy is underestimated; moreover no bremsstrahlung radiation for the muons can be evaluated with the fast simulation. Therefore a sum of two Gaussians is used to fit the resolution distributions, where the second one describes the tail at low energies. However, at this stage of the study, the only interesting parameter is the width of the Gaussian which fits the peak.

All the plots presented here are referred to an integrated luminosity of 100 fb^{-1}, corresponding to one year of high luminosity running.

4.4.1 Observables in VV-fusion

4.4.1.1 Muon Observables

The CMS muon system (see Section 2.2.5) will have a high resolution on the muon track measurements, thus the CMSJET fast and simplified simulation is acceptable for this study.

In Figures 4.39, 4.40 and 4.41 pseudorapidity, transverse momentum and en-

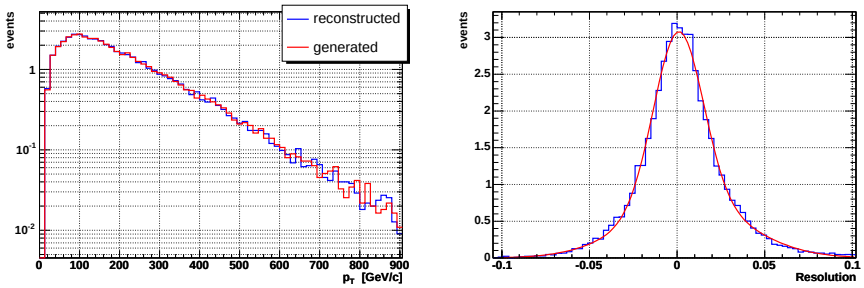

Figure 4.40: *Left: transverse momentum distribution for the two muons in the final state, compared with the generated muons p_T. Right: the corresponding resolution on the transverse momentum. ($m_H = 10000\ GeV$)*

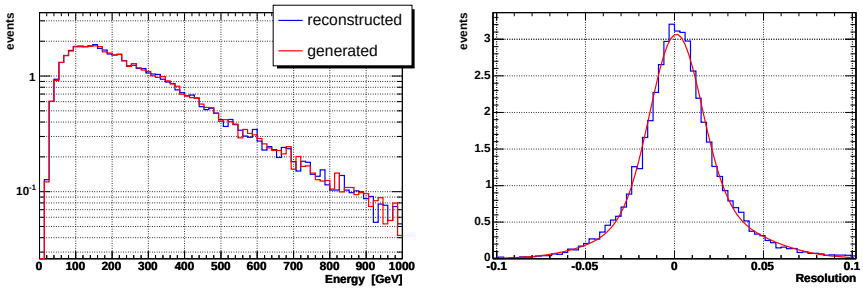

Figure 4.41: *Left: energy distribution for the two muons in the final state, compared with the generated muon energy. Right: the corresponding resolution. ($m_H = 10000\ GeV$)*

ergy distributions with the respective resolutions are shown. The distributions are referred to the no-Higgs scenario (*i.e.* $m_H = 10$ TeV), the distributions are similar for all the other signal samples.

The resolutions are:

- $R_\eta \simeq (0.06 \pm 0.01)\%$,
- $R_{p_T} \simeq (1.8 \pm 0.3)\%$,
- $R_E \simeq (1.8 \pm 0.3)\%$.

4.4.1.2 Vector Bosons Observables

The vector boson reconstruction is the core of the analysis, since it allows to compute the energy scale of the process, *i.e.* the invariant mass of the two vector bosons system, and to suppress the background. A good resolution on η, p_T and M_{inv} of the vector boson has been achieved. Of course the Z boson which decays leptonically is better reconstructed than the vector boson which decays into hadrons.

- $Z \to \mu^+\mu^-$:
  - $R_\eta \simeq (0.15 \pm 0.07)\%$,
  - $R_{p_T} \simeq (1.8 \pm 0.4)\%$,
  - $R_{M_{inv}} \simeq (1.5 \pm 0.3)\%$.
- $V \to jj$:
  - $R_\eta \simeq (3 \pm 1)\%$,
  - $R_{p_T} \simeq (8 \pm 3)\%$,
  - $R_{M_{inv}} \simeq (13 \pm 3)\%$.

In Figures 4.42, 4.43 and 4.44 the η, p_T and M_{inv} spectra of the Z boson which decays leptonically are shown, while in Figure 4.45, 4.46 and 4.47 are plotted the ones for the boson which decays hadronically.

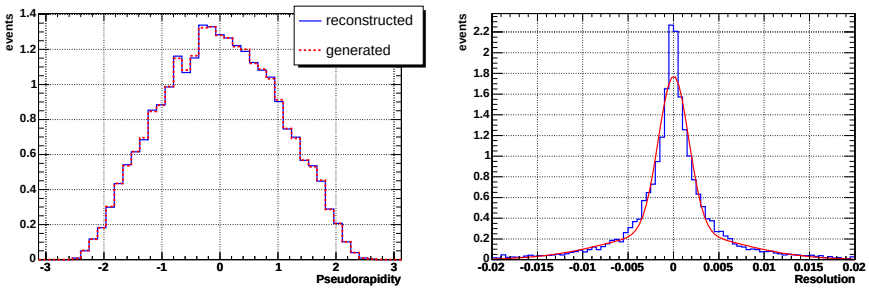

Figure 4.42: *Left: pseudorapidity distribution for the Z boson which decays leptonically, compared with the generated one. Right: resolution on pseudorapidity.* ($m_H = 10000\ GeV$)

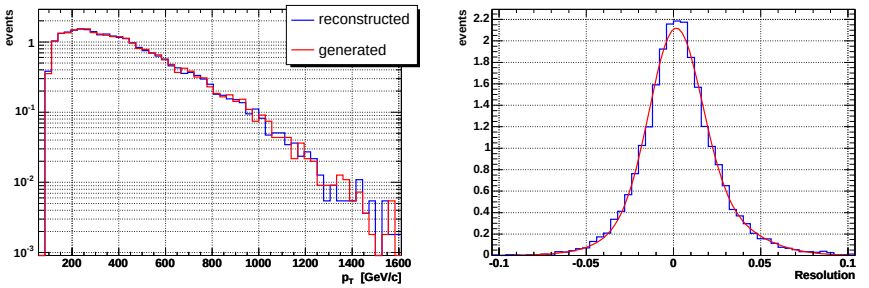

Figure 4.43: *Left: transverse momentum distribution for the Z boson which decays leptonically, compared with the generated one. Right: resolution on transverse momentum.* ($m_H = 10000\ GeV$)

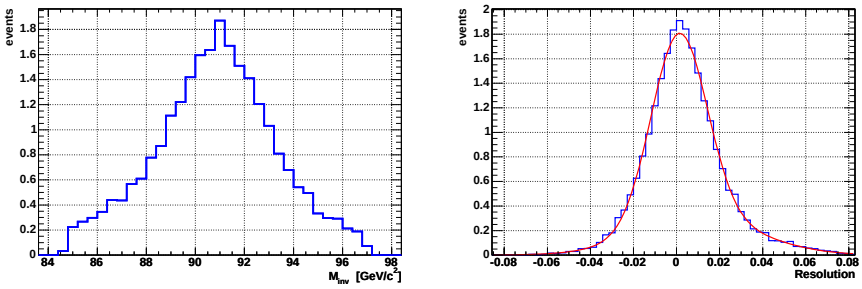

Figure 4.44: *Left: invariant mass distribution for the Z boson which decays leptonically. Right: corresponding resolution.* ($m_H = 10000\ GeV$)

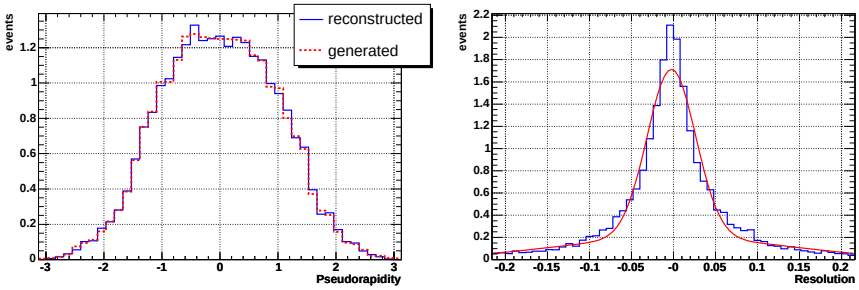

Figure 4.45: *Left: pseudorapidity distribution for the Z boson which decays hadronically, compared with the generated one. Right: resolution on pseudorapidity.* ($m_H = 10000\ GeV$)

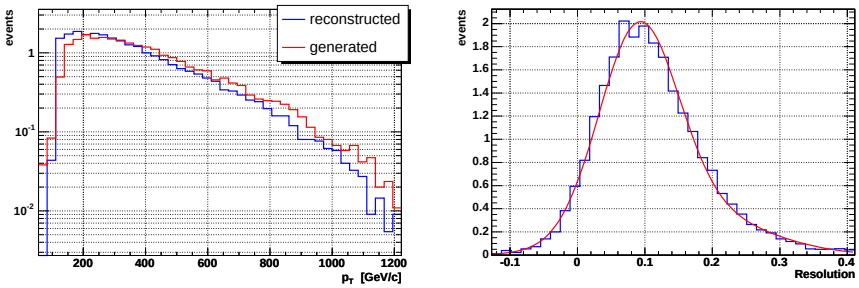

Figure 4.46: *Left: transverse momentum distribution for the Z boson which decays hadronically, compared with the generated one. Right: resolution on transverse momentum.* ($m_H = 10000\ GeV$)

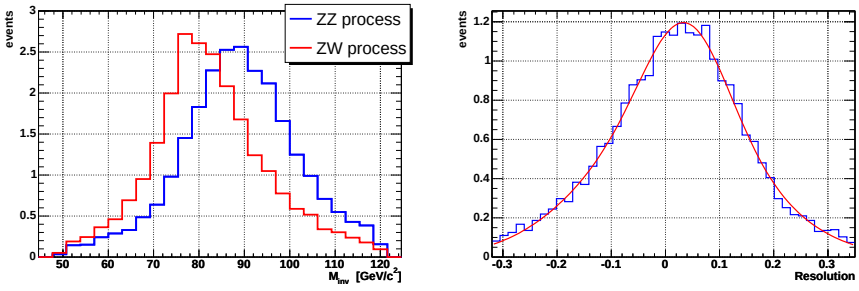

Figure 4.47: *Left: invariant mass distribution for the Z boson which decays hadronically. Right: corresponding resolution.* ($m_H = 10000\ GeV$)

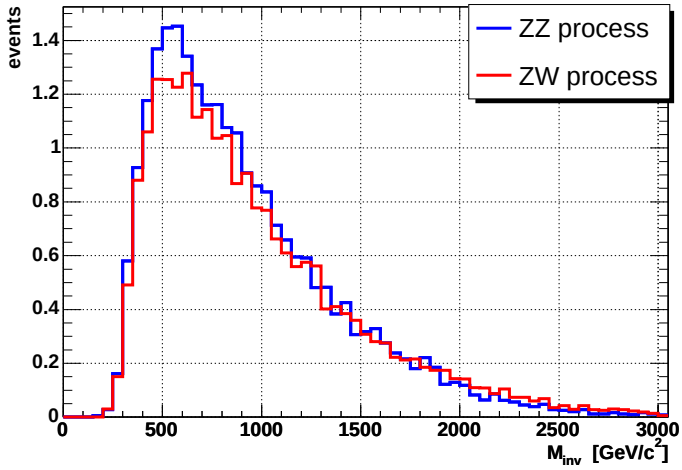

Figure 4.48: *Number of reconstructed events as a function of the* VV *invariant mass.* ($m_H = 10000$ *GeV)*

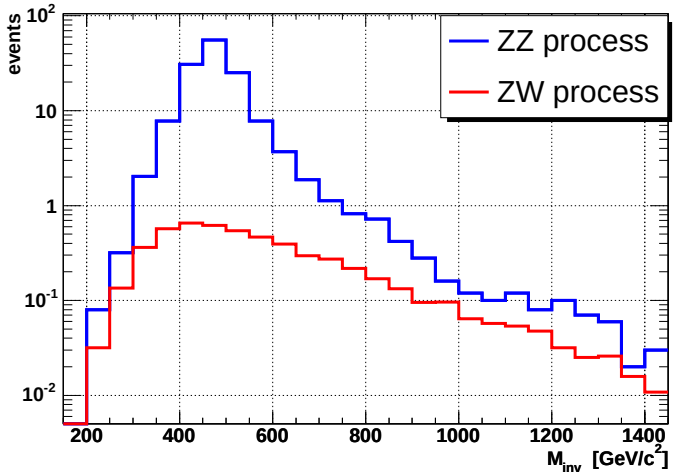

Figure 4.49: *Number of reconstructed events as a function of the* VV *invariant mass.* ($m_H = 500$ *GeV)*

4.4.1.3 *VV*-fusion Invariant Mass

As the histograms 4.48 and 4.49 show, as the exchanged quantum mass (over 1 TeV the term "Higgs boson" loses its meaning) increases, the two channels tend to have the same VV invariant mass spectrum. The two cross section values and the two reconstruction efficiencies become equal (see Tables 3.1 and 4.14). This is due to the presence of the s-channel Feynman diagram (in which the symmetry breaking quantum is exchanged) only for the ZZ process. If m_H increases, this channel is suppressed by the SB boson's propagator ($\sim 1/m_H^2$). Moreover at high energy, differences between m_W and m_Z become negligible. Therefore for m_H and $\sqrt{s} \gg (m_W, m_Z)$ the two cross section spectra tend to coincide. The crucial issue is if they are experimentally separable. The answer after this analysis is negative, because the invariant mass spectra of the Z (from ZZ process) and the W (from the ZW process) bosons are not sufficiently separated (the difference between the central values is less than one standard deviation). Therefore there are no observables that allow to discriminate from which of the two process the event comes from.

Since the two processes studied

$$pp \to j_F j_B Z_L Z_L + X \to j_F j_B \mu^+ \mu^- jj + X$$

$$pp \to j_F j_B Z_L W_L + X \to j_F j_B \mu^+ \mu^- jj + X$$

cannot be separated, in the VV-fusion invariant mass plots and in the signal over background ratio computation, the respective reconstructed events are merged.

The results of the event selection are plotted in Figures 4.50, 4.51,4.52 and 4.53. Each of these histograms shows the number of reconstructed events as a function of the invariant mass of the longitudinal vector boson system. On the same plot also background distributions are shown. These plots correspond to an integrated luminosity of 100 fb^{-1}. The relative resolution spectra are shown in Figures 4.54 and 4.55.

A good sensitivity is achieved to m_{VV} for all the Higgs masses considered. The resolution for the different signal datasets are:

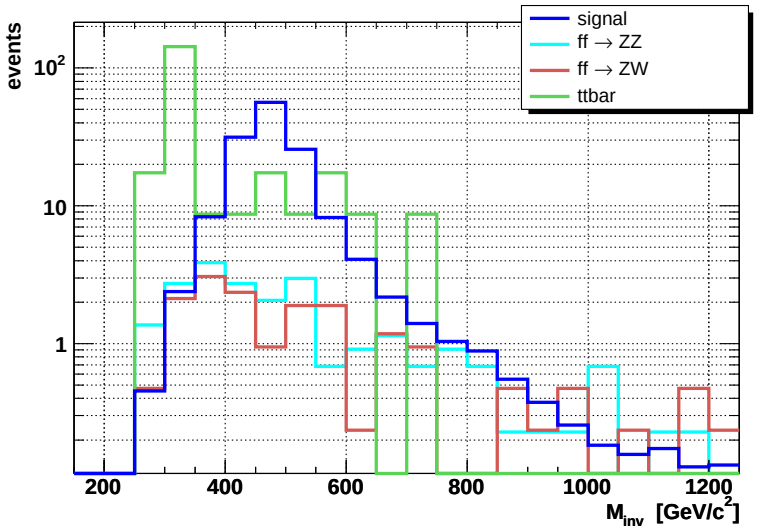

Figure 4.50: *Number of reconstructed events as a function of the* VV *invariant mass. Signal compared with background.* ($m_H = 500$ *GeV*)

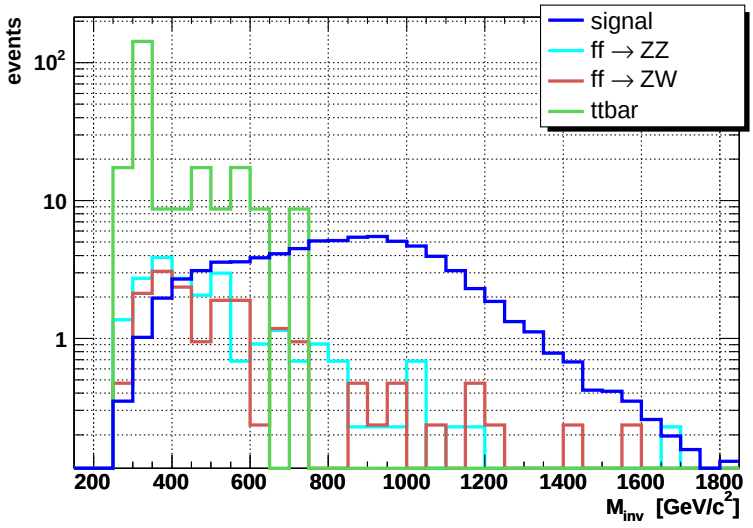

Figure 4.51: *Number of reconstructed events as a function of the* VV *invariant mass. Signal compared with background.* ($m_H = 1000$ *GeV*)

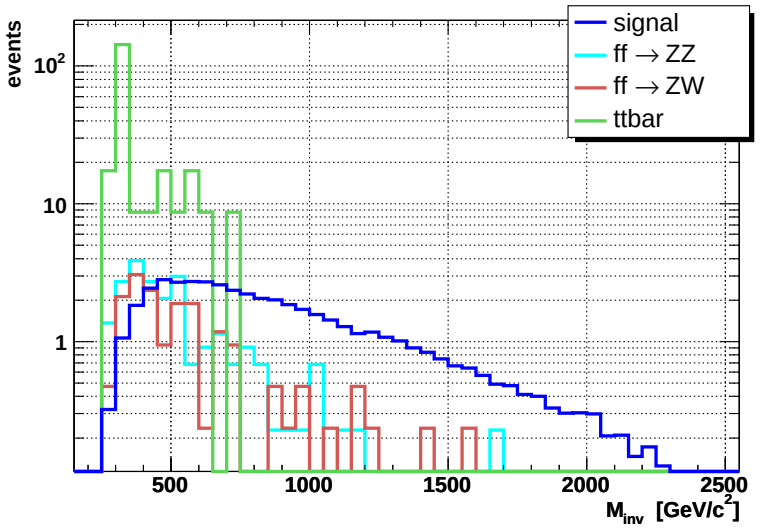

Figure 4.52: *Number of reconstructed events as a function of the* VV *invariant mass. Signal compared with background. ($m_H = 2000$ GeV)*

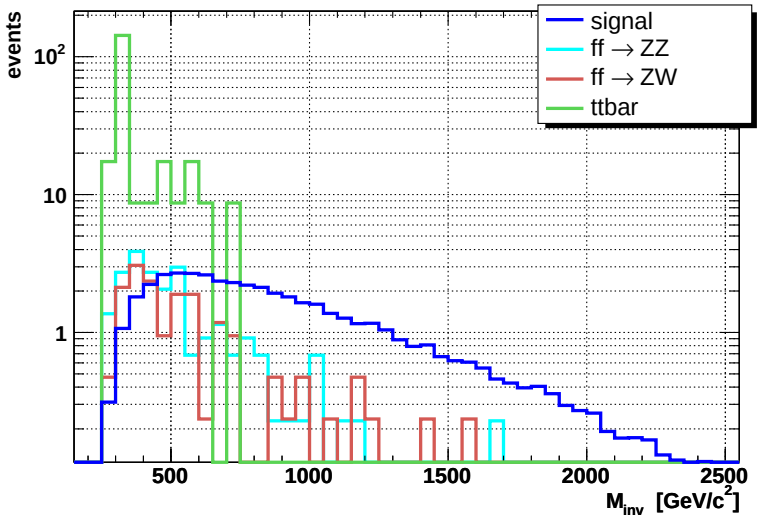

Figure 4.53: *Number of reconstructed events as a function of the* VV *invariant mass. Signal compared with background. ($m_H = 10000$ GeV)*

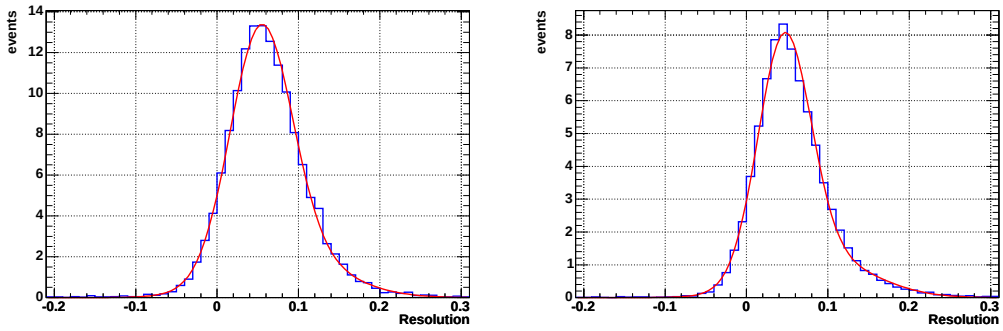

Figure 4.54: *Resolution on the* VV *invariant mass. (left:* $m_H = 500$ *GeV. Right:* $m_H = 1000$ *GeV)*

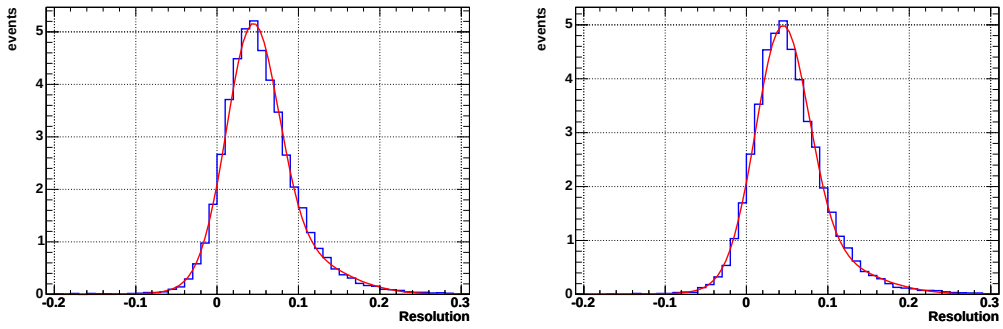

Figure 4.55: *Resolution on the* VV *invariant mass. (left:* $m_H = 2000$ *GeV. Right:* $m_H = 10000$ *GeV)*

Table 4.16: *Number of signal events after 100 fb^{-1} of integrated luminosity. The statistical uncertainty is given.*

Signal				
Samples	**0<M_{inv}^{VV}<1 TeV**	**1<M_{inv}^{VV}<2 TeV**	**M_{inv}^{VV}>2 TeV**	**All**
$m_H = 500\ GeV$	143.8±1.2	1.29±0.09	0.31±0.02	145.4±1.2
$m_H = 1000\ GeV$	55.0±0.4	22.0±0.3	0.33±0.03	77.3±0.5
$m_H = 2000\ GeV$	31.4±0.3	15.8±0.2	2.07±0.06	49.3±0.3
$m_H = 10000\ GeV$	30.5±0.2	15.2±0.2	2.12±0.06	47.8±0.3

- $m_H = 500$ GeV: $R \simeq (4.0 \pm 0.5)\%$;
- $m_H = 1000$ GeV: $R \simeq (4.0 \pm 0.6)\%$;
- $m_H = 2000$ GeV: $R \simeq (4.1 \pm 0.8)\%$;
- $m_H = 10000$ GeV: $R \simeq (4.1 \pm 0.8)\%$.

4.4.2 Signal Over Background Ratio

High signal over background ratio is extremely important to discriminate the signal from the background and to draw a conclusion on the presence of the signal (see Note 2 of this Chapter).

In Tables 4.16 and 4.17, the number of signal and background events are shown. There are no background events over 2 TeV. For the no-Higgs scenario samples, two events are present over 2 TeV (after 100 fb^{-1}).

In Table 4.18, $S/\sqrt{B}$ ratio for all the signal data samples and for two different intervals of the VV system invariant mass are shown. The intervals taken in account are: 0<M_{inv}^{VV}<1 TeV and M_{inv}^{VV}>1 TeV, because 1 TeV is a convenient limit between Higgs scenario (first interval) and no-Higgs scenario (second interval). The signal over background ratios are high in the regions of interest for all the signals. Since this is a preliminary study, the results are satisfactory.

Table 4.17: *Number of background events after 100 fb^{-1} of integrated luminosity. The statistical uncertainty is given.*

Background				
Samples	**0<M_{inv}^{VV}<1 TeV**	**1<M_{inv}^{VV}<2 TeV**	**M_{inv}^{VV}>2 TeV**	**All**
$qq \to ZZ$	21±2	1.4±0.6	0	23±2
$qq \to ZW$	16±2	1.4±0.6	0	18±2
Z + *jet*	0	0	0	0
$t\bar{t}$	238±137	0	0	238±137
All background	276±137	2.8±0.8	0	279±137

Table 4.18: *Signal over background ratio after 100 fb^{-1} of integrated luminosity.*

Signal over background ratio			
Samples	**0<M_{inv}^{VV}<1 TeV**	**M_{inv}^{VV}>1 TeV**	**All**
$m_H = 500\ GeV$	9±3	1.0±0.6	9±3
$m_H = 1000\ GeV$	3.3±1.2	13±3	5±2
$m_H = 2000\ GeV$	1.9±0.7	11±2	3.0±1.0
$m_H = 10000\ GeV$	1.8±0.6	10±2	2.9±1.0

Summary

Electroweak symmetry breaking can be probed through the fusion of longitudinally polarized vector bosons. Since no real data are yet available, Monte Carlo samples processed through the CMS detector simulation have been used for this study. At this stage the CMSJET fast simulation package was used. Its reliability was confirmed by a comparison with the results obtained with the full simulation.

Good resolution on the signal observables (for both the $V_L V_L \to Z_L Z_L$ and $Z_L W_L \to Z_L W_L$ processes) has been achieved: in particular a resolution of 4% on the invariant mass of the VV-fusion process has been obtained.

No significant experimental difference has been found between the two signal processes studied; therefore the two samples were merged.

It has been shown that most of the background can be rejected, in particular at high values of the VV system mass. The most powerful tool to reject the background is the tagging of the two jets which emit the vector bosons.

Since the background efficiency is lower than one percent and the signal efficiency reaches 30%, a high signal over background ratio ($s/\sqrt{B}$) has been achieved for an integrated luminosity of 100 fb^{-1} (~ 8.5 in the interval $M_{inv}^{VV} \in [0,1]$ TeV for the Higgs mass set to 500 GeV and ~ 10.5 for $M_{inv}^{VV} > 1$ TeV for the no Higgs scenario).

In conclusion the CMS experiment can be used to probe electroweak symmetry breaking through the fusion of longitudinally polarized vector bosons. The signal reconstruction and the background rejection algorithm has been successfully tested on the fast simulation. In the near future the study will be repeated with the full simulation.

Appendix

The Effective Vector Boson Approximation (EVBA)

If no light Higgs boson exists, a perturbative calculation involving VV production will not be useful, whereas the effective vector boson approximation (EVBA) can still be used. The EVBA [58, 59] is equivalent to the Effective Photon Approximation (EPA, or Weizsäcker-Williams approximation) used in QED for the study of photon-photon processes. It is a reliable technique which consists of treating the W and Z bosons as on-shell partons in the quarks: the fermion-fermion cross section is written as a product of the distribution functions of the vector boson inside the quark and the cross section for on-shell VV scattering. Consider, for example, the scattering process $a + A \to X$ at a centre-of-mass energy s; the cross section is factorized into probability densities $P_{pol}^{V/a}(z)$ for finding a vector boson V with polarization pol in the incoming fermion a, and hard vector boson scattering cross sections at a reduced centre-of-mass energy xs:

$$d\sigma(a + A \to X,\, s) = \int_{x_{min}}^{1} dx \sum_{V} \sum_{pol} P_{pol}^{V/a}(x) d\sigma(V_{pol} + A \to X,\, xs)\,.$$

In the application to VV scattering the probability densities for vector boson pairs are obtained as a convolution of single vector boson probability densities:

$$\mathcal{L}_{pol_1 pol_2}^{V_1 V_2/ab}(x) = \int_{z_{min}}^{1} \frac{dz}{z} P_{pol_1}^{V_1/a}(z) P_{pol_2}^{V_2/b}(x/z)\,.$$

Thus, the cross section for two fermion scattering can be written as:

$$d\sigma(a + b \to X,\, s) = \int_{x_{min}}^{1} dx \sum_{V_1,V_2} \sum_{pol_1,pol_2} \mathcal{L}_{pol_1 pol_2}^{V_1 V_2/ab}(x) d\sigma(V_1^{pol_1} + V_2^{pol_2} \to X,\, xs)$$

The basic assumption is that the cross section for the scattering of an on-shell vector boson is similar to the cross section for on-shell vectors. If there is no Higgs with mass below ~ 0.8 TeV, the EVBA technique is essential to make progress in the study of VV scattering. Otherwise, if a light Higgs boson exists, this approximation can be still considered a useful and simplifying approach to the calculations. In fact the EVBA gives reliable results for heavy Higgs boson production through the VV-fusion process when all the tree-level diagrams are considered.

Bibliography

[1] F. Halzen and A.D. Martin, *Quarks and leptons: an introductory course in modern particle physics*, John Willey; New York, 1984.

[2] T.P. Cheng and L.F. Li, *Gauge theory of the elementary particle physics,* Oxford Univ. Press, 1991 (reprinted).

[3] S.L. Glashow, Nucl.Phys. 22 (1961) 579.

[4] M. Herrero, *The Standard Model*, hep-ph/9812242 (1998)

[5] The LEP Electroweak Working Group and the SLD Heavy Flavour Group, *A Combination of Preliminary Electroweak Measurements and Constraints on the Standard Model*, The LEP collaborations, LEPEWWG/2004 (2004).

[6] Particle Data Group, Review of particle physics (2002), http://pdg.lbl.gov.

[7] P. Higgs, Phys. Lett. 12 (1964) 132.

[8] P. Higgs, Phys. Lett. 145 (1966) 1156.

[9] T. van Ritbergen and R.G. Stuart, Phys. Rev. Lett. 82 (1999).

[10] W.J. Marciano and A. Sirlin, Phys. Rev. Lett. 61 (1988) 1815.

[11] Murray Gell-Mann, Phys. Rev. 125 (1962) 1067.

[12] The LEP Higgs Working Group, Phys. Lett. B 565 (2003) 61.

[13] S.L.Glashow et al., Phys. Rev. Lett. 40 (1978) 692.

[14] M. Spira and P.M. Zerwas, CERN-TH/97-379 (1997).

[15] J. F. Gunion et al., The Higgs Hunter's Guide, Addison-Wesley Publishing Company, 1990.

[16] M. Golden, T. Han and G. Valencia, hep-hp/9511206 (1995).

[17] G.J. Gounaris, J. Layssac and F.M. Renard, hep-ph/9309324 (1993).

[18] C. Quigg, B.W. Lee and H.B. Thacker, Phys. Rev. Lett. 38 (1977) 883.

[19] C. Quigg, B.W. Lee and H.B. Thacker, Phys. Rev. D 16 (1977) 1519.

[20] A. Dobado and J.R. Pelaez, Phys. Rev. D 56 (1997) 3057.

[21] S.N. Gupta. Quantum Electrodynamics. Gordon and Breach, 1981.

[22] G. Altarelli and G. Isidori, Phys. Lett. B 337 (1994) 141.

[23] R.S. Willey, Phys. Lett. B 377 (1996) 255.

[24] N. Cabibbo et al., Nucl. Phys. B 158 (1979) 295.

[25] C. Ford, D.R.T. Jones and P.W. Stephenson, Nucl. Phys. B395 17 (1978).

[26] M. Golden et al., hep-ph/9503230 (1995).

[27] G.J. Gounaris et al., hep-ph/9311370 (1993).

[28] T.L. Barklow et al., hep-ph/9704217 (1997).

[29] A. Dobado and M.J. Herrero hep-ph/9912224 (2000).

[30] M.S. Chanowitz, Ann. Rev. Nucl. Part. Sci. 38 (1988) 323.

[31] G. Ridolfi, hep-ph/0106300 (2001).

[32] The LHC Study Group, The Large Hadron Collider Conceptual Design, CERN/AC 95-05 (1995).

[33] G. Altarelli and M.L. Mangano (editors), Proceedings of the Workshop on Standard Model Physics (and more) at the LHC (2000), CERN 2000-004.

[34] The ALICE Collaboration, Technical Proposal for A Large Ion Collider Experiment at the CERN LHC, CERN/LHCC 95-71 (1995).

[35] The LHCb Collaboration, Technical Proposal, CERN/LHCC 98-4 (1998).

[36] The ATLAS Collaboration, Technical Proposal, CERN/LHCC 94-43, LHCC/P2 (1994).

[37] The CMS Collaboration, Technical Proposal, CERN/LHCC 94-38, LHCC/P1 (1994).

[38] The CMS Collaboration, The Magnet Project: Technical Design Report, CERN/LHCC 97-10, CMS TDR 1 (1997).

[39] The CMS Collaboration, The Tracker Project: Technical Design Report, CERN/LHCC 98-6, CMS TDR 5 (1998).

[40] The CMS Collaboration, Addendum to the CMS Tracker Technical Design Report, CERN/LHCC 2000-016, CMS TDR 5 Addendum 1 (2000).

[41] The CMS Collaboration, The TriDAS Project, Technical Design Report: Data Acquisition and High-Level Trigger, CERN/LHCC 02-26, CMS TDR 6.1 (2002).

[42] The CMS Collaboration, The Electromagnetic Calorimeter Project: Technical Design Report, CERN/LHCC 97-33, CMS TDR 4 (1997).

[43] The CMS Collaboration, The Hadronic Calorimeter: Technical Design Report, CERN/LHCC 97-31, CMS TDR 2 (1997).

[44] The CMS Collaboration, The Muon Project, Technical Design Report, CERN/LHCC 97-32, CMS TDR 3 (1997).

[45] The CMS Collaboration, The Trigger Project, Technical Design Report: The Level-1 Trigger, CERN/LHCC 2000-038, CMS TDR 6.1 (2000).

[46] Hans Wenzel, AIP Conf. Proc. 583(1) 319 (Aug 2001).

[47] T. Sjoŏstrand et al., High-energy-physics event generation with PYTHIA 6.1, Comp. Phys. Comm. 135 (2001) 238.

[48] S. Abdullin, A. Khanov and N. Stepanov, CMSJET, CMS TN/94-180 (Aug 2002).

[49] M. Seymour et al., HERWIG, http://hepwww.rl.ac.uk/theory/seymour/herwig/.

[50] H. Baer et al., ISAJET/ISASUSY, http://www.phy.bnl.gov/~isajet/.

[51] Z. Was, TAUOLA the library for tau lepton decay, hep-ph/0011305 (Nov 2000).

[52] S. Slabospitsky et al., TopRex, http://cmsdoc.cern.ch/~spitskyc/toprex/toprex.html.

[53] E. Boos et al., CompHEP, http://www.ifh.de/~pukhov/comphep.html.

[54] M.L. Mangano et al., AlpGEN, http://mlm.home.cern.ch/mlm/alpgen/.

[55] F. Maltoni and T. Stelzer, MadGraph, http://madgraph.hep.uiuc.edu/.

[56] L. Taylor et al., CMKIN - The CMS Kinematics interface package, CMS TN/96-099 (July 1996).

[57] M. Glück, E. Reya and A. Vogt, Z. Phys. C67 (1995) 433.

[58] I. Kuss, Phys. Rev. D 55(11) (1997) 7165.

[59] I. Kuss and H. Spierberger, BI-TP 95/25 (1995).

[60] CMS Software and Computing Group, Object oriented Simulation for CMS Analysis and Reconstruction, http://cmsdoc.cern.ch/OSCAR/.

[61] The Geant4 Collaboration, GEANT – Detector Description and Simulation Tool, geant4.web.cern.ch/geant4/.

[62] CMS Software and Computing Group, Object Oriented Reconstruction for CMS Analysis, http://cmsdoc.cern.ch/orca/.

[63] CMS Software and Computing Group, CMS Geometry Project, http://cmsdoc.cern.ch/cms/software/geometry/index.html.

[64] CMS Software and Computing Group, Detector Description Database, http://cmsdoc.cern.ch/cms/software/ddd/www/index.html.

[65] V. Innocente et al., Coherent Object-oriented Base for Reconstruction, Analysis and simulation, http://cobra.web.cern.ch/cobra/.

[66] G.Alverson et al., Interactive Graphics for User ANAlysis, http://iguana.cern.ch.

[67] CMS Software and Computing Group, Software Configuration, Release And Management, http://cmsdoc.cern.ch/Releases/SCRAM/current/cgi/scrampage.cgi.

[68] CVS, Concurrent Version System, https://www.cvshome.org/.

[69] M. Shaw, Some Patterns for Software Architecture, Proceedings of the Second Workshop on Pattern languages For Programming, Addison Wesley, Reading Masachusetts, 1994.

[70] Dirk Duellmann et al., POOL, Pool Of persistent Objects for LHC, http://lcgapp.cern.ch/project/persist/.

[71] CMS Software and Computing Group, CMS FAst MOnte Carlo Simulation, http://cmsdoc.cern.ch/famos/.

[72] ROOT user guide, http://root.cern.ch.

Ringraziamenti

Non è facile ringraziare in modo adeguato le persone che mi hanno aiutato a portare a termine questo lavoro e il mio percorso di studi. Cercherò di farlo, confidando che ognuno di loro abbia benevolenza nei miei confronti, per la semplicità dei miei ringraziamenti.

Lavorare insieme alle persone del gruppo di CMS Torino è stata un'esperienza molto importante. Ringrazio tutte le persone con cui ho potuto collaborare e anche quelle con cui non ho potuto, perché è cruciale avere alle spalle un gruppo compatto.

Vorrei ringraziare particolarmente (e non finirò mai di farlo) la Dott.sa Chiara Mariotti che, nonostante i suoi impegni veramente importanti, non mi ha mai fatto mancare il suo supporto, sia professionale che umano. In questi mesi di lavoro, grazie a lei e ai suoi continui stimoli, ho potuto imparare molto e crescere, lavorando in un ambiente entusiasmante. Un sentito ringraziamento alla Prof.sa Alessandra Romero per avermi seguito dall'alto, provvedendo all'organizzazione del lavoro nella sua interezza e organicità. Ringrazio in modo speciale il Prof. Michele Arneodo che è stato veramente prezioso per gli innumerevoli consigli e miglioramenti alla tesi. Ringrazio molto anche Elena Accomando per le correzioni al capitolo primo. Tutto è stato molto più facile avendo come punti di riferimento Nicola Amapane e Gianluca Cerminara, i quali ringrazio per il tanto tempo dedicatomi e i continui aiuti prestatimi in questi mesi.

In questi anni vissuti a Torino ho avuto la fortuna di conoscere persone veramente eccezionali, senza le quali una parte di me, ora, sarebbe indubbiamente diversa. Diego e Betta, che tra un piatto di pasta, una nuotata e centinaia di ore a parlare di fisica hanno saputo rendere meno dura la vita in università e divertente quella al di fuori. Davide, Christian e Alessio, insostituibili compagni

di viaggio... è stato bello studiare e condividere le giornate con voi! Ma anche Angela, Manuela, i due Dario, Enzo e Marco, con i quali si son trascorse sempre ore piacevoli assieme.

Un ringraziamento speciale va ai miei due amici e compagni d'appartamento Fabry e Simone che hanno sopportato tutte le mie pazzie. In particolare Simone, per il quale nutro il più profondo sentimento di amicizia. Sono stati anni bellissimi questi passati assieme, sarà dura un giorno non vivere più assieme. Un abbraccio e un grazie va anche a tutti i miei amici nel "lontano" biellese, che non mi hanno mai abbandonato e mi hanno sempre trasmesso la voglia di stare assieme. Mi hanno aiutato innumerevoli volte a "staccare la spina"; grazie Paolo, Ale, Davide, Max, Raffaella, Nadia, Danielone, Monica e Flavia. Ringrazio anche Piera S., Adriana C. e Riccardo F., miei ex professori, che hanno sempre creduto in me.

E come non ringraziare mio fratello, il miglior fratello e amico che si possa avere, per i continui incoraggiamenti e il grande supporto morale (e tecnico) datomi. Sono stati il mio carburante in questi anni. Mio nonno Mario che mi ha insegnato che tutto si può aggiustare, anche utilizzando solo un fil di ferro. Mia nonna Ada, che mi ha insegnato che ogni tanto bisogna sapersi fermare, e mangiare! Mia nonna Tina, che è una seconda mamma per me, e mi ha insegnato a non avere paura di fronte a nulla. Mio nonno Osvaldo, perché mi ha insegnato ad essere curioso e nella fisica, e nella vita, è un fattore molto importante. Decisivo. La mia Sara, senza la quale semplicemente questo lavoro non sarebbe potuto esistere. Perché senza di lei non avrei fatto il fisico e perché insieme a lei nessun ostacolo che mi si è parato di fronte mi ha mai impensierito. Mia Mamma e mio Papà, per i quali io esisto. Non sarebbe possibile elencare quanto mi hanno insegnato, e quanto ancora voglio imparare. Mi hanno reso un uomo. A loro dedico questo lavoro, sintesi dei miei frutti. Sintesi dei loro sacrifici per me.